OPTIMIZATION OF A MULTILAYER ALUMINA TEMPLATE FOR ELECTROCHEMICAL DEPOSITION OF QUANTUM WIRES AND QUANTUM DOTS

By

ATAUL AZIZ IKRAM

A dissertation submitted to the Graduate Faculty in Engineering in partial fulfillment of the requirements for the degree of Doctor of Philosophy,
The City University of New York

2007

This manuscript has been read and accepted for the Graduate Faculty in Engineering in satisfaction of the dissertation requirement for the degree of Doctor of Philosophy.

Professor David Crouse

Date

Chair of Examining Committee

Professor Mumtaz Kassir

Date

Executive Officer

Professor Roger Dorsinville

Professor Fred Moshary

Professor Aidong Shen

Dr. Thomas James

Supervision Committee

THE CITY UNIVERSITY OF NEWYORK

Abstract

OPTIMIZATION OF A MULTILAYER ALUMINA TEMPLATE FOR ELECTROCHEMICAL DEPOSITION OF QUANTUM WIRES AND QUANTUM DOTS

By

Ataul Aziz Ikram

Advisor: Professor David Crouse

With advances in fabrication techniques, it is becoming possible to tap into low dimensional physics of materials, and the favorable characteristics exhibited by these at quantum scales, for applications in devices in general. Device applications range from electrical, optical, mechanical, to chemical and biological. Confinement in one, two or three dimensions, are achieved in quantum wells, wires and dots, respectively. These structures each have their own advantages in fabrication and trade offs with respect to the cost in fabrication convenience, and relevant applications. This thesis presents a previously developed multilayer alumina template, and optimizes the template for quantum wire and dot fabrication. Issues such as structural integrity, material quality, and reproducibility of fabrication results are improved upon for tech transfer purposes, and for scaling up to industrial size wafers. The resultant template is shown to be an excellent host for electrodeposition for semiconductors and metals. An overview of nanowire device applications is presented, with some background of the physics involved, and simulation results describing quantum wire infrared photodetectors, based on the same.

This is followed by a general description of aluminum anodization and the newly developed multilayer template that has desirable characteristics as a host for quantum wire fabrication. Lastly, quantum wire and quantum dot fabrication results are outlined. Characterization of the electrodeposited material is described, with favorable results depicting quantum confinement effects in the structures grown.

Acknowledgements

In search of knowledge, this happens to be a milestone, in my career. During this journey of learning, there have been a number of people that have come, some have stayed, and traveled with me, others, have left and gone on their ways. It is important, for me to mention some names that have been the foundation for this achievement. Before, I mention names of people, I would like to thank Allah, for providing me with this opportunity, to learn from it, and to become a better person, human, and professional in my field. This span of my life, where I have met different people related to my work, and otherwise, has been a complete learning experience, in terms of events, challenges, and realizations. I would like to thank my parents whose prayers, support, and love, has been a source of inspiration, and a driving force for me throughout this period of highs and lows.

My mentor Prof. Crouse, has been a source of guidance, and I admire his ability to tackle the most challenging problems with great confidence and conviction. I have learned from him that nothing is impossible if you approach it with the right attitude.

During my stay at New York, my friend Rommana, who has been a sister to me really, with her love, generosity and care, and has not let me feel the absence of my family. I would like to thank my dear friend Omer, for his moral support and for picking up my confidence, at many occasions, and being a true brother to me. I would also like to thank my colleague Tom, for his sincere advice related to work in general, and also for his valuable comments while I was preparing my thesis, and the final presentation.

Table of Contents

List of Figures

List of Tables

Chapter 1 Introduction

As advances in technology begin to allow fabrication and characterization in the nanoscale regime, more and more research is being conducted in this area. Quantum confinement effects modify the physics of materials, and properties can be tailored for device applications. Device applications range from electrical, optical, mechanical, to chemical and biological. Confinement in one two or three dimensions, are achieved in quantum wells, wires and dots, respectively. These structures each have their own advantages in fabrication and trade offs with respect to fabrication cost, convenience, and applications. This thesis proposes a device structure based on quantum wires within a newly optimized alumina template that uses intersubband absorption mechanism for infrared photodetection and optimizes the multilayer template that is the starting material for such a device structure. The simulation results for materials absorbing in the IR regime show that such a device can be fabricated. We present a study of the anodization of aluminum from a more practical perspective for electrodeposition of II-VI semiconductor nanowires, so that the technique can be scaled for mass production or

tech-transfer to the industry. The thesis starts with an overview of nanowire device applications, with some background of the physics involved, and simulation results describing quantum wire infrared photodetector device structure. An overview of the anodic alumina is presented with an introduction to a newly developed multilayer template that has desirable characteristics as a host for quantum wire fabrication. The challenges to improve the process for better and reproducible results of fabrication are then addressed. Following this, fabrication techniques of quantum wires is presented, with recent results of porous templates as hosts for growth. This is followed by structural and optical characterization of the quantum structures.

1.1 Background

II-VI semiconductors have a fundamental bandgap that falls in the visible spectrum to the near infrared from 1.43eV to 2.713eV (457nm-867nm). With quantum confinement effects the fundamental bandgap sees an increase [1] as well as a shift in the lowest energy level in the conduction band and the highest level in the valence band. In addition there is a significant change in density of states at low dimensions. The energy states are discretized and spread apart as dimensions of structures are decreased in all directions. These two very important phenomena are the founding properties for photodetecting applications utilizing semiconductor nanostructures. We are interested in LWIR and MWIR photodetection. A sample wavelength of 5μm corresponds to a fundamental bandgap of 0.25eV.

There are two windows that are used in the infrared spectrum. Radiant emission from objects at ambient temperature (300K) will pass through atmosphere unaffected if it is in one of these windows or bands, i.e. the 3-5μm band and in the 8-14μm band. Other

emissions in the spectrum are absorbed by carbon dioxide and water vapors. The windows are shown in Fig. 1 [2].

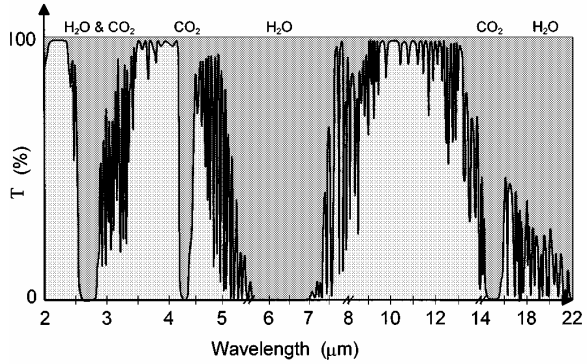

Figure 1: Atmospheric transmission windows in the infrared range of the optical spectrum, taken for transmission through 300m of humid air at sea level [2]

1.1.1 Types of Photodetectors

Three types of infrared photodetectors exist, intrinsic, extrinsic and quantum structure (well/wire/dot) photodetectors [2]. The basic principle of operation of intrinsic and extrinsic photodetectors is that, photons are excited from the valence band to the conduction band if an incident photon of energy larger than the bandgap is absorbed by an electron in the valence band, and on applying a bias, may be recorded as current. The wavelength of absorption is thus controlled by the fundamental bandgap E_g. Tuning the wavelength of absorption therefore translates to engineering of the bandgap, which may be achieved by altering the composition of the materials being used for device operation, in case of alloys. In case of direct bandgap intrinsic infrared photodetectors based on II-VI alloys of (Hg,Cd)Te, or (Pb,Sn)Te, varying the composition of Hg/Cd, and Pb/Sn may allow absorption from 3μm to 15μm by tuning the bandgap from 413.3 to 82.7meV [2].

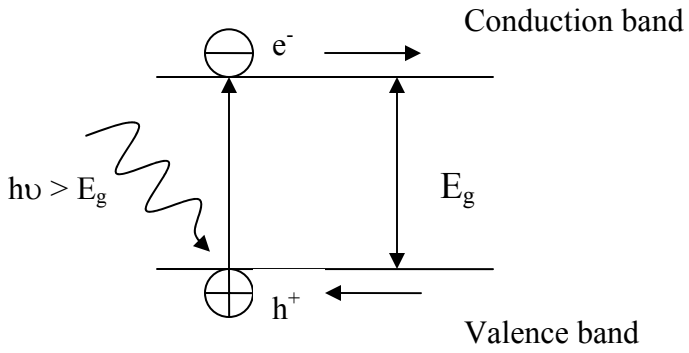

Figure 2: Schematic of Band to Band Absorption by a photon

However, one of the main disadvantages of these photodetectors is the fabrication cost. This is due to the fact that materials with such small bandgaps are soft, and it is difficult to grow and process large area wafers [2].

The second type of photodetectors is called extrinsic photodetectors where an impurity band is introduced in the bandgap due to doping. Absorption, hence takes place from the impurity band to the conduction band, wherein it can be recorded as current at application of a bias. These types of detectors are limited by the materials available for doping and hence the absorption wavelengths are also limited [2].

This brings us to the photodetectors based on quantum structures, i.e. wells, wires, and dots. Quantum well devices are well researched and may employ intersubband absorption as the mechanism of operation. These structures are very promising, as the wavelength can be tailored effectively, and being based on semiconductors such as GaAs, the growth and processing technologies are mature [2]. This provides the possibility of manufacturing high uniformity, reproducibility, and large area low cost arrays. As it is possible to accurately control band structure, the spectral response can be effectively

controlled, as well as integration with GaAs multiplexers and other electronics [2]. The drawback however, is the inability to detect normal incident radiation for n-type quantum wells. Recently however there has been some promise of possible absorption utilizing p-type material based QWIPS [3]. Compared to bulk direct bandgap semiconductors such as (Hg, Cd)Te, photodetectors based on this structure also depict lower quantum efficiency, and lower responsivity. The inability to detect normal incident light can be rectified by using a grating or corrugated surface. This allows for the electric field vector to be aligned parallel to the current dipole of the confined charge, so that it can be absorbed [2].

1.2 Dissertation Objective

This dissertation describes the optimization of a multilayer template that can be used as a host for electrochemical deposition of II VI semiconductor quantum wires, and quantum dots. Based on this material system, we propose a novel device structure. The proposed device structure that this research work is aimed at fabricating eventually is a photodetector in the infrared region based on quantum wires heterostructures. This may be achieved by using semiconductor materials, employing nanowires, or nanodots, or combinations thereof. Utilizing quantum dots exclusively has the disadvantage that it is difficult to provide connections to the ends of the structures [4].

Quantum wires on the other hand are easier to connect, and also have the advantage of absorbing normal incident light, as opposed to quantum well structures wherein intersubband absorption between a pair of bands can occur either in the normal to plane polarized light or in plane polarized light [5]. Quantum dot intersubband absorption promises to be higher compared to QWIPS and HgCdTe band to band detectors, by

several orders of magnitude [6], and also depends on polarization of the incoming light [7].

We want to utilize quantum wires for intersubband absorption in devices based on quantum wires, for infrared detection. In addition to the main advantage, i.e. normal absorption, over bulk HgCdTe and QWIP detectors, it is easier to tailor the absorption wavelengths by modifying the radii and materials involved in the device with these structures. The immediate application would be the ability to grow the material on a substrate of choice, such as silicon, that allows for readout circuitry to be fabricated with great ease.

Quantum wire fabrication has been studied in great detail in the past decade, and a myriad of fabrication procedures are being explored in general, and fabrication involving porous membranes such as alumina, are also available in literature. The technique utilized in this work is electrochemical deposition within an alumina template. The motivation is the development of a multilayer template that allows for fabrication of nanowires within by the possibility of having a platinum metal at the pore base. The novel aspect in this type of fabrication is the fact that the anodization template is fabricated using a one step anodization and barrier layer removal in situ, and the nanowire growth can then be done using DC (direct current) electrochemical deposition, instead of AC (that is needed if a barrier layer is present). This procedure is known to yield nanowires of very good quality [8], and the technique can be easily extended to a variety of II-VI semiconductors and other materials, with well researched thin film deposition literature available. Recently, there is work in the area of III-V semiconductor nanowire fabrication by electrodeposition in anodic alumina templates [9]. The development and characterization

of the alumina template will be described later in this thesis.

1.2.1 Quantum Wire Heterostructures

The device structure that will be using the nanowires mentioned above is briefly described next. The material consists of an array of nanowires shown in Figure 3. The nanowires consist of two different materials with some constraint on the range of effective masses, and band offsets of the heterostructures, that will allow for absorption in the IR regime. The calculation is provided in a later chapter. A simple explanation of the device operation based on such a combination of materials is given as follows:

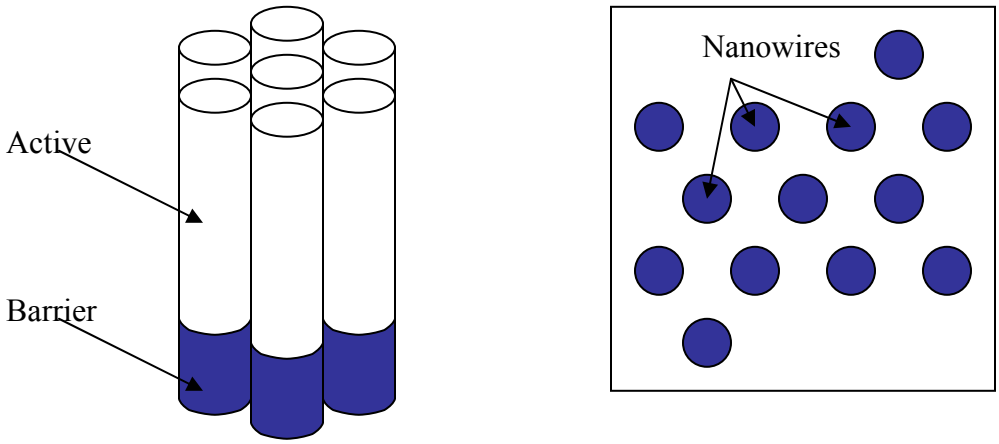

(a) Cross Section: Free standing Wires

(b) Top View: Wires in Alumina Template

Figure 3: (a) Schematic of Nanowire Heterostructures (b) Nanowires within Alumina Template

The energy bands are discretized as is expected at the nanoscale (wires may vary between 10 nm to 100 nm in diameter). The choice of materials is such that the lowest energy

band on the barrier side of the nanowire aligns with the second energy band of the active barrier. Both of the materials are nonintentionally doped. In this case the lowest energy level on the active side of the wire, is populated with electrons, that may be excited by incident of photons with energy hν such that E_2-E_1> hν.At the application of a bias, these electrons can tunnel across the interface between the different materials, and thus can be recorded as a photocurrent. The energy difference can be tailored such that the absorption energy corresponds to a wavelength in the spectrum of choice, and can easily be modified to absorb in the infrared regime. An example of infrared absorption of radiation at 5μm corresponds to an energy difference of 0.125eV.

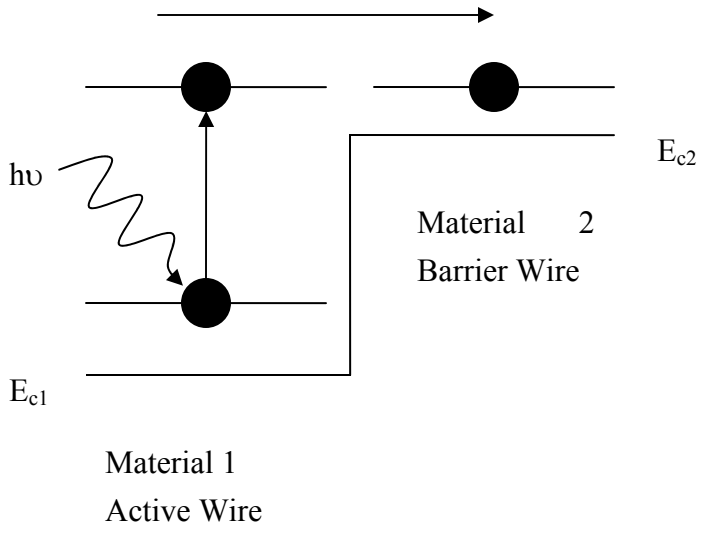

Figure 4: Intersubband Absorption within Conduction Band and Photodetection in a Nanowire Heterostructure

The calculation of the energy levels for a given material nanostructure, will determine what material will be suitable for operation of device based on this concept, which will be determined by the effective masses and band offsets. For example, the difference between

energy levels on one side of the wire will correspond to absorption wavelength, and applying a bias the electrons will tunnel through the barrier and be recorded as photocurrent. If normal incident light falls on the detectors only the QRIP will produce an appreciable current because of photon absorption selection rules. The concept of intersubband transitions is also shown along with the transition of the excited electron from the active wire to the barrier wire in figure 4. The fabrication of this kind of semiconductor heterostructures has been successfully achieved in porous anodic alumina templates. A combination of different types of materials have been done, such as metal metal, metal semiconductor, bimetallic, metal oxide metal, and semiconductor semiconductor [10-21].

1.2.2 Device Structure

Our idea is to fabricate an intersubband photodetector, and the device structure for such a detector is given in Fig. 5 [22]. This detector is based on an anodized alumina nanoporous array. The alumina is fabricated from a multilayer template and fabrication is explained in earlier works of Crouse et al. [23], and given in the present paper in the section describing the anodic alumina.

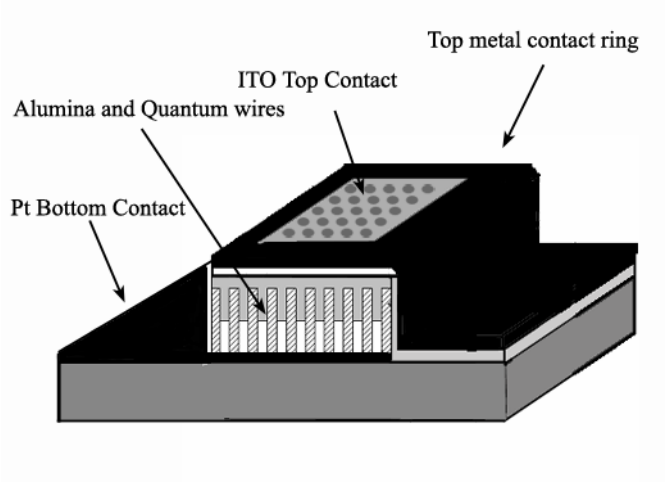

Figure 5: One design of a QRIP that uses the multilayer nanotemplate. This one pixel detector has a Si substrate with a Pt bottom electrode, an ITO Top contact and metal contact ring. The active wire (white) is next to the substrate and the barrier wire (gray) is above it and makes an electrical contact with the ITO.

The top electrical contacts may be a transparent conductive oxide, e.g. indium tin oxide (ITO), as it has been extensively used for electrical contacts for CdS/CdTe solar cells and thus can also be used for the CdSe/CdTe QRIPs [24-25].

This device structure provides the following advantages with respect to the prevalent technologies within this area :

- Possibility to incorporate onto a substrate of choice, namely Silicon.
- Possibility to modify the absorption wavelengths by modifying simple growth parameters in a wide range.
- Easy and cost effective fabrication technique

1.3 Organization

This thesis is arranged as follows. The first two chapters go over theoretical concepts of photon, phonons and electron-photon, electron-phonon interactions. These will also provide basis for the fabrication parameters to achieve the absorption wavelength and requirements of the experimental setup. The following chapter describes anodization in detail, and how optimization of the multilayer template has been achieved for good device fabrication, and how issues with material quality, such as adhesion, intermetallic formation etc have been resolved, and an excellent starting template for electrodeposition has been progressively achieved. The following chapter will describe electrodeposition of CdTe quantum dots and quantum wires, and provide characterization results for the same. The last chapter will conclude the results and provide some information on how these results can be enhanced into a bigger project that may have broader applications by involving other materials and more complex structures within the optimized alumina template.

Chapter 2 Electron Photon Interaction

2.1 Background

In order to understand the operation of device based on quantum structures it is of empirical importance to cover the general theory of electrons in semiconductor, including a simple treatment of time independent Schrodinger's equation, the dispersion curves based on the parabolic approximation, and absorption in single quantum wires.

Generally, the energy eigenvalues and eigenfunctions have strong dependence on symmetry. Due to periodicity of the lattice, the Hamiltonian is invariant under lattice translations, the spectrum has the form of energy bands separated by forbidden gaps, and eigenfunctions are Bloch waves. Electron transport in a structure depends on the crystal structure of the material and is strongly dependent on the orientation of the crystal lattice (an example being electron mobility) [26].

In case of quantum structures, where quantum confinement stems from shape, and size, it makes sense to carry out theoretical simulations to predict material properties, and

eventually device properties in detail.

The most important effect is the increase of the LUMO (lowest unoccupied molecular orbital), and the HOMO (highest occupied molecular orbital) commonly referred to as the bandgap. The values of the bandgap vary with temperature and pressure. The values of the most common semiconductors and semiconductor compounds are given in Table 1 [27].

Table 1: Bandgap values of some common elemental semiconductors and their compounds with dependence on temperature and pressure [27].

Semiconductor	$E_g(300K)$	$dE_g = dT$ (meV/$_o$K)	$dE_g = dP$ (meV/kbar)
Si	1.110	-0.28	-1.41
Ge	0.664	-0.37	5.1
GaP	2.272	-0.37	10.5
GaAs	1.411	-0.39	11.3
GaSb	0.70	-0.37	14.5
InP	1.34	-0.29	9.1
InAs	0.356	-0.34	10.0
InSb	0.180	-0.28	15.7
ZnSe	2.713	-0.45	0.7
ZnTe	2.26	-0.52	8.3
CdS	2.485	-0.41	4.5
CdSe	1.751	0.36	5.
CdTe	1.43	-0.54	8

2.2 Energy levels in single Quantum Wires:

In the introductory chapter, we had devised a device based on quantum wire heterostructures of semiconductor. Both of these materials are II-VI semiconductors. The choice of the semiconductor is done after initial simulation results as described next. The starting point is to solve the time independent Schrodinger's equation, and obtain the energy levels on each side of the nanowire. Once these are calculated we can apply finite element techniques to calculate the expected absorption in a nanowire heterostructure.

As a starting point, it is assumed that the energy at the band edges (conduction and valence band) is parabolic in nature, i.e. energy is proportional to the square of the wavevector k. In the bands the effects on the electron motion are accounted for by taking its mass as a constant, i.e. effective mass m_e. Solving the Schrodinger's equation under the effective mass approximation, we will get the energy eigenvalues to the equation.

In general the Schrodinger's equation that is the principal equation of quantum mechanics is given by [26]

$$i\hbar\frac{\partial\Psi}{\partial t} - \mathrm{H}\Psi = 0 \qquad (1)$$

In the above equation H is the Hamiltonian operator of the system and is given by

$$\mathrm{H} = -\frac{\hbar^2\nabla^2}{2m} + V(\vec{r}) \qquad (2)$$

$V(\vec{r})$ is the potential energy term , and the first term is the operator of the kinetic energy, in cylindrical coordinates, it is given by

$$\nabla^2 = \frac{1}{\rho}\frac{\partial}{\partial\rho}\left(\rho\frac{\partial}{\partial\rho}\right) + \frac{1}{\rho}\frac{\partial^2}{\partial^2\phi} + \frac{\partial^2}{\partial^2 z} \qquad (3)$$

The time independent Schrodinger equation can be rewritten as

$$\left[-\frac{\hbar^2\nabla^2}{2m}+V(\vec{r})\right]\psi(\vec{r})=E\psi(\vec{r}) \tag{4}$$

In the above equation E is the energy of a particle.

For a quantum wire structure, this calculation can be very easily done by using the Schrodinger's equation under a finite cylindrical potential well profile. For a uniform quantum wire oriented with its axis parallel to the *z*-axis, with a radius *R* and electron affinity of the semiconductor as χ, the electron potential energy profile is assumed to be:

$$V(r)=\begin{cases}-\chi & \text{for } r <= R\\ 0 & \text{for } r > R\end{cases} \tag{5}$$

Then solution of the Schrodinger's equation gives electron wave functions, expressed in terms of Bessel functions and modified Bessel functions:

$$\varphi_m(r,z,\theta)=\begin{cases}a_m J_m(k_{r1}r)\exp(i(k_z z+m\theta)) & \text{for } r <= R\\ b_m K_m(k_{r2}r)\exp(i(k_z z+m\theta)) & \text{for } r > R\end{cases} \tag{6}$$

where *m* is an integer (only *m=0* is considered in this calculation), a_m and b_m are coefficients that are determined by the boundary conditions at *r=R* and normalizing the wavefunction. The terms k_{r1} and k_{r2} are given by:

$$k_{r1}^{\ 2}=\frac{2mE}{\hbar^2}+\frac{2m\chi}{\hbar^2}-k_z^2 \tag{7}$$

$$k_{r2}^{\ 2}=-\frac{2mE}{\hbar^2}+k_z^2 \tag{8}$$

where for confined states in the potential well, the energies of the states *E* must be in the range of $-\chi+\hbar^2k_z^2/2m<E<\hbar^2k_z^2/2m$ where k_z can be any real value in an infinitely long quantum wire. The values of the energies of the quantum states can be obtained from the solving the following equation obtained by invoking the boundary conditions at *r=R*:

$$k_{r1}\frac{J_1(k_{r1}R)}{J_0(k_{r1}R)}=k_{r2}\frac{K_1(k_{r2}R)}{K_0(k_{r2}R)} \tag{9}$$

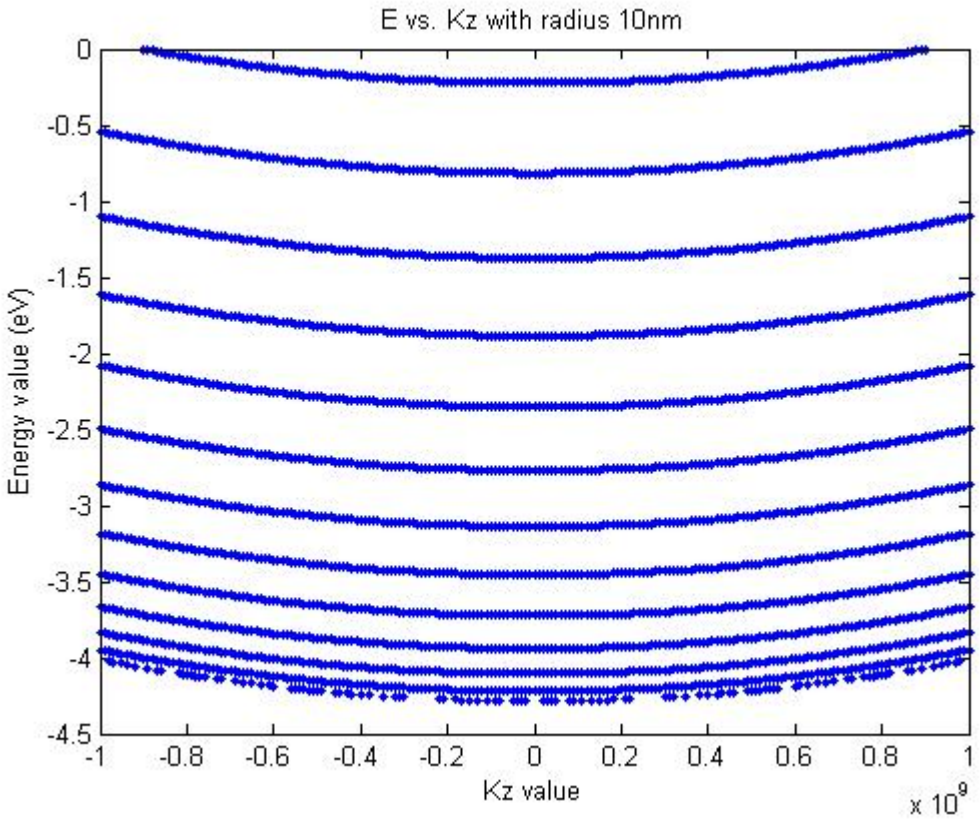

Figure 6: Energy Levels vs. Wavevector kz in CdTe nanowire with a diameter of 20 nm

As can be seen the solution to the above equation depends on three parameters, the wire radius, the effective mass of the electron, and the electron affinity of the material. A plot of energy vs wavevector kz is given in Figure 6 for CdTe for a wire radius of 5nm, and in Figure 7 for a wire radius of 8 nm. We can see that energy discretization is more prominent for a wire radius of 5 nm.

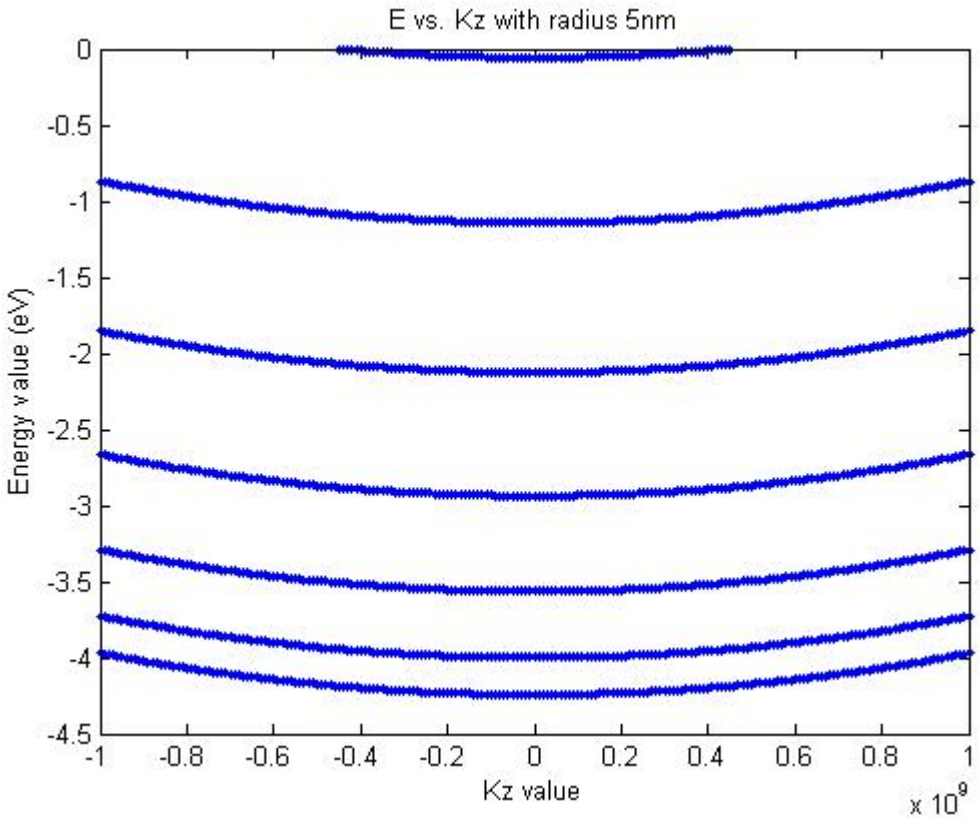

Figure 7: Energy levels vs. wavevector kz in CdTe nanowire with a diameter of 10 nm

2.3 Energy levels and Band Alignment in Quantum Wire Heterostructures:

In context of the calculation for a heterostructures consisting of wires of two different materials, these energy levels on one side, need to align to the energy levels on the other side, such that, the difference in energy would correspond to the absorption wavelength, and applying a bias will allow for photocurrent to be detected, as described earlier. This condition puts a restriction on the types of material that can be used for device operation in the spectrum of choice.

Therefore, there is a limited choice of II VI semiconductors that will allow for this condition to be fulfilled. Figure shows band offsets for three materials, so there is a possibility of CdSe/ZnTe, CdSe/ZnS, or ZnS/ZnTe.

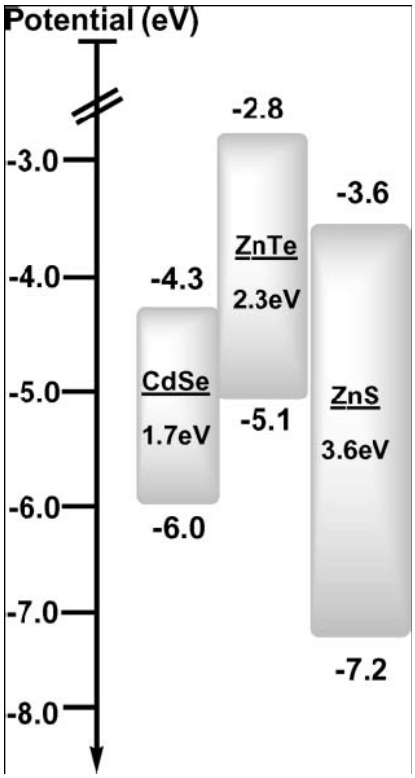

Figure 8: Plot depicting band offsets of CdSe, ZnTe and ZnS [28]

If we carry out the calculation for different materials (hence different effective mass and electron affinity) we can plot the dependence of the energy levels with respect to radius. This exercise will help us determine how the bands of different materials will align, and we can decide what combination of materials will be able to absorb at a particular spectrum of wavelengths, for example in the infrared. With the present template, it is possible to achieve pore sizes with high regularity down to a scale of around 10nm. Therefore the materials that will be electrodeposited should have small effective masses for electrons or holes, in order to get good quantization effect. Because

electrons in II-VI semiconductors have lower effective masses than the holes, the II-VI semiconductors should be n-type dopable. Table 2 gives some important parameters for solvent-based electrodeposited CdTe, CdS, CdSe and ZnSe [29-32]. These parameters suggest that several different types of QRIP designs are possible.

Table 2. II-VI Semiconductor Electronic and Growth Parameters [8]

Semiconductor (at *T=300K*)	m_e^* / m_e	m_h^* / m_e	χ (eV)	E_G (eV)	n-type dopable?
CdTe	0.14	0.35	4.3	1.45	Yes
CdS	0.23	0.7	4.6	2.42	Yes
CdSe	0.13	0.4	4.56	1.73	Yes
ZnSe	0.21	0.6	3.67	2.67	Yes

One design for a shorter wavelength QRIP could use ZnSe as the barrier wire because of its small value for the electron affinity (χ). Reducing χ can be achieved by replacing some of the Zn with Cd to produce $Zn_{1-x}Cd_xSe$. In this device, either CdTe or CdSe may be desirable for the active wire because of their small electron effective masses. For longer wavelength IR, CdSe/ $Zn_{1-x}Cd_xSe$ or CdSe/CdTe quantum wires can be used with the first semiconductor as the active part of the wire and the second semiconductor as the barrier part of the wire.

After having explored different combinations of II-VI semiconductors, we have found that the combination of CdSe, as the active material, CdTe, as the barrier material, will be suitable for the absorption in the IR regime. A plot of the first three energy levels, with respect to diameter within a potential well is given in Figure 9 for CdTe and CdSe and

are plotted on the same graph, to see at what diameters the smallest energy levels align, and hence can be used for photodetection based on the proposed device structure.

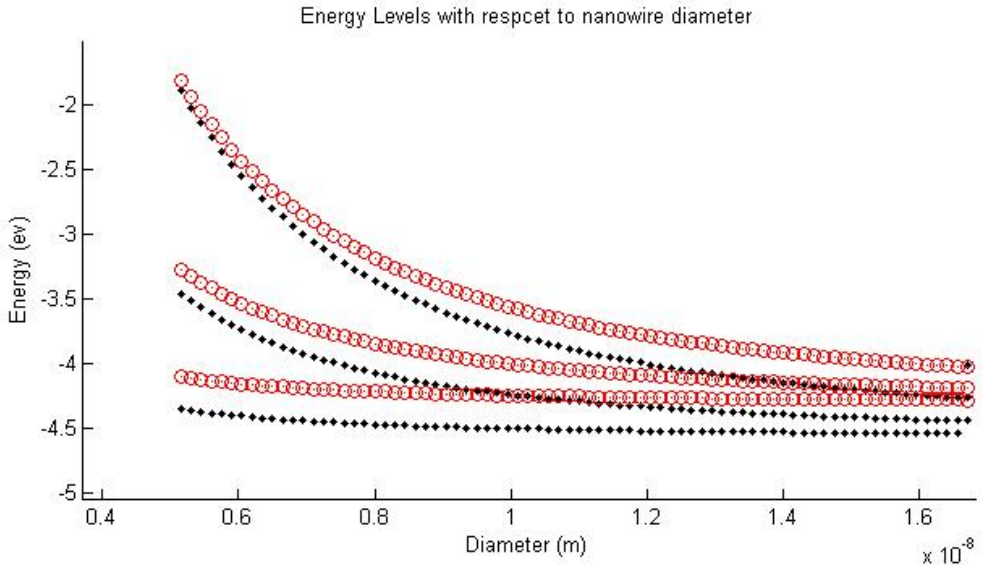

Figure 9: CdSe/CdTe energy levels with respect to diameter within a finite potential well. As is evident from the plot, the second energy level of CdSe corresponding to the first energy level of CdTe is around a diameter of 10nm. The red dots are energy levels of CdTe, while the black dots are CdSe energy bands.

Similar calculation results have been published in ref [8], and results are repeated below. Figure 9 shows a plot of the energies of the electron states (relative to E_C in CdSe) in uniform CdTe and CdSe quantum wires as a function of wire diameter. It is seen that the first excited state in the CdSe QR (denoted as 2_{CdSe}) matches the ground state in the CdTe QR (denoted as 1_{CdTe}) when the wire diameter is 10.4 nm, 3_{CdSe} matches 2_{CdTe} when the wire diameter is 14.2 nm, and 3_{CdSe} matches 1_{CdTe} when the wire diameter is 17.4 nm.

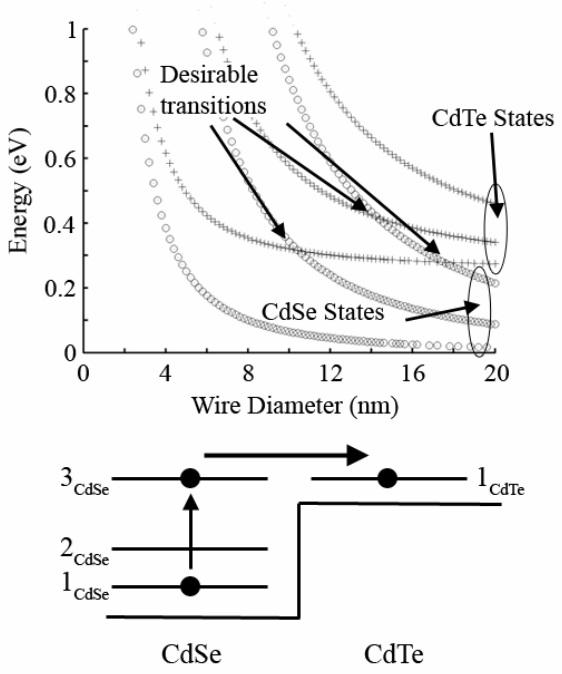

Fig. 10: The quantized electron subband levels in CdSe and CdTe conduction band. There are three promising wire radii that allow for alignment of the states. Bottom: A diagram of the $1_{CdSe} \rightarrow 3_{CdSe} \rightarrow 1_{CdTe}$ transition for a wire with diameter 17.4 nm allowing for 4.76 μm IR radiation to be detected.

These diameters (***D***) are achievable with the anodized alumina template and allow the following transitions:

D = 10.4nm: $1_{CdSe} \rightarrow 2_{CdSe} \rightarrow 1_{CdTe}$ will allow 4.83 μm IR radiation detection

D = 14.2nm: $1_{CdSe} \rightarrow 3_{CdSe} \rightarrow 2_{CdTe}$ will allow 3.17 μm IR radiation detection

$2_{CdSe} \rightarrow 3_{CdSe} \rightarrow 2_{CdTe}$ will allow 4.95 μm IR radiation detection

D = 17.4nm: $1_{CdSe} \rightarrow 3_{CdSe} \rightarrow 1_{CdTe}$ will allow 4.76 μm IR radiation detection

$2_{CdSe} \rightarrow 3_{CdSe} \rightarrow 1_{CdTe}$ will allow 7.40 μm IR radiation detection

Hence the diameter of the wire is calculated using the simplified analytical technique such that the quantum states in the active and barrier wires are aligned.

2.4 Absorption Results:

Further analysis of the wire and to understand a more complex structure than a wire requires a more advanced finite difference (FD) technique i.e. the stabilization method [33-37].

In case of a two material wire CdSe/CdTe QRIP, we with zero applied bias we have:

$$V(r,z)=\begin{cases} -\chi_{CdSe} & \text{for } r <= R \text{ and } z<0 \\ -\chi_{CdTe} & \text{for } r <= R \text{ and } z>0 \\ 0 & \text{otherwise} \end{cases} \tag{10}$$

The quantum states are expressed as a linear combination of basis functions:

$$\Psi=\sum_{m,n} a_{m,n}\varphi_{m,n} \tag{11}$$

$$\varphi_{m,n}=\sqrt{\frac{2}{\pi L_o R_o^2 J_1^2(s_m R_o)}}J_0(s_m r)\sin(k_n z) \tag{12}$$

where $s_m R_o$ are the zeros of $J_o(x)$ and $k_n = 2\pi n/L_o$. The following Hamiltonian is then diagonalized using the above basis functions:

$$H(r,z)=-\frac{\hbar^2}{2m^*(r,z)}\nabla^2+V(r,z) \tag{13}$$

The absorption $\alpha(\omega)$ can be calculated using first order perturbation theory and Fermi's golden rule. In this case, the temperature is taken to be 300°K, the CdSe is n-type, the CdTe is nonintentially doped. Thus the absorption is produced almost entirely by the CdSe portion of the quantum wire. As a first approximation, the electron distribution is assumed to obey Fermi-Dirac distribution function denoted as $F(E)$. The absorption in

this case can be written as [38]:

$$\alpha(\hbar\omega) = \frac{2\pi e^2}{n_{wire} c \varepsilon_o m_o^2 \omega V_{wire}} \sum_{f,i} \left|\hat{e} \cdot \mathbf{p}_{fi}\right|^2 L\left(\Gamma, E_f - E_i - \hbar\omega\right)\left(F(E_i) - F(E_f)\right) \tag{14}$$

where n_{wrie} and V_{wire} are the index of refraction and volume of the wire, $\hat{e}$ is the polarization of the incident light and $L\left(\Gamma, E_f - E_i - \hbar\omega\right)$ is a Lorentzian function with linewidth Γ [38]:

$$L\left(\Gamma, E_f - E_i - \hbar\omega\right) = \frac{\Gamma/2\pi}{\left(E_f - E_i - \hbar\omega\right)^2 - \left(\Gamma/2\right)^2} \tag{15}$$

Figure 11 shows the absorption for a uniform CdSe quantum wire and a CdSe/CdTe heterostructure quantum wire at 300°K. Most of the absorption in the CdSe/CdTe quantum wire is due to the CdSe, as chosen.

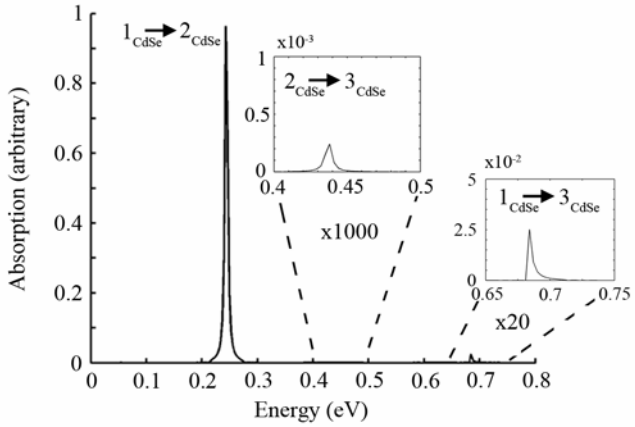

Figure 11: The absorption of a 10.4 nm diameter CdSe quantum wire. The most prominent absorption peak is due to the $1_{CdSe} \rightarrow 2_{CdSe}$ transition. The next strongest peak is the $1_{CdSe} \rightarrow 3_{CdSe}$ transition followed by the weak $2_{CdSe} \rightarrow 3_{CdSe}$. Only the $1_{CdSe} \rightarrow 2_{CdSe}$ is used in 10.4 nm diameter CdSe/CdTe because the 2_{CdSe} energy matches the 1_{CdTe} energy.

2.5 Miscellaneous Variant Structures:

The photodetector design is an immediate application that calls for heterostructures fabrication. Optical absorption of different material nanowires can be varied by varying the size and/or composition of the materials as the simulation results indicate. Figure 12 shows PL signal of the alloy $CdS_{1-x}Se_x$ with varying the value of x.. These two parameters, i.e. composition and diameter can be varied with varying experimental conditions.

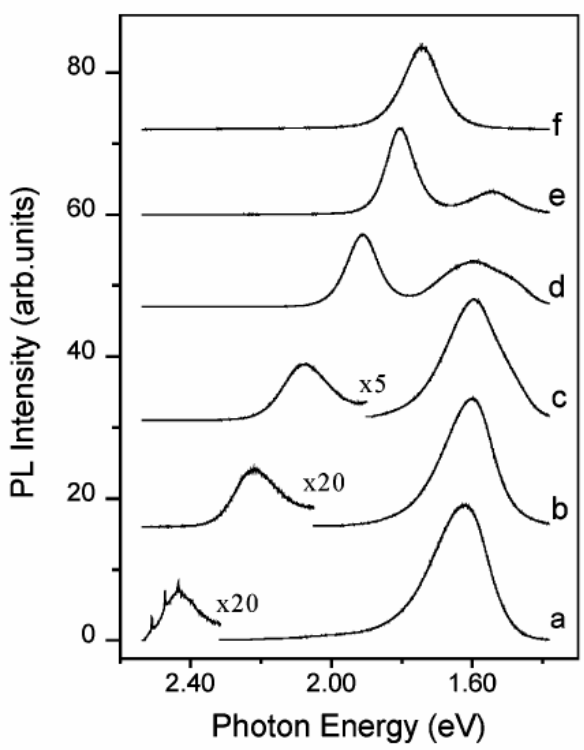

Fig. 12: PL spectra of a series of $CdS_{1-x}Se_x$ nanowires at room temperature with different *x* values: (a) 0; (b) 0.22; (c) 0.40; (d) 0.64; (e) 0.87; (f) 1.00. [39]

Utilizing alumina as a host template, more complex structures can also be fabricated i.e a variant of the basic concept may be, in addition to alloying semiconductor compounds, a structure where the entire QR is the composed of the active II-VI semiconductor (e.g.,

CdSe in this work) and a thin II-VI semiconductor film is deposited on top of the wires that will serve as the barrier layer (e.g., CdTe or $Zn_{1-x}Cd_xSe$ in this work), (2) wires that are composed of a superlattice of alternating II-VI semiconductors producing arrays of QDs. Both of these variant structures will have different optical and electronic behavior and the effects of variant structure.

The next chapter describes the theory of the electron phonon interaction briefly, which is an added advantage with these structures. This will allow for better operation with respect to temperature change, and ideally the structure should have very low noise, at room temperatures. This will be followed by experimental techniques and results. Once the basis for this type of experimental work is given, fabrication and characterization results will be given to compare with the derived theory.

Chapter 3 Formulation of Electron Phonon Interactions

3.1 Background

Some theoretical results were presented in the previous chapter relating to electron photon interactions. As we explore the benefits achieved by quantum confinement in tailoring material properties to specific device needs, it is also imperative to cover the effect on electron phonon scattering. The altered phonon modes and density of states account for enhanced confinement of the electrons to the ground state energy level in the conduction band, to a higher degree compared to bulk materials [40]. In case of a quantum wire using intersubband absorption as mentioned in previous chapter, the electron would be confined in the conduction band of the active wire. Due to quantum confinement the energy levels for the electrons as well as phonon modes are discretized. This means that phonon modes will also be spread further apart. This concept has been successfully utilized in quantum cascade lasers based on quantum well structures, wherein phonon scattering is the mechanism by which energy levels are depopulated [41]. Similarly, in quantum dots, discreteness of energy levels, suppresses relaxation via

acoustic phonons, and restricts relaxation via optical polar optical phonons to energy spacing matching the eigenenergies of polar optical phonon modes [42]. The interaction of carriers is stronger with optical phonons compared to acoustic phonons [43]. Therefore, the LO phonon assisted relaxation is faster typically in the order of a few picoseconds. This is achieved by designing the energy spacing between levels to coincide with the energy of a few LO phonons [43]. Very recently, mid IR quantum cascade laser with active regions composed of doubly resonant longitudinal optical (LO) phonon depopulation schemes have been used to demonstrate room temperature operation [44]. This favors operation in the terahertz regime as this process is very fast. In quantum dots, the relaxation occurs with the emission of acoustic phonons. Due to small carrier-acoustic phonon strength this process is much slower, and this limitation is referred to the 'phonon bottleneck' effect [45]. In the case of quantum wires, as electron phonon scattering is inhibited, a better operation with respect to temperature is expected, which would translate into lower dark current and higher sensitivity if these wires are to be used in photodetecting applications. Before a theoretical analysis of phonons is given, a brief introduction to the types of phonons is presented. A theoretical analysis of electron phonon interaction follows the introduction.

3.2 Phonons

A charge carrier, electron or hole, changes its state by a process known as scattering. It is summarized usually in terms of Fermi's Golden Rule [46]. The rule states that if an electron/hole in a state i of energy E_i experiences a time dependent perturbation which could scatter it into a final state f with energy E_f then the lifetime it will have in this final state is given by [47]

$$\frac{1}{\tau_i} = \frac{2\pi}{\hbar} \sum_f \left| \langle f | H | i \rangle \right|^2 \delta(E_f - E_i) \qquad (1)$$

As presented in previous chapter electrons are scattered by photons to higher energy levels. This difference in energy can either be given away as a photon, or in terms of lattice vibration by a emitting a phonon.

In general, the atoms in a semiconductor crystal are connected by chemical bonds. These atoms are always in a state of continual motion. This motion is vibrational around an equilibrium position, because of the crystal lattice structure. This motion even at the hypothetical absolute zero of temperature pertains, which is usually termed as the zero point energy. This motion can be compared to a classical example of system of a series of masses connected by springs. These are classified into four fundamental categories or modes of vibration, namely, longitudinal acoustic (LA), transverse acoustic (TA), longitudinal optic (LO), and transverse optic (TO) phonon modes. These modes are shown in Figures 1 and 2.

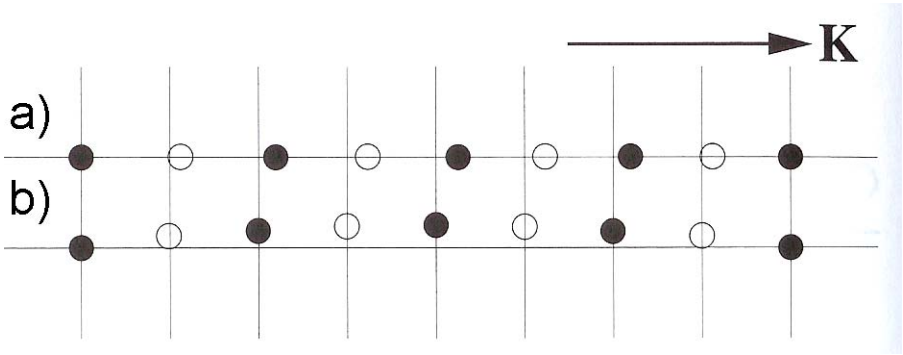

Figure 13: Acoustic Phonon Modes [47]

The acoustic modes shown in Figure 13, are characterized as neighboring atoms being in phase while vibrating. The longitudinal acoustic mode is characterized by atomic

displacement being in the same direction as energy transfer, while in transverse mode the atomic displacements are perpendicular. In case of longitudinal and transverse optic modes, the lattice vibration displaces the neighboring atoms in opposite phase, as shown in Figure 14.

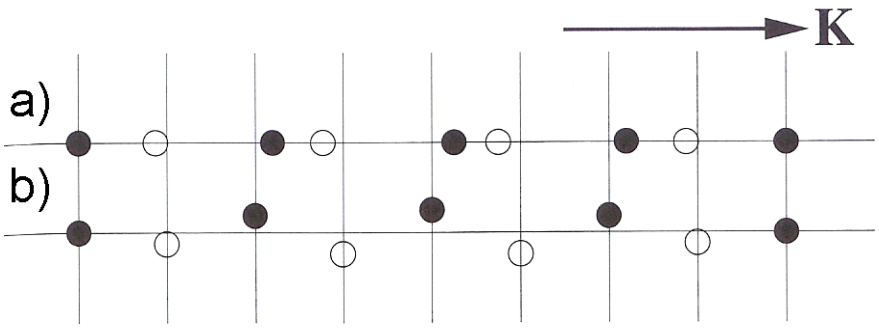

Figure 14: Optical Phonon Modes [47]

Due to the wave like nature of the lattice vibration, they can be described by angular frequency ω, and a wave vector K. In this way, the energy of a phonon is ħω, similar to a photon of light. Analogous to propagating electrons, the momentum of a photon is said to be quantized with value ħK. In addition to these properties, phonons are diffracted by crystal lattice in a manner similar to electrons or holes, hence, Brillouin zone type of energy momentum curves can be employed to study the diffraction. For different semiconductors the form of the curves may be similar with differing energy scales [48]. Theoretical analysis of the electron phonon interactions is given next.

3.3 Formulation of electron phonon interactions in cylindrical quantum wires

The macroscopic analysis of phonon modes starts from Maxwell's equations describing classical electrodynamics

$$\nabla \cdot \mathbf{D}(\mathbf{r}) = 4\pi\rho_{o}(\mathbf{r}) \qquad (2)$$

$$D_i(\mathbf{r}) = \varepsilon_{ij} E_j(\mathbf{r}) = E_i(\mathbf{r}) + 4\pi P_i(\mathbf{r}) \tag{3}$$

$$\mathbf{E}(\mathbf{r}) = -\nabla\varphi(\mathbf{r}) \tag{4}$$

$$P_i(\mathbf{r}) = \chi_{ij} E_j(\mathbf{r}) \tag{5}$$

where $\mathbf{E}(\mathbf{r})$, $\mathbf{D}(\mathbf{r})$, $\mathbf{P}(\mathbf{r})$, $\varphi(\mathbf{r})$, $\rho_o(\mathbf{r})$, ε_{ij} and χ_{ij} are the electric field, electric displacement, electric polarization, electric scalar potential, free charge density, dielectric constant tensor and electric susceptibility tensor (using Einstein summation convention) respectively. For no external charges, namely $\rho_o(\mathbf{r}) = 0$, Eqs. (2)- (4) lead to

$$\nabla \cdot \mathbf{D}(\mathbf{r}) = \varepsilon \nabla^2 \varphi(\mathbf{r}) = 0 \tag{6}$$

$\varepsilon(\omega)$ can be written in the usual way

$$\varepsilon(\omega) = \varepsilon_\infty \frac{\omega^2 - \omega_{LO}^2}{\omega^2 - \omega_{TO}^2} \tag{7}$$

where ε_∞ is the high frequency dielectric constant and $\omega_{LO} = \omega_{TO}\sqrt{\varepsilon_o / \varepsilon_\infty}$, as given by the Lyddane-Sachs-Teller relation.

Before we go further in the theory of the modes, let us briefly discuss the effect of the scales on the dielectric function of a material. The dielectric function has been studied in terms of the random phase approximation (RPA) [49], local density approximation (LDA) [50], and using density functional theory (DFT) [51]. We are interested in how the dielectric constant changes with nanoparticle size, and how dramatic this increase will be if we are to model optical and electrical properties of devices accurately. As we are also studying the phonon modes and electron-phonon interactions, this analysis makes more sense. This can be seen in equation (6), and in later derivations, that there is a strong dependence on the dielectric function for calculation of the phonon modes. Therefore, it

is very important to model the dielectric function and include an accurate estimate to get correct results, in the case of nanostructures in general. Theoretical and experimental evidence supports the fact that the dielectric constants within quantum dots are significantly reduced from their bulk values. The origin of the decrease is not well understood. This was originally attributed to the bandgap increase in side the quantum dot. This would lower the polarizibility in the surface region. Recently, Delerue et al. argued that the effect of the quantum dot boundary should only be felt close the surface, hence claiming that the reduction in average value the dielectric constant is only a surface effect and is not due to the opening of the gap but to a breaking of polarizable bonds at the surface [52]. Xavier Cartioxa, et al. have modeled the microscopic dielectric function for quantum dots, and found that the dielectric response function is bulklike within the quantum dots, confirming the claim of Delerue et al [53] For further analysis we will assume the dielectric constant to have the bulk value. We will describe LO and SO modes, as TO modes are not of interest for our work.

3.3.1 LO Phonon Modes – Macroscopic Approach

LO modes have a frequency $\omega = \omega_{LO}$, assuming no dispersion, and are described by functions that satisfy the following electrostatic boundary conditions

$$\mathbf{D} = 0 \qquad 0 \le \rho \le \infty \tag{8}$$

$$\mathbf{E} = 0 \qquad R \le \rho \le \infty \tag{9}$$

Using separation of variables and solving for $\mathbf{E}_{nm}(\mathbf{r})$ and $\mathbf{P}_{nm}(\mathbf{r})$ we get

$$\mathbf{E}_{nm}(\mathbf{r}) = \begin{cases} e^{i(m\phi+kz)}\left(\frac{\alpha_{0n}}{R}J_1\left(\frac{\alpha_{0n}}{R}\rho\right)\hat{\rho} - \frac{im}{\rho}J_0\left(\frac{\alpha_{0n}}{R}\rho\right)\hat{\phi} - ikJ_0\left(\frac{\alpha_{0n}}{R}\rho\right)\hat{z}\right) & \rho \le R \\ 0 & \rho \ge R \end{cases} \tag{10}$$

$$\mathbf{P}_{nm}(\mathbf{r}) = -\frac{1}{4\pi}\mathbf{E}_{nm}(\mathbf{r}) \tag{11}$$

3.3.2 SO Phonon Modes – Macroscopic Approach

When $\varepsilon(\omega) \neq 0$, Eq. (6) is satisfied when $\nabla^2 \varphi = 0$. Solving for the electric and polarization fields, in this case yields.

$$\mathbf{E}_n(\mathbf{r}) = \begin{cases} -c_n e^{i(n\phi + k_n z)}\left(\frac{k}{2}\left(I_{n+1}(k\rho) + I_{n-1}(k\rho)\right)\hat{\rho} + \frac{in}{\rho} I_n(k\rho)\hat{\phi} + ikI_n(k\rho)\hat{z}\right) & \rho \leq R \\ d_n e^{i(n\phi + k_n z)}\left(\frac{k}{2}\left(K_{n+1}(k\rho) + K_{n-1}(k\rho)\right)\hat{\rho} - \frac{in}{\rho} K_n(k\rho)\hat{\phi} - ikK_n(k\rho)\hat{z}\right) & \rho \geq R \end{cases} \tag{12}$$

$$\mathbf{P}_n(\mathbf{r}) = \chi \mathbf{E}_n(\mathbf{r}) \tag{13}$$

where χ will be calculated in the microscopic analysis. The terms c_n and d_n are determined using boundary conditions at $\rho = R$ and a ω versus k relationship is obtained

$$d_n = \frac{I_n(kR)}{K_n(kR)} c_n \tag{14}$$

$$\varepsilon(\omega)\frac{I_{n+1}(kR) + I_{n-1}(kR)}{I_n(kR)} = -\frac{K_{n+1}(kR) + K_{n-1}(kR)}{K_n(kR)} \tag{15}$$

Using the above equation, one can plot the SO phonon modes, for a wire radius of 5 nm, in units of eV, vs. wavevector kz is given in Figure 15.

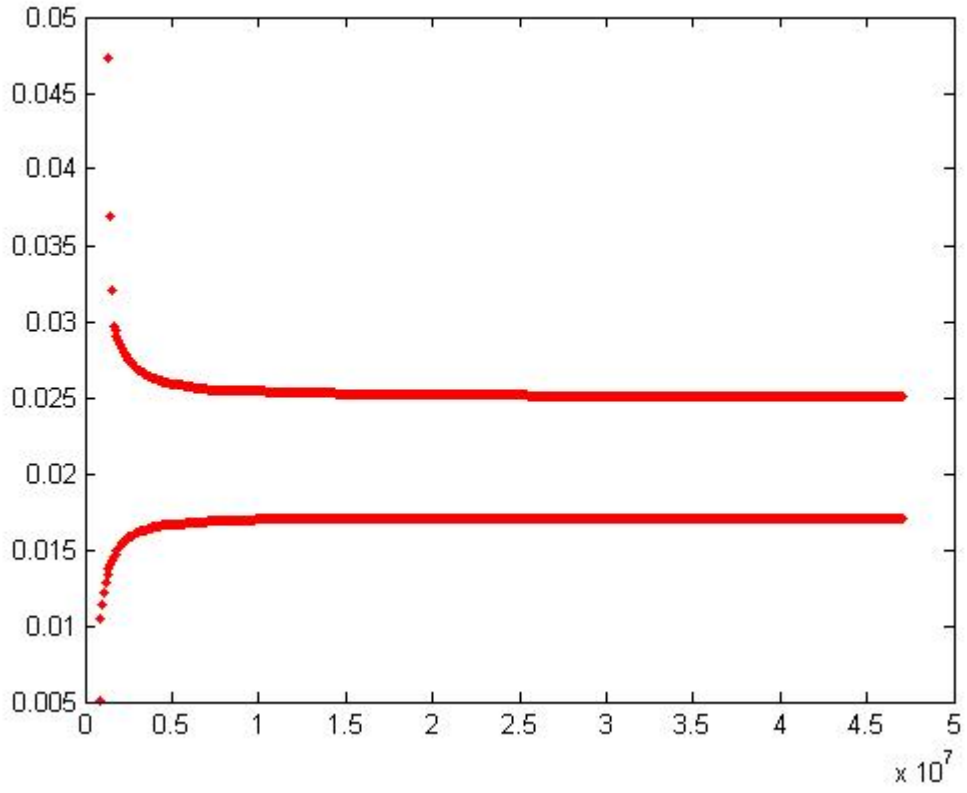

Figure 15: Phonon modes vs. kz, Energy is eV for a quantum wire of 5 nm radius.

.

3.3.3 Reformulating the Macroscopic Equations

The equations in the macroscopic approach can be expressed in a different way and will be compared with the equations obtained using the microscopic approach. If $\rho_o = 0$ throughout all space, i.e., the quantum wire and any material surrounding the quantum wire, then Eq. (2) and Eq. (3) can be expressed as

$$\nabla \cdot \mathbf{E}(\mathbf{r}) = -4\pi \nabla \cdot \mathbf{P}(\mathbf{r}) \tag{16}$$

$$\nabla^2 \varphi(\mathbf{r}) = 4\pi \rho_{pol}(\mathbf{r}) \tag{17}$$

where $\rho_{pol}(\mathbf{r}) = -\nabla \cdot \mathbf{P}(\mathbf{r})$ is the polarization charge density and includes all possible

microscopic contributions to the electric field from ions within the wire and the surrounding medium. Taking the Fourier transform and rearranging terms we can include all scalar and vector component contributions in an equation form. The general form of the Fourier transform is given by the equation.

$$S(r) = \frac{L}{2\pi}\int dk S(k,\rho)e^{ikz} \tag{18}$$

Here L is the length of the wire. Equation (17) becomes

$$\left(\nabla_{2D}^2 - k^2\right)\varphi(k,\boldsymbol{\rho}) = -4\pi\rho_{pol}(k,\boldsymbol{\rho}) \tag{19}$$

where $\nabla_{2D}^2 = \partial^2/\partial x^2 + \partial^2/\partial y^2$. The solution to this nonhomogeneous differential equation can be expressed using a Green's function $G(k,\rho_0 - \rho)$

$$\phi(k,\rho_0) = -4\pi\int G(k,\rho_0 - \rho)\rho_{pol}(k,\rho)dA \tag{20}$$

The Green's function is given in the two dimensional form for the modified Helmholtz's operator

$$G(k,\rho_0 - \rho) = \frac{1}{2\pi}K_0(k|\rho - \rho_0|) \tag{21}$$

Taking the gradient of the left hand side of Eq. (20), and expressing E(r) in terms of P(r), using integration by parts, the following equations:

$$\frac{1}{2\chi}P_i(k,\boldsymbol{\rho}_o) = \int_{all\ space} T_{ij}\left(k,|\boldsymbol{\rho}_o - \boldsymbol{\rho}|\right)P_j(k,\boldsymbol{\rho})d\vec{A} \tag{22}$$

$$T_{xx}(k,|\rho_0 - \rho|) = \frac{\partial}{\partial x}\frac{\partial}{\partial x}K_0(k|\rho_0 - \rho|), \tag{23}$$

$$T_{xy}(k,|\rho_0 - \rho|) = T_{yx}(k,|\rho_0 - \rho|) = \frac{\partial}{\partial x}\frac{\partial}{\partial y}K_0(k|\rho_0 - \rho|), \tag{24}$$

$$T_{xz}(k,|\rho_0 - \rho|) = T_{zx}(k,|\rho_0 - \rho|) = -ik\frac{\partial}{\partial x}K_0(k|\rho_0 - \rho|), \tag{25}$$

$$T_{yy}(k,|\rho_0-\rho|=\frac{\partial}{\partial y}\frac{\partial}{\partial y}K_0(k|\rho_0-\rho|), \tag{26}$$

$$T_{yz}(k,|\rho_0-\rho|)=T_{zy}(k,|\rho_0-\rho|)=-ik\frac{\partial}{\partial y}K_0(k|\rho_0-\rho|), \tag{27}$$

$$T_{zz}\left(k|\rho_0-\rho|\right)=-k^2K_0(k|\rho_0-\rho|), \tag{28}$$

A microscopic analysis for a similar result follows. The displacement of positive and negative ions can be written as $\mathbf{u}_+(\mathbf{r},t)$ and $\mathbf{u}_-(\mathbf{r},t)$ respectively and the relative displacement as $\mathbf{u}(\mathbf{r},t)=\mathbf{u}_+(\mathbf{r},t)-\mathbf{u}_-(\mathbf{r},t)$. The equation of motion for the relative displacement of the positive and negative ions is

$$\mu\frac{d^2\mathbf{u}(\mathbf{r},t)}{dt^2}=-\mu\omega_o^2\mathbf{u}(\mathbf{r},t)+e\mathbf{E}^l(\mathbf{r},t) \tag{29}$$

where $\mu=M_+M_-/(M_++M_-)$ is the reduced mass of the ion pair, ω_o is the frequency associated with the short-range force between ions, and $\mathbf{E}^l(\mathbf{r},t)$ is the local field. The oscillating ions produce a polarization field according to the equation

$$\mathbf{P}(\mathbf{r},t)=ne\mathbf{u}(\mathbf{r},t)+n\alpha\mathbf{E}^l(\mathbf{r},t) \tag{30}$$

Fuchs and Kliewer [54], used three regions in their work for evaluating the local electric field is calculated by splitting up the material into three regions. The total contributions from regions I and II are calculated and in integral form correspond to

$$E_i(\mathbf{r}_o,t)=\int_{I,II}Q_{ij}(\mathbf{r}_o-\mathbf{r})P_j(\mathbf{r})d\mathbf{V} \tag{31}$$

The full macroscopic electric field $\mathbf{E}(\mathbf{r},t)$ that is used in the Lorentz relation [55]

$$\mathbf{E}^l(\mathbf{r},t)=\mathbf{E}(\mathbf{r},t)+\frac{4\pi}{3}\mathbf{P}(\mathbf{r},t) \tag{32}$$

where $\mathbf{E}^l(\mathbf{r}_o,t)$ is the local electric field. With Eq. (31), Eq. (32) can be written as

$$E_i^l(\mathbf{r}_o,t)=\gamma_{ij}P_j(\mathbf{r}_o,t)+\int Q_{ij}(\mathbf{r}_o-\mathbf{r})P_j(\mathbf{r})d\mathbf{V} \tag{33}$$

where γ_{ij} is the Lorentz factor and is written as $\gamma_{ij}=\delta_{ij}4\pi/3$ with *i, j =(x,y,z)* for materials with cubic symmetry, and only depends on symmetry of the material [56]. Solving further yields

$$\frac{(\Gamma_{ij}-\xi_{ij})}{2}P_j(k,\boldsymbol{\rho}_o)=\int_{all\ space} T_{ij}(k,|\boldsymbol{\rho}_o-\boldsymbol{\rho}|)P_j(k,\boldsymbol{\rho})d\mathbf{A} \tag{34}$$

Where $T_{ij}(k,|\rho_0-\rho|)$ are given by Eqs. (23)-(28). Once $\mathbf{P}(\mathbf{r})$ has been obtained using Eq. (34), $\mathbf{E}^l(\mathbf{r})$ can be expressed as

$$\mathbf{E}^l(\mathbf{r})=\frac{4\pi}{3}\frac{\varepsilon(\omega)+2}{\varepsilon(\omega)-1}\mathbf{P}(\mathbf{r})=\kappa(\omega)\mathbf{P}(\mathbf{r}) \tag{35}$$

LO Modes: $$\mathbf{E}^l(\mathbf{r})=-\frac{8\pi}{3}\mathbf{P}(\mathbf{r}) \tag{36}$$

TO Modes: $$\mathbf{E}^l(\mathbf{r})=\frac{4\pi}{3}\mathbf{P}(\mathbf{r}) \tag{37}$$

SO Modes: $$\mathbf{E}^l(\mathbf{r})=\kappa_{SO}\mathbf{P}(\mathbf{r}) \tag{38}$$

Where κ_{SO} is the coefficient of $\mathbf{P}(\mathbf{r})$ in Eq. (35) evaluated at a frequency $\omega=\omega_{SO}$ where ω_{SO} satisfies Eq. (15). For a general k(w) we can write the following relation between $\mathbf{u}(\mathbf{r})$ and $\mathbf{P}(\mathbf{r})$

$$\mathbf{u}(\mathbf{r})=\frac{1-n\alpha\kappa(\omega)}{ne}\mathbf{P}(\mathbf{r})=\frac{\theta(\omega)}{ne}\mathbf{P}(\mathbf{r}) \tag{39}$$

where $\theta(\omega)=1-n\alpha\kappa(\omega)$.

3.3.4. Quantization of the phonon modes and Electron Phonon Interactions

A method of quantizing the phonon modes similar to that used by Wendler [57] in their analysis of phonons in 2D dielectric slabs and Trallero-Giner et al. [58] in their analysis of phonons in arbitrarily shaped nanostructures will be performed in this work on 1D quantum wires. The Hamiltonian density can easily be derived from the equation of motion, Eq. (29) and is

$$h_p = \frac{1}{2}\sum_i \left(\frac{1}{n\mu}\Pi_i(\mathbf{r})\Pi_i(\mathbf{r}) + n\mu\omega_o^2 u_i(\mathbf{r})u_i(\mathbf{r}) - neu_i(\mathbf{r})E_i^l(\mathbf{r}) \right) \tag{40}$$

where $\vec{\Pi}(\mathbf{r}) = n\mu\dot{\mathbf{u}}(\mathbf{r})$ is the conjugate momentum. The Hamiltonian is then the integral over all space of h_p

$$H_p = \frac{1}{2}\sum_i \int dV \left(\frac{1}{n\mu}\Pi_i(\mathbf{r})\Pi_i(\mathbf{r}) + n\mu\omega_o^2 u_i(\mathbf{r})u_i(\mathbf{r}) - neu_i(\mathbf{r})E_i^l(\mathbf{r}) \right) \tag{41}$$

The terms $\vec{\Pi}(\mathbf{r})$ and $\mathbf{u}(\mathbf{r})$ in Eq. (41) are 1D Fourier transformed over a discrete set of k values by using Eq. (18) and replacing the integral with a summation that includes Born-von Karman periodic boundary conditions: $L/2\pi \int dk \to \sum_k$. Eq. (41) can be expressed in the following form after using Eqs. (32) and (39).

$$H_p = \sum_k H_k \tag{42}$$

with

$$H_k = \frac{1}{2}\sum_{i,m} \left\{ \int \left(\sqrt{\frac{L}{n\mu}}\Pi_i^m(k,\boldsymbol{\rho}) \right)^* \left(\sqrt{\frac{L}{n\mu}}\Pi_i^m(k,\boldsymbol{\rho}) \right) d\mathbf{A} + \omega_m^2 \int \left(\sqrt{n\mu L}u_i^m(k,\boldsymbol{\rho}) \right)^* \left(\sqrt{n\mu L}u_i^m(k,\boldsymbol{\rho}) \right) d\mathbf{A} \right\} \tag{43}$$

$$\omega_m^2 = \omega_o^2 - \frac{\omega_p^2}{4\pi}\frac{\kappa(\omega_m)}{\theta(\omega_m)} \tag{44}$$

For normalization, recall that the system is composed of N coupled oscillators each with

kinetic energy and potential energy with the latter being proportional to $|\mathbf{u}(\mathbf{r}_i)|^2$ for each ion pair at $\mathbf{r}_i$. With the energy of each ground state phonon mode being $E = \hbar\omega_m/2$ and with the virial theorem (stating that expectation value of the total kinetic energy $\langle T \rangle$ is related to the expectation of the total potential energy $\langle U \rangle$ by the equation $\langle T \rangle = k/2 \cdot \langle U \rangle$, with $k = 2$ for this coupled oscillators situation), the following equation for $\langle U \rangle$ can be obtained that produces the correct normalization procedure

$$n\mu L \int \left(\mathbf{u}^m(k,\boldsymbol{\rho})\right)^* \cdot \left(\mathbf{u}^m(k,\boldsymbol{\rho})\right) d\mathbf{A} = \frac{\hbar}{2\omega_m} \tag{45}$$

Eq. (45) properly normalizes $\mathbf{u}^m(k,\boldsymbol{\rho})$, and $\varphi^m(k,\boldsymbol{\rho})$, the eigenvectors that form the basis for the expansion of $\mathbf{u}(k,\boldsymbol{\rho})$ and $\varphi(k,\boldsymbol{\rho})$ in the second quantization:

$$\mathbf{u}(k,\boldsymbol{\rho},t) = \sum_m \left(a_m(k)\mathbf{u}^m(k,\boldsymbol{\rho})e^{i\omega_m t} + a_m^\dagger(-k)\mathbf{u}^{m^*}(k,\boldsymbol{\rho})e^{-i\omega_m t} \right) \tag{46}$$

$$\varphi(k,\boldsymbol{\rho},t) = \sum_m \left(a_m(k)\varphi^m(k,\boldsymbol{\rho})e^{i\omega_m t} + a_m^\dagger(-k)\varphi^{m^*}(k,\boldsymbol{\rho})e^{-i\omega_m t} \right) \tag{47}$$

Once the phonon eigenvectors have been properly normalized, the electron-phonon interaction can be developed. The interaction Hamiltonian can be expressed as:

$$\begin{aligned} H^{ep}(\mathbf{r}) &= -e\varphi(k,\boldsymbol{\rho}) \\ &= \sum_k H_k^{ep}(\boldsymbol{\rho}) = -e\sum_m \left(a_m(k)\varphi^m(k,\boldsymbol{\rho})e^{i(kz+\omega_m t)} + a_m^\dagger(-k)\varphi^{m^*}(k,\boldsymbol{\rho})e^{-i(kz+\omega_m t)} \right) \end{aligned} \tag{48}$$

Eq. (48) is the correct form for the electron-phonon interaction Hamiltonian that can be used with the electron states described in detail by Crouse [8] and Fermi's golden rule, as done in Ref. [59-61] to calculate electron-phonon scattering rates.

Summary:

We have presented a brief theoretical account of electron phonon interactions. These results can be utilized in simulating the effect of these interactions on absorption spectra.

Chapter 4 Anodization of Aluminum, and Optimization of The Multilayer Template

4.1 Anodization Background

Anodization of is the process of oxidation of aluminum. In this process, the growth of an oxide on the surface of the biased conductive solid (e.g. semiconductor wafer) immersed in a liquid electrolyte or, generally in a gas discharge, is stimulated by the flow of electric current. The process has been well researched mostly in connection with corrosion prevention, and this material was initially characterized by Keller et al [62]. The following spontaneous chemical reactions occur at the surface of aluminum when exposed to oxygen or pure water.

$$2Al + \frac{3}{2}O_2 \rightarrow Al_2O_3 \quad (1)$$

or

$$2Al + 3H_2O \rightarrow Al_2O_3 + 3H_2 \quad (2)$$

Aluminum oxide when interacted with acids, dissolves by the following process:

$$Al_2O_3 + H_2O + 2H^+ \rightarrow 2Al(OH)_2^+$$
$$Al(OH)_2^+ + H^+ \rightarrow Al(OH)^{2+} + H_2O \quad (3)$$
$$Al(OH)^{2+} + H^+ \rightarrow Al^{3+} + H_2O$$

These two processes of oxidation and dissolution describe anodization. Typically anodic alumina is oxidized in a chamber filled with an acid, e.g. sulfuric, phosphoric or oxalic acid. A dc bias is applied between the aluminum film and a counter electrode. This bias ensures a constant supply of energy so that oxidation and dissolution occur simultaneously. The above mentioned process is not only of conversion of the aluminum to a hydrated aluminum oxide alumina, but also of the film transforming to a hexagonal array of cylindrical pores as shown in Figure 16. The top view shows that the pores have a hexagonal arrangement.

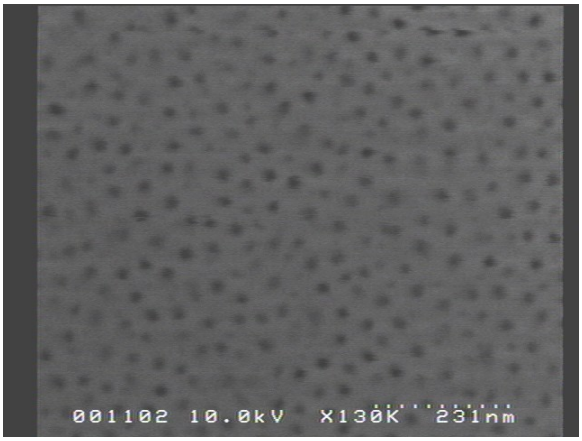

Figure 16: SEM image of anodized aluminum sample at 25V in 0.5M sulfuric acid, at 10C, Pore diameter is approximately 25nm

As mentioned above, anodization of aluminum has been thoroughly studied after the initial use as corrosion prevention [62]. Masuda and Fakuda were the first to report an ordered porous arrangement in porous anodic alumina in 1996, and its possible use as a template for nanowire deposition [63]. Other templates that have been employed for

nanowire growth are nuclear track etched polycarbonate membranes, nanochannel array glasses, and mesoporous channel hosts [64]. The advantage porous alumina has over other templates, is that it is a wide bandgap material and optically transparent. Additionally, it is a low cost and fast technique to produce large arrays of identical entities, with a very large aspect ratio (length divided by diameter), which is not possible with conventional lithographic techniques [65]. Anodic template and nanowires deposited within, compared to polycarbonate membranes, also has the advantage of being parallel to each other, and perpendicular to the membrane surface, with an assumed constant diameter throughout their length [65].

The pore arrangement is roughly hexagonal, as can be seen in Figure 16. The regularity and periodicity in the pore arrangement can be improved by pre-patterning the surface of the aluminum by a SiC stamping process similar to the on used by Masuda et al [66], or by by chemicals, and then anodization is carried out again on this aluminum, that now has a pattern, where the pore growth will take place preferentially at the sites of previously terminating pores. Anodization can give high quality porous templates. In addition, the pore size and spacing can be controlled very easily by the voltage and other experimental parameters, and follow an empirical relation [23]. In 1970, O'Sullivan and Wood presented a model for the porous arrangement by self regulation. This model described how the electric field distribution at the pore tips affects pore growth, and the reason for the narrow size distribution.[68] Further models are good microscopic explanations for the dependence of pore diameters, interpore distances on applied voltage or electrolyte combination. [69-71].

4.1.1 The Mechanical Stress Model

Very recently have new models have been proposed that explain the expansion and pore formation phenomenon [72-73]. The steps during anodization starting with the oxide formation on the surface, continuing with the distribution of electric field to the steady state pore formation regime is shown in Figure 17. The mechanical stress model describes these steps as follows [73]:

1. Oxidation takes place at the entire metal/oxide interface primarily due to the migration of oxygen containing ions (O^{2-} or OH^-) from the electrolyte.
2. There is dissolution and thinning of the oxide layer due to the hydration reaction of the formed oxide layer.
3. If there is no pore formation, all Al^{3+} ions reaching the electrolyte/oxide interface contribute to oxide formation. Porous alumina is formed when Al^{3+} ions drift through the oxide layer. Some of them come back to the electrolyte without contributing to the oxide formation.
4. Pore growth perpendicular to the surface, takes place when field enhanced dissolution at the electrolyte/oxide interface is in equilibrium with oxide growth at the oxide/metal interface.
5. The formed alumina is assumed to be Al_2O_3, in which case the aluminum composition has an atomic density lower by a factor of 2 to metallic aluminum. The volume of anodized alumina expands to be twice the original volume.
6. This volume expansion results in a compressive stress during the oxide formation in the oxide/metal interface. The expansion in the vertical direction therefore pushes the pore walls upwards.

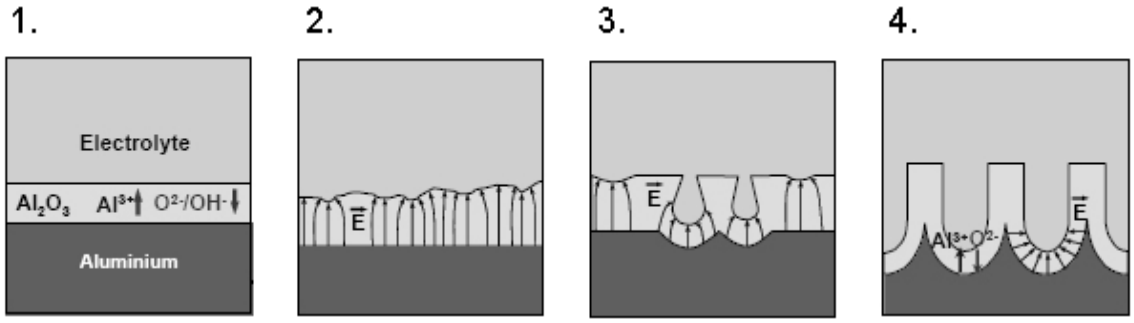

Figure 17: Schematic of pore formation at the beginning of the anodization. Step 1. Formation of the barrier oxide on the entire area. Step 2. Local field distribution caused by the surface fluctuations. Step 3. Creation of pores by field and/or temperature dependent dissolution. Step 4. Stable Pore Growth.

The current curve for a typical anodization at 25 V dc in a solution of 0.5 M sulfuric acid is given in Fig. 18 .

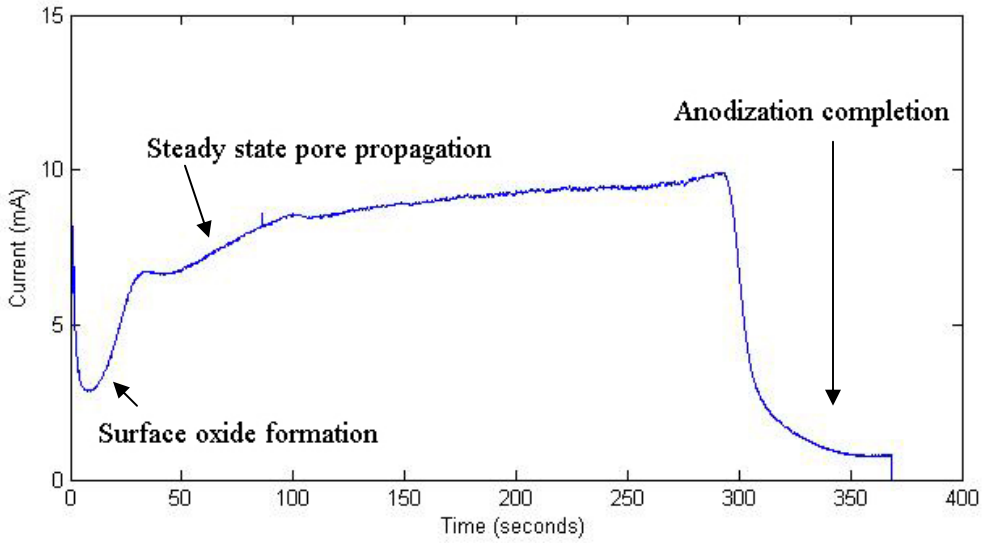

Figure 18: Anodization Curve with respect to time for Aluminum in 0.5M H_2SO_4. The three regions, i.e. surface oxide formation, steady state pore propagation and anodization completion are clearly visible

The oxide formation, steady state pore propagation and anodization termination are clearly observable in the profile. The type and concentration of the electrolyte has to be chosen according to the applied potential for self ordered growth. Usually, anodization is carried out in sulfuric acid for low potential ranges (5~40V), in oxalic acid for medium potential ranges (30V~120V) and phosphoric acid for high potential ranges (80~200V). This restriction is mainly due to the conductivity and pH value of the electrolyte. As sulfuric acid has high conductivity, if anodization is carried out in sulfuric acid at high potential, breakdown of the oxide layer is very likely. In addition the pH value determines the size of the pores. A lower pH value translates into a lower potential threshold for field enhanced dissolution at the pore tip. This results in lower pore sizes.

The recent studies in anodization of alumina have been for modification of the porous arrangement by varying experimental parameters [74], and pore spacing in the range of 50nm to 420nm by varying the parameters of anodization was done by Li et al [75]. Low potential anodization (30-60V) in 0.3M oxalic acid at 2°C result in pore distances of 50-150nm. In phosphoric acid with a concentration of 10% by weight at 3°C interpore distances in the range 300nm-420nm can be obtained. As a rule it can be estimated that pore diameter is around 30% f interpore distance [76]. Further increase is possible by pore widening etch in phosphoric acid, NaOH, or other acidic solutions, for which calibration needs to be done, as both of these chemicals may etch the template away completely [77]. For phosphoric acid solutions, regularity of the nanoporous array depends on the the anodic voltage and acid concentration [78].

4.1.2 The 10% Porosity Rule

Anodization parameters usually determine the regularity, size and interpore spacing, and

recently a study on the optimal parameters has been given in [76]. The porosity of a hexagonal structure is given by the following relation [76] under optimal conditions.

$$P = \frac{2\Pi}{\sqrt{3}}\left(\frac{r}{D_{\text{int}}}\right)^2 \tag{4}$$

Empirical relations exist for the ratio $\frac{r}{D_{\text{int}}}$. It is also reported that the pore diameter is affected by dissolution velocity that is directly related by the pH of the solution [76]. The lower the pH, the stronger the acid, and the lower the potential threshold for field enhanced dissolution at the pore tip. The above equation can be rewritten for self ordered growth as:

$$U = \sqrt{\frac{2\Pi}{\sqrt{3}P}}\frac{r}{k} \tag{5}$$

Where k is a proportionality constant and is approximately 2.5nm/V [76]. Nielsch et al. also claim that there is an optimal anodization time to obtain largest pore size, and that for longer times, the pore diameter may not remain the same, and an increase in current for longer time is possibly due to the change of the pH tip at the oxide solution interface, where the flow of ions becomes diffusion limited [76].

4.2 Pore Diameter Study

Anodization voltage effectively controls the diameter of the porous structure as mentioned earlier [76]. We need to have good control over this parameter as it is going to control the diameter of the materials deposited within. Two approaches were used, namely variation in voltage, and a chemical etch procedure and are described next.

4.2.1 Variation in Voltage

We have used two techniques for obtaining alumina template with different pore sizes.

Keeping all experimental parameters such as pH of the electrolyte, temperature and type of electrolyte the same, but varying the anodization voltage only, we want to see the variation in pore diameters, and quality of the pores. Anodization was carried out at four different voltages 10V, 15V, 20V, and 25V. Samples were imaged by an SEM as seen in Figure 19.

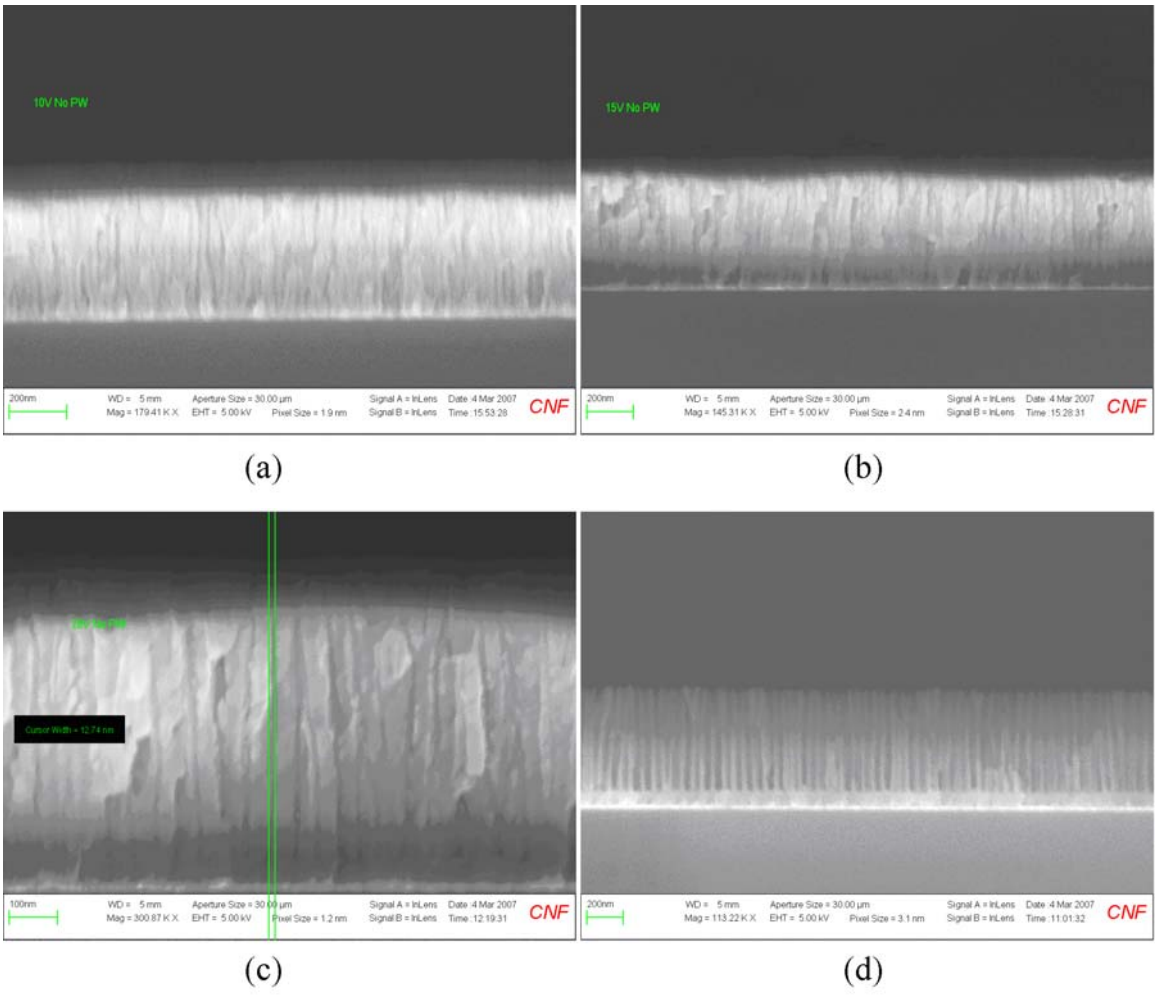

Figure 19: (a) 10V anodization, no PW sample shows poor uniformity of the pores. (b) 15V anodization, no PW. (c) 20V anodization, no PW. (d) 25V anodization, 20min PW shows nice straight pores.

The samples for 10V, 15V, and 20V, have low pore quality. The pores do not propagate

in a straight manner from the top to the base, and pore cleaning may not be able to fix that As seen in Figure 19, the 25V anodization samples show the best quality.The results indicate that the best overall results are obtained by employing a 25V voltage as seen in Figure 19(d). At lower voltages the pores are either not straight either at the surface or do not propagate perpendicularly to the base. Employing a short pore cleaning chemical etch using phosphoric acid. As can be seen the pore propagate to the bottom of the sample, however there is a barrier at the base. This issue will be addressed and resolved in later sections.

4.2.2 Chemical Etch Pore Widening Procedure:

At this point it is required to come up with a procedure with which we can vary the diameter of the pores. Phosphoric acid has been widely used as an etching solution for pore cleaning and oxide removal. If the sample is subjected to the solution for varying periods of time, it is possible to get different pore diameters for one particular voltage. This process was studied in detail Measurements taken from SEM images of anodized samples etched at 25^{o}C in 0.52M phosphoric acid (shown in Figure 20) allowed us to determine an average pore diameter for a given samples. Multiple pore diameters were measured for a given sample, and an average pore diameter then calculated.

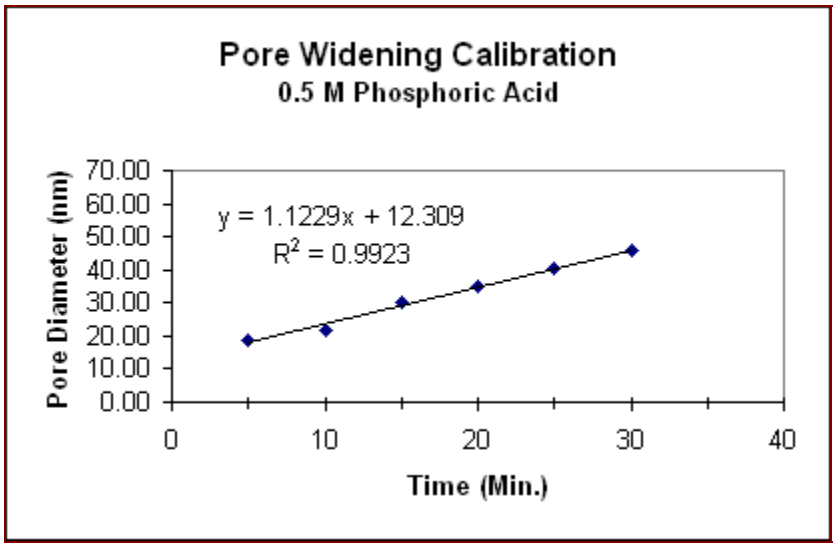

Figure 20: Pore widening calibration curve showing Etch Time vs. pore diameter for 5% w.t. phosphoric acid

These measurements were used to develop the calibration curve shown in Figure 20, which demonstrates a linear relationship between etch time and pore diameter. This relationship shows that by etching anodized samples for varying periods of time, it is possible to vary the pore diameter within a specified range.

4.3 Anodized Alumina Template Study

The motivation for use of alumina as a template for nanowire growth is that it is a wide bandgap material and optically transparent [79]. Large arrays of identical entities, with a very large aspect ratio (length divided by diameter) can be fabricated cost effectively, which is not possible with conventional lithographic techniques. This is a favorable characteristic for nanowires that are to be used in photodetection devices such as focal plane arrays [22].

Different material nanowires have been grown in alumina, including metals semiconductors, alloys, compounds and heterostructures of the same, using different

techniques [80]. Electrodeposition, in alumina membranes is made possible by a material present at the base that could be used as an electrode. At the termination of anodization of aluminum, the material has a concave or convex oxide barrier layer at the base, depending on the anodization conditions [23]. This is shown in Figure 21.

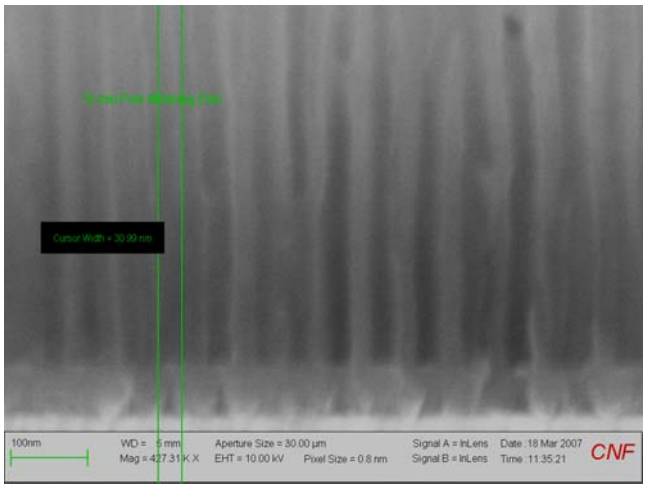

Figure 21: SEM image of alumina layer of anodized nanotemplate. Vertical lines show coincide with pore diameter

In this case, high potentials are needed by electrons to tunnel through the thick barrier layer. Sudden electrical breaking of the barrier may leads to a thermal shock that can break the barrier layer and disrupt the deposition. DC electrodeposition in the presence of a barrier is also not favorable as it is very unstable. because of the increment of the pH at the cathodic site, which leads to partial removal of the barrier layer [81]. This reduces the resistance and increase in cathodic current pass from this pore. AC electrodeposition is employed but is not preferred over DC as the later does not yield high single crystalline nanowires [8]. The solution is to selectively remove the barrier at the base. Different combinations of thin films have been employed to achieve this goal, a few are

summarized below for reference:

1- Metal at the base: Yang et al. used a gold layer on top of the Si before aluminum deposition. The anodization of top aluminum oxide after the pore reaches the base, is continued till the barrier thinning results in exposure of the base. This method has however not been characterized, and quality of the CdS deposited within the pores have not been thoroughly studied. Moreover, the authors claim that the thickness of Al is kept small for Si planar techniques. This is not suitable for arrays of nanowires that usually require high aspect ratios [82].

2- Chemical etch:

   O. Rabin et al. used different film combinations Pt coated Si wafer [83]. Anodization thickness is graded along one dimension of the sample. So at anodization completion the area that is exposed longer to the electrolyte experiences decrease in barrier thickness, and an eventual exposure of the underlying Pt base. At this point the sample needs to be removed, as the oxidation reaction with the Pt might break through the delicate PAA. To obtain a more uniform template for electrodeposition Si/Ti/Al, was employed. At the completion of anodization, the sample was electrochemically etched by immersing in a solution of potassium chloride electrolyte, and cathodically polarizing the titanium layer for several minutes. Dissolution o f PAA occurs at pH >8 [84]. This also leads to thinning of the alumina, but gets rid of the alumina barrier layer. Bismuth telluride nanowires were deposited, to confirm depletion of the barrier layer and similar results are expected for Zr, Nb, Hf, Ta [83] films below the as a barrier.

3- Conductive pass:

Yasui et al. employed two different techniques to use the template for electrodeposition [85]. Two types of techniques were employed. Si substrates had W deposited with Al on top, while Mg (001) sustrates were sputtered with Pt, and a thin Ti adhesion layer with Al on top. With the first substrate as anodization reaches completion and the W below the alumina is oxidized, a conductive path is formed, which has some resisitivity when reduced by an annealing process. In the case of the other multifilm structure the pore widening procedure after anodization removes the barrier. CoPt columns were deposited within the alumina of both structures [85].

Multilayer template, deposition of nanowires, and IR absorption using heterostructure nanowires: Crouse et al. employed a multilayer template comprising of a Ti barrier on top of Pt [23]. Anodization leaves a barrier layer that is gradually thinned by ramping up the anodizing voltage. As this process reaches completion the Ti beneath the barrier is oxidized. Voltage ramp is continued and a point the titanium oxide is removed by anodic breakthrough. Template was characterized after anodic breakthrough of the titanium layer for confirmation of the removal of barrier layer, by CV, OER-UV and Tafel plot analysis. This technique is advantageous as it gives a template with Pt at the base that can be used for electrodeposition, on top of a Si substrate that is good for integration of circuitry for device applications. Moreover, this technique can be employed with any desired substrate

4.4 The Original Multilayer Template, Ramp Procedure and Breakthrough

The multilayer thin film stack that is deposited by thermal evaporation on a silicon substrate has been described in earlier works [8,23], and is composed of the following

layers, as shown in the schematic in Fig. 22:

Aluminum: 500nm to 1000nm depending on the length of nanowires required

Titanium: 5nm (8nm in earlier works)

Platinum: 30nm

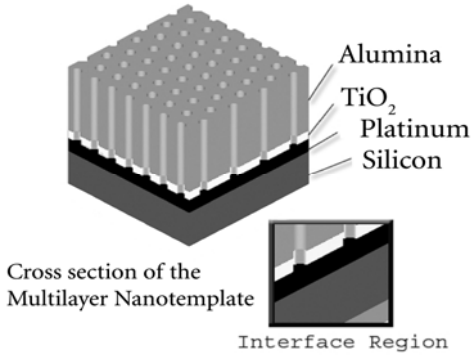

Figure 22: A schematic of the multilayer template after Al anodization, zoom in shows there is no barrier at the pore bases

Each of these layers has their respective roles in the template fabrication process. The initial structure of the multilayer template has been shown to be favorable for some nanowire depositions, and very convenient for nanodot deposition. However, the template fabrication process needs more optimization for it to be scaled up to industrial sized wafer growth for more repetitive results and hence good quality nanowire growth. At the research level it has been challenging to get a good nanowire growth within the pores, with uniform distribution. This chapter will study the process improvement over the conventional template fabrication procedure described in [23].

As seen earlier, the nanotemplate breakthrough is achieved by anodizing the aluminum layer to completion, and subsequent ramp of the voltage to incrementally etch away the

alumina barrier at the pore base, oxidation of the titanium layer underneath, and subsequent removal of the titanium oxide by modified anodic breakdown [81]. The ramping process although very convenient, as discussed in earlier works, has to be improved for a good quality starting nanoporous template for electrodeposition of materials. The two issues encountered towards this end, are that breakthrough has to be widespread throughout the sample, and that the pore bases are open so that after removal of the titanium oxide the platinum is not covered by alumina barrier. In earlier works, for example Crouse et al. [23] breakthrough was characterized by several techniques, namely, CV, OER-UV and Tafel plot analysis, to confirm that these issues were resolved, i.e. the pore base was clean and the platinum was exposed. These techniques although provide scientific evidence of the result, however require a separate experimental setup. It would be useful to incorporate a procedure within the anodization, so that breakthrough may be monitored as it is taking place. This is a good idea as it is essential to stop the breakthrough procedure as soon as it happens, to avoid damage to the sample, due to very high current flow through the pores, and to confirm it as it has happened, simultaneously.

The typical anodization curve for aluminum is shown, in Fig. 8, with current as breakthrough is achieved, by a modified anodic breakdown of the titanium oxide at elevated voltage [86]. .

As the current increases it is evident that the titanium oxide is being removed, and the current path does not have an oxide that inhibits current but a conductor. As the breakthrough is completed we would expect a current to essentially follow a voltage applied proportionally.

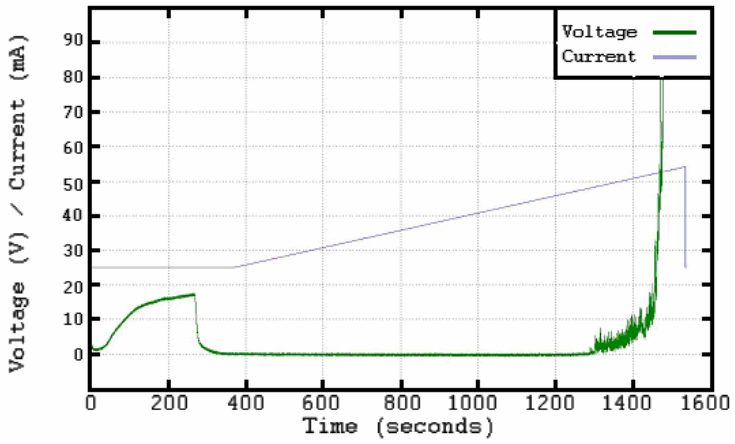

Figure 23: Anodization Curve for The original Multilayer Template. Green Curve shows current in mA, Blue curve shows voltage ramp after anodization is completed. Breakthrough is prominent at around 1300 secs, where current suddenly increases by 50 orders of magnitude

This hypothesis is based on the fact that we have a metal at the pore base, and hence a roughly resistive circuit. An SEM of the template base after ramping up and template removal by a chemical etch, is given in Fig. 9. CdS nanowires were deposited in the template as a proof for great utility of the template structure [8].

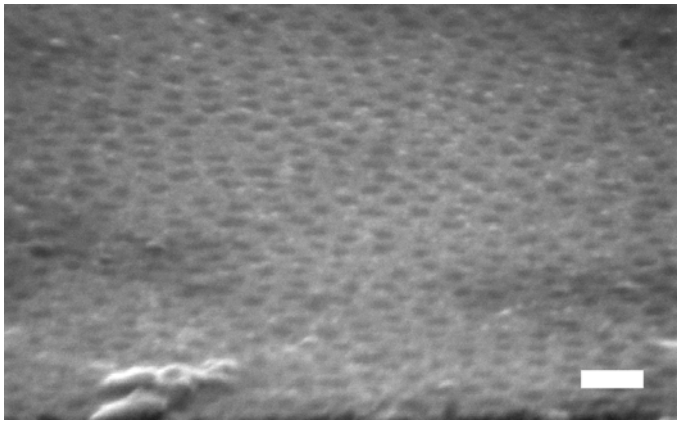

Figure 24: Template after anodization, breakthrough and subsequent chemical etch that removed the alumina. The SEM shows that the Titanium beneath the anodized aluminum has been oxidized and removed leaving the Platinum beneath it exposed. The bar is 100nm in length.

4.5 Optimization of The Multilayer Template and Breakthrough Procedures

This section describes the optimization process of the breakthrough mechanism for good nanoporous template with open bases. A modified breakthrough procedure was initially employed. As results indicated, a gentler breakthrough procedure was required, so the starting material was revised to achieve this goal. Eventually, a good combination of starting material and post anodization procedure resulted in an excellent starting material for subsequent electrodeposition.

4.5.1 Modified Ramp, Diagnostic Current, and Breakthrough

This idea can be used to replace the post anodization ramp by a cyclical ramp, with two different cycles. One cycle will be the ramp procedure, as before, that will achieve breakthrough gradually, and the second cycle will in alternate succession monitor current as a positive sinusoid is applied. The anodization current and voltage waveforms,

implementing this modification are shown in Figure 25.These two cycles will be repeated until the diagnostic sinusoid voltage produces a sinusoid current waveform, confirming oxide removal, hence a current proportional to the voltage, defining a resistive circuit. This idea, though promising initially, will be improved upon later.

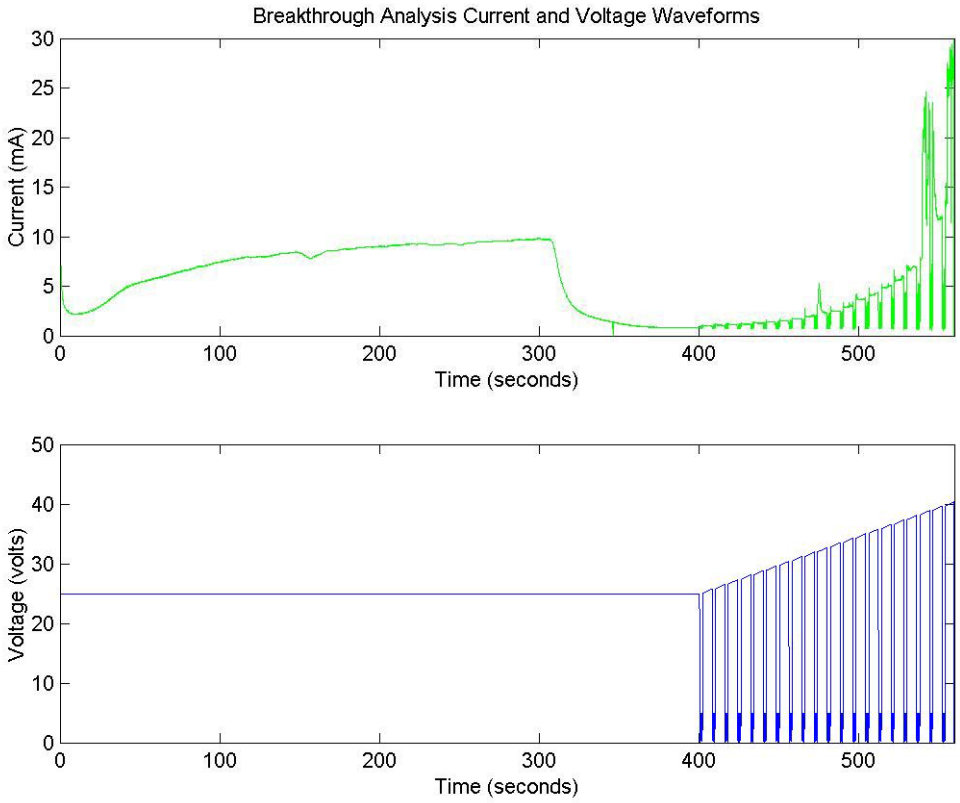

Figure 25: Anodization and Modified Post anodization procedure, that consists of a ramp cycle, and a 5V sinusoid cycle

It will be interesting to compare the current with respect to applied sinusoid diagnostic voltage to see how much current the sample is allowing to pass through the oxide. The initial and final waveforms are shown in Figure 26. It can be seen that over the course of the the ramping procedure, that the amplitude of the current as well as the shape of the

waveform have improved. Towards the end of the ramp, a diagnostic voltage of 5V peak, results in a current of less than 0.8mA. As the ramp progresses, and there the oxide breaks through, we see, a final value of around 6mA at the same applied voltage of 5V peak, as shown in Figure 26. The initial waveform does not depend on the applied voltage, a characteristic expected from an insulating material. As the ramp progresses and we expose Pt at the base, the applied voltage produces a current that exhibits a nice sinusoid waveform.

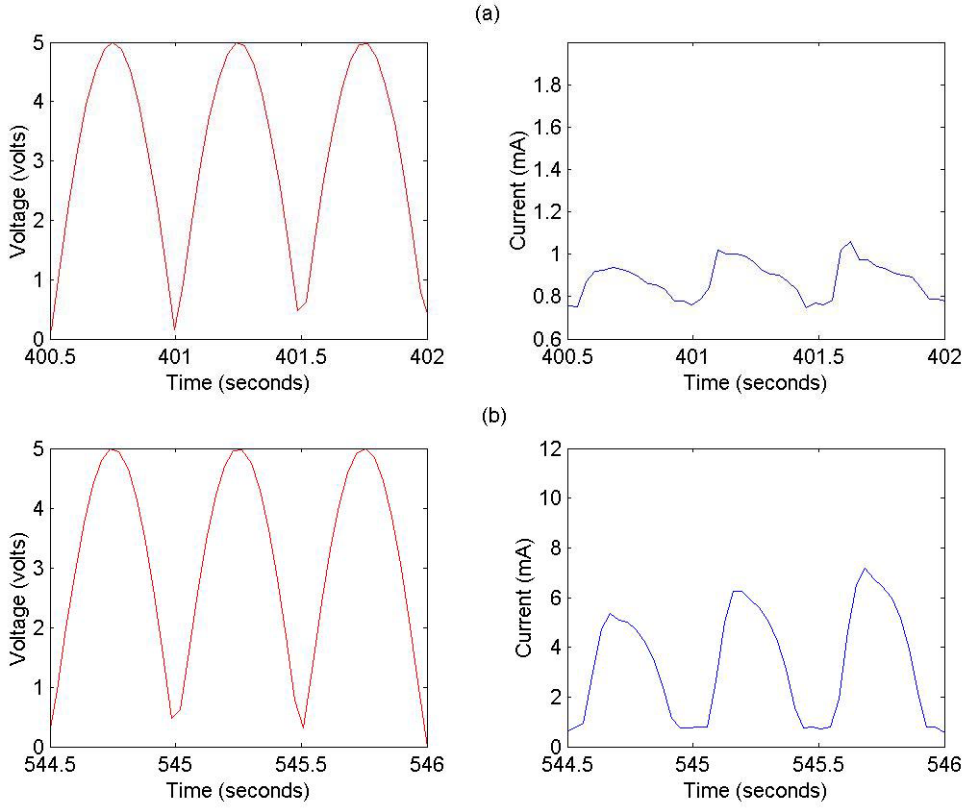

Figure 26: Initial and final current waveforms, during the diagnostic sinusoid cycle of the ramp procedure. Earlier on, 5V produces around 1mA max, which is significantly increased as breakthrough progresses, and a max of 6mA is achieved.

As we clean the pore bases the diagnostic current will increase. However, at one point we have to stop applying the ramp any further, in order to avoid sample degradation. As seen in Figure 25, towards the end we see spikes in current with steady increase in amplitude. This is the point where, the amount of current will start degrading the sample, if conditions are not changed. Beyond this point we see delamination of the sample that is shown by an increase in current amplitude, several orders of magnitude, and is shown in Figure 27 as white spots.

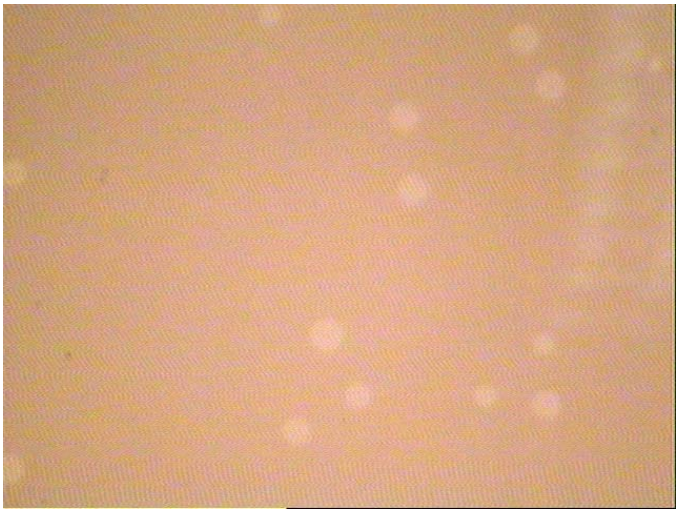

Figure 27: Image of sample surface depicting delamination sites seen as white spots.

The amount of current flowing through the sample and the delamination can severely damage the sample as is described later. The resulting template may not be good for electrodeposition, because the delaminated areas may be areas where the platinum has no oxide on it and would cause preferential electrochemical growth at these locations. Therefore, the favorable scenario would be to achieve breakthrough and stop further ramping as early as possible so that the very high amount of current flow that follows is stopped before causing damage to the sample. This may be achieved if we have

breakthrough at gentler conditions i.e. lower voltages. The breakthrough voltage depends on the titanium thickness; therefore thinning of the barrier layer will reduce the breakthrough voltage. Thinning the layer too much may cause intermetallic formation and Al diffusion may occur in the Pt layer [87-88]. Two obvious ways are either to have a starting thickness that is lower, or to reduce the thickness by annealing, which would produce intermixing at the titanium/aluminum interface, effectively reducing the titanium thickness. After having studied the phase diagrams for the metals Al/Ti., and Ti/Pt, [89], it was decided to run a set of samples at 325 °C for different periods of time. Following this procedure, the samples would be anodized to compare the breakthrough voltages keeping other experimental parameters, i.e. temperature, type of electrochemical solution, anodization voltage and ramp duration constant.

4.5.2 Gentle conditions for breakthrough

Two approaches were used to achieve gentler conditions for breakthrough, annealing to effectively reduce the titanium barrier thickness. Results with respect to this approach and problems that arose during the procedure are mentioned next. Following this results with respect to a template with a lower starting thickness of titanium and are given with a discussion of the results.

4.5.2.1 Annealing, Intermetallics formation and Adhesion Issues

As explained earlier, the main indicator of titanium oxide removal at the pore base is a significantly higher current flow. The ramping procedure requires that the sample is subjected to a large voltage for a prolonged period of time as the titanium layer reaches breakthrough. The breakthrough is based on avalanche breakdown of the titanium oxide, hence can be considered a relatively sudden phenomenon, i.e. within a few seconds there

is a large current flowing through the solution into the pores. This large current is seen to increase bubble formation at the surface of the template, resulting from the oxidation evolution reaction at the pore bases where the Pt is. This reaction will destroy the aluminum film if there is no adhesion promoting layer (Al/Pt only) [83], or cause large caves within the nanopores towards the pore base, again due to the same reason. In other cases, the sample will have large areas where the top most alumina template layer has come off, i.e. delamination., seen as white spots in low resolution microscope of the sample, as seen previously in Figure 27. As the titanium thickness determines the voltage at which breakthrough is likely to occur, one way to solve this problem would be to decrease the deposited titanium thickness. There are two major issues with the practicality of this approach. The first one is to get a sufficient decrease in breakthrough voltage, we have to go to a range of 5 nm or less of Ti thickness. At these scales, it is very challenging to get an exact value of Ti deposition thickness, in case different systems are used. It is therefore customary to see variations in breakthrough voltages as calibration of deposition equipment results in fluctuations in measurements of thicknesses in the angstrom regime (in case of thermal evaporation of the metals on the Si wafer). The second issue is as we go to smaller titanium thicknesses, the effectivity of the barrier layer decreases. In fact, very similar anodization behavior is observed for a barrier layer of of 2nm Ti, and no barrier layer at all, wherein samples cannot be anodized to completion. Three thicknesses were chosen for the study, 2nm, 4nm, and 6nm. Using too small a thickness of Ti (lower or equal to 2nm), does not give favorable results, as there is significant intermetallic formation at the Al/Ti, and Ti/Pt interfaces even at room temperatures. This disrupts the anodization of aluminum prematurely, and the 2nm or

lower barrier Ti samples will exhibit the same pattern in current profile as Al/Pt with no barrier. This can be seen in Figure 28.

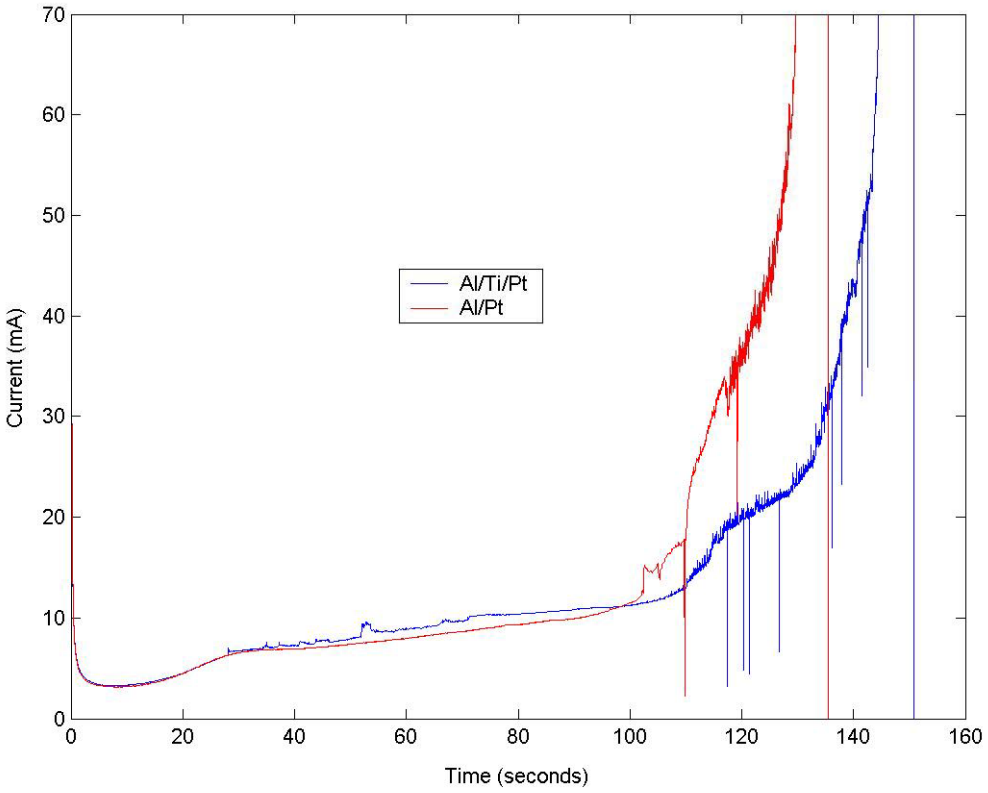

Figure 28: Anodization curves for Al/Pt and Al/Ti/Pt samples. Blue curve depicts current for Al/Ti(2nm)/Pt sample, while the red curve shows Al/Pt with no barrier layer. It can be seen that the current waveforms exhibit a similar patterm, except a longer shoulder with the sample with a barrier layer.

The 4nm samples exhibited a nice breakthrough voltage, did show current spikes. The reason was that, prior to anodization the samples were being painted by a conducting silver paste all around the back and on the sides to get the voltage to be applied to the surface directly. During anodization this procedure did not exhibit a repeatable pattern,

for different sample runs. It was decided to use a different cleaning procedure and to apply the conducting silver paste at the back only. This would allow for the potential drop to be uniformly distributed across the sample and at the same time, the surface would be an equipotential surface, nevertheless. Concurrent to this set of experiments, a study of breakthrough vs. annealing was carried out for the 4nm and 6nm Ti thickness samples. Alternate to the reduced initial thickness of Ti, the other option was to start off with a large Ti layer and anneal which in turn causes intermixing to effectively reduce the barrier layer as mentioned above. Towards this end, two sets of samples were prepared one with 4nm thickness, and one with 6nm thickness, to compare with the 5nm thickness sample that we had been using initially. It was very difficult to get breakthrough at a reasonable (less than 65V) voltage for 6nm Ti barrier layer sample if no annealing was carried out. As the exposure of the sample to annealing was increased there was an almost linear decrease in breakthrough voltage, indicating the effective Ti barrier layer has decreased. The samples exhibited very smooth anodization curves, and decrease in the breakthrough voltage, however, significant degradation of the sample was seen after anodization.

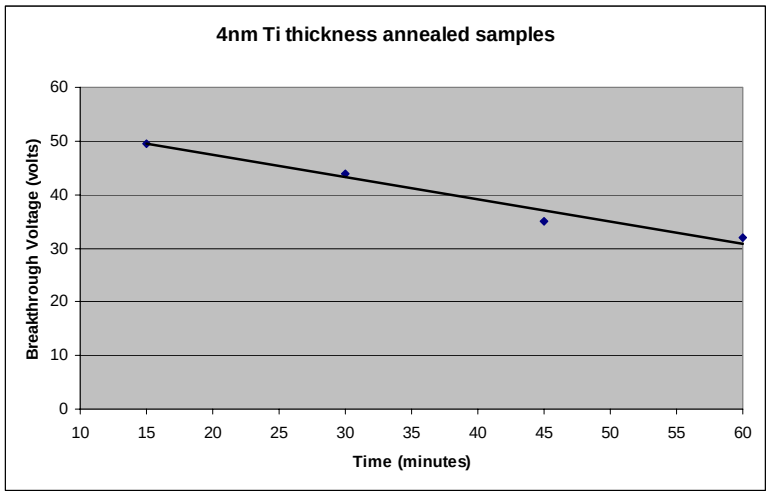

Figure 29: Breakthrough voltage versus annealing times for one set of samples with Ti thickness of 4 nm

The breakthrough voltage decreases in a linear fashion with respect to annealing time for the 4nm and 6nm titanium thicknesses as seen in Figure 29 and Figure 30. Initial inspection on low resolution microscope showed a uniform density of black spots on the surface of the annealed samples.

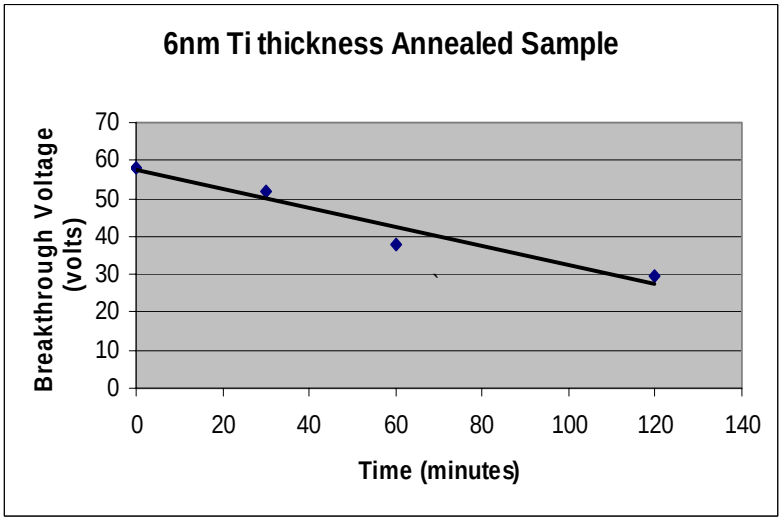

Figure 30: Breakthrough voltage versus annealing times for one set of samples with Ti thickness of 6 nm

SEM inspection of the annealed sample depicted that the annealed samples show hillock formation of the Pt layer in the aluminum. This behavior has been observed in literature too [90].

Figure 31: Annealed sample surface showing black spots that may correspond to the hillocks

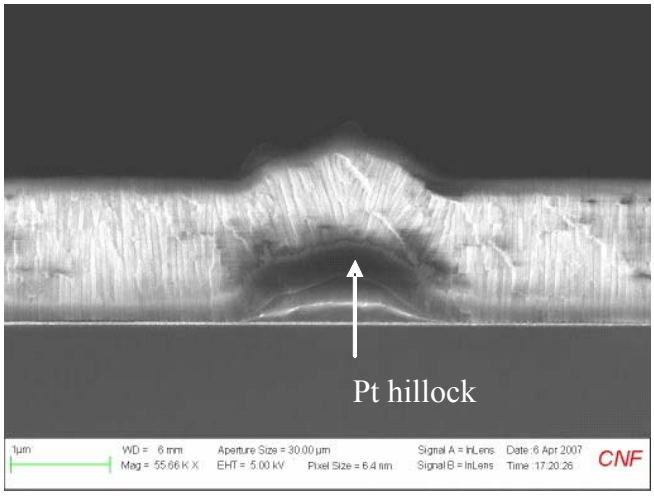

Figure 32: SEM of anodization template with 4.0nm upper titanium layer, annealed at 325°C exhibits platinum hillocks beneath alumina surface

This ruled out the possibility of using annealing for improving adhesion and improving breakthrough conditions. As mentioned earlier, another problem that had been observed with the 4nm was an unexpected spike during ramp. The samples that had been showing some spikes did show some signs of delamination and a current spike during post anodization ramp. This seemed to indicate that adhesion was one of the underlying reasons and that annealing could not be used to improve adhesion. In addition to this concern, initial cross sections of the 4nm Ti barrier samples showed a residual alumina barrier at the pores bases, even after breakthrough of the underlying titanium oxide. If we closely inspect the SEM shown in Figure 33, it is evident that that the alumina that remains there is thickest near the pore wall and thinner near the pore center, suggesting that there may be a current/ion exchange path through this layer of alumina to the titanium dioxide layer beneath. This would allow for the titanium dioxide layer to have broken down, in presence of the alumina. These samples, when observed under a microscope usually displayed some evidence of pinholes uniformly distributed across the alumina surface, indicating that small areas of delamination were occurring across the sample surface.

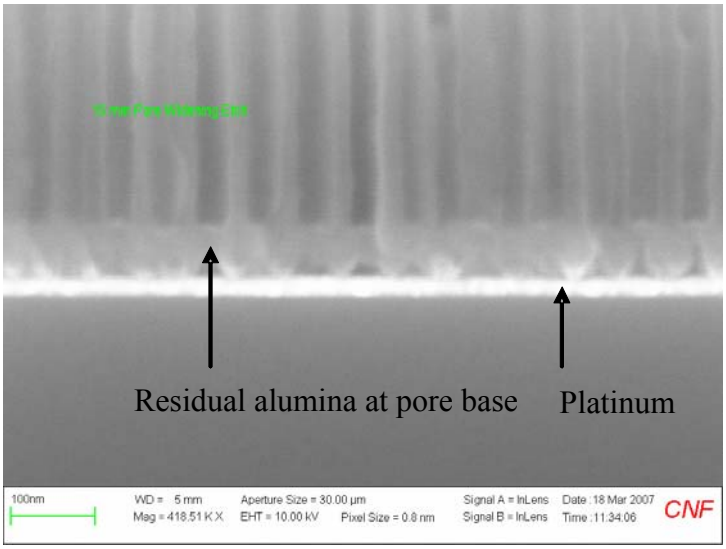

Figure 33: Anodized template using voltage ramp procedure to achieve titanium oxide breakthrough. Residual alumina still present at pore bases.

It was decided that we need to carry out thermal evaporation of different types of starting wafers with variable titanium thicknesses, and to improve adhesion by adding another layer between the Pt and the Si. This modification would give some insight on solving the adhesion problem, as well as comparing the voltage drop the oxide layers and resistance of the wafer, for good anodization curves.

4.5.2.2 Titanium Thickness Variation

A set of nine wafers was prepared including a combination of 2.5 nm, 3.0 nm and 3.5 nm with three different types of wafers, i.e. n-type wafer with a BOE clean of the oxide, p-type with a pirhana clean, and p-type with a BOE clean. At this point, another major revision was made, in the post anodization breakthrough procedure. Instead of employing a ramp after completion of anodization, a lower amplitude pulsed voltage was tried. This ensured that the sample is not subjected to a harsh condition for achieving

breakthrough, and that the process will be gentle, and more sustained.

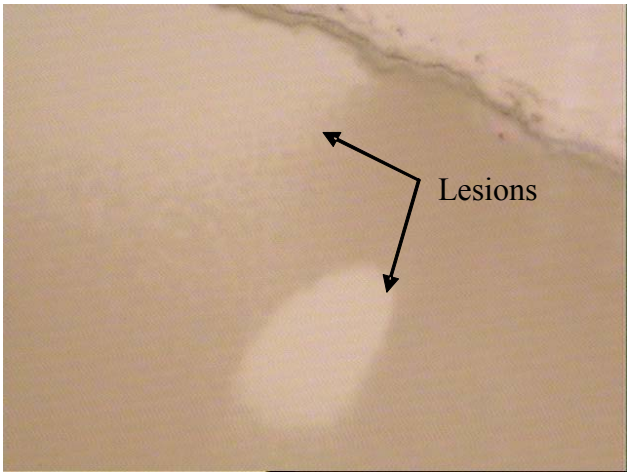

Figure 19: Anodized template surface with 2.5 nm upper Ti layer. Arrows show delamination lesions, within anodized alumina

The on pulse would apply a large voltage across the barrier at the base, followed by an off period where the system is allowed to gain its equilibrium state, and solution replenishes the pores, with ions. The results indicated success of the technique, in achieving breakthrough as well as getting rid of the alumina barrier at the pore bases. The pirhana cleaning procedure to the starting wafers showed the best results in terms of repeatability for 3.0nm and 3.5nm wafers. Although good current profiles that show leveling off were obtained for the BOE cleaned wafers, it was not possible to get repeatable results for wafers. Figure 19 shows a post-anodization photograph of a wafer with a 2.5nm titanium layer. Large circular and strip-like delamination lesions are observed around the perimeter of the anodized area (For reference, everything below and to the left of the dark strip running across the top right of the frame is anodized material and the light-colored lesions lie within this area.). Figure 35, however, shows a similar

photo of a 3.0nm titanium sample, which exhibits no such delamination. Hence, it is obvious that 3.0nm titanium thickness is necessary to maintain acceptable adhesion properties and also achieving breakthrough of the titanium dioxide layer. The next section goes over the current leveling off seen in current profiles of samples, in detail

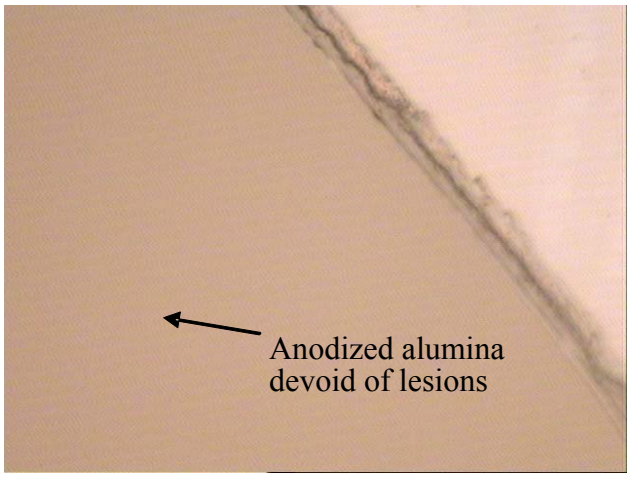

Figure 35: Anodized nanotemplate with 3.0 nm upper titanium layer. No delamination lesions observed in anodized alumina.

4.5.3 Leveling Off of Post Anodization Current and Results

It has been observed during anodization that the current, as titanium oxide is broken through, will start increasing significantly, and as more areas of the sample see breakthrough this current will keep increasing, exponentially. As this technique risks of damaging the alumina layer, it was decided to achieve breakthrough by a different technique: applying short pulses of voltage. We expect that breakthrough will be incrementally achieved, and there will be a point where the current will reach steady state, as there is no more barrier layer or oxide layer. Initially, results indicated this behavior for three voltage values, i.e.15V post anodization stepped voltages, 12.5V and

10 V. The current profiles are shown in Fig. 36. Despite the promising current profile, on inspection of the surface, all of these samples exhibited some white spots, indicating some sample degradation. As a starting point for the oxide removal at the base, this procedure indicated good potential. For a thickness of 3.0 nm, the results indicated good repeatability, and a thin barrier layer at the base, that could be removed easily by a chemical etch, after the anodization and post anodization pulse voltage procedure.

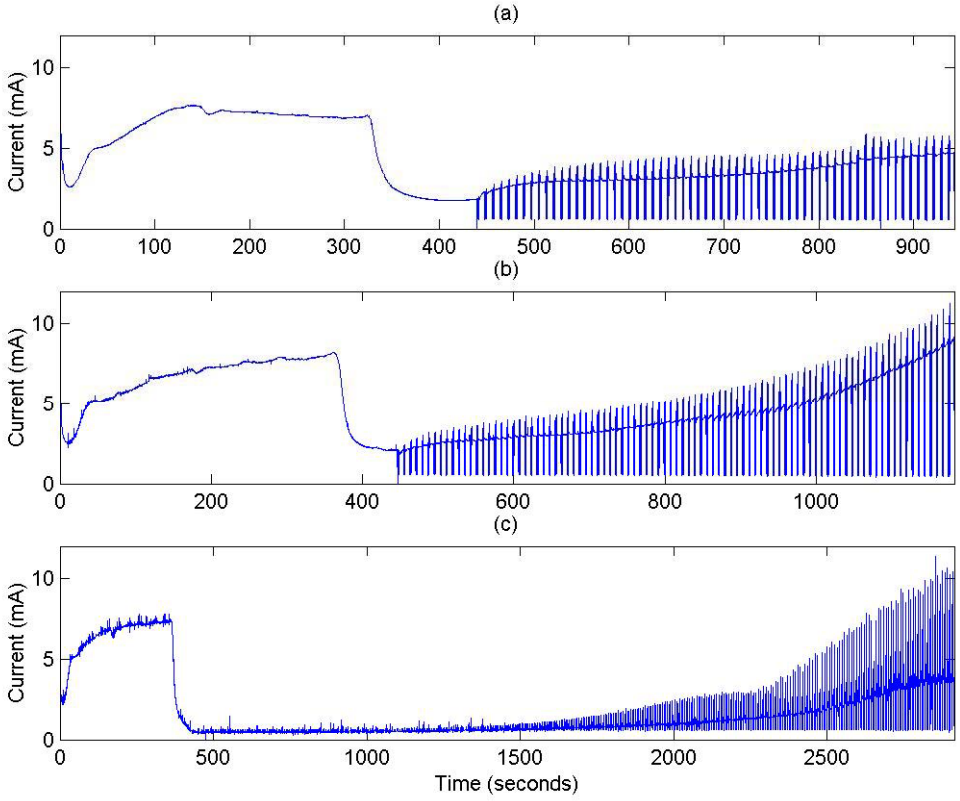

Figure 36: Initial results for Levelling off of three different set of samples for (a) 10V pulses, (b) 12.5V pulses, (c) 15V pulses, with an alternate 5V sinusoid cycle. All three samples exhibit leveling off, however 12.5V and 15V pulse voltages also show an exponential increase after leveling off shoulder.

An explanation of the procedure follows. As we apply a post anodization procedure, and incrementally remove the alumina barrier, and/or breakthrough the titanium, we expect an increase in current, as the platinum becomes exposed. As we progress through the breakthrough throughout the sample area, we expect this current to increase, and eventually approach or reach a steady state value. This happens as we have exposed most of the platinum at the base. At this point, the oxygen evolution reaction will begin at these sites. Further subjecting the sample to the same conditions will only deteriorate the sample as pores will start becoming wider (as sulfuric acid etches alumina at a concentration of 0.5M) and this will become the dominant reaction as the oxide starts getting slowly etched away along the pore walls, as seen in curve (b) after 1000 seconds, and curve (c) after 2500 seconds in Figure 36. Further degradation sites start emerging with possible reason being the oxidation evolution at the pore bases that may cause delamination areas with no alumina. As this back and forth reaction occurs, that may further increase the current, and further increase the pore size at these sites, until these sites dominate the current passage, and other reactions are suppressed. Therefore, we need to try to get breakthrough at as gentle conditions as possible, in order to remove the barrier layer, and stop the procedure immediately.

This hypothesis was confirmed by the results we got with the piranha cleaned 3.0 nm p-type wafers, and the 3.5 nm wafers with slightly different results, in terms of current amplitudes, but similar in behavior or current waveform. In these waveforms the leveling off is smoother, and the steady state has a smaller slope.

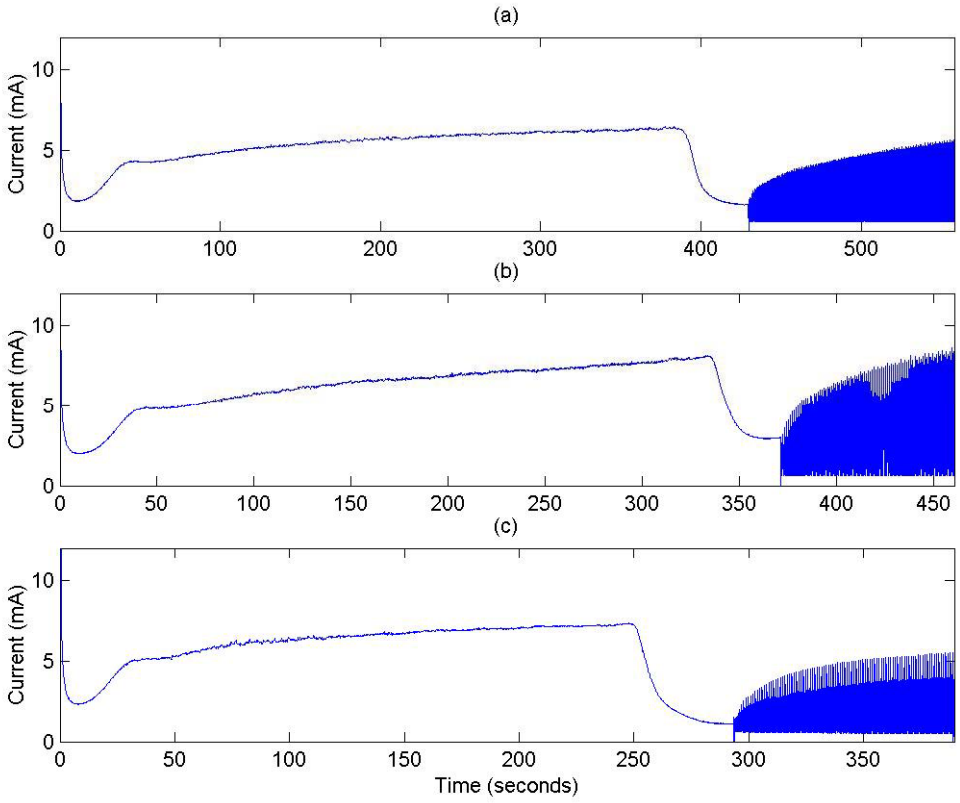

Figure 37: Leveling off of current waveforms, after anodization at 26V. We can see all three curves depict the same behavior with respect to the slope indicating that breakthrough has been reached, at (a) 5V pulses, (b) 7.5V pulses, and (c) 10V pulses.

We expect similar results with n-type piranha-etched silicon wafers, with 3.0nm upper titanium layer. For this series of experiments, the best results were obtained using voltage pulses of 5-10 V every two seconds, with the pulses of 150 ms duration. This provides the time for the solution to relax back to equilibrium during the off -second period. Under these conditions, the current increases steadily, but eventually begins to level off, which is an indication that we have reached a steady state consistent with breakthrough down to the platinum at the base of the pores. On comparison with platinum-only control samples,

the post breakthrough current levels correspond to a 5-10% porosity of the alumina template. The samples show no indication of delamination or pinholes. Figure 37 shows a typical current profile for the samples described immediately above, using (a) 5.0V pulses, (b) 7.5V pulses, and (c) 10V pulses, to break through the titanium layer following aluminum anodization.

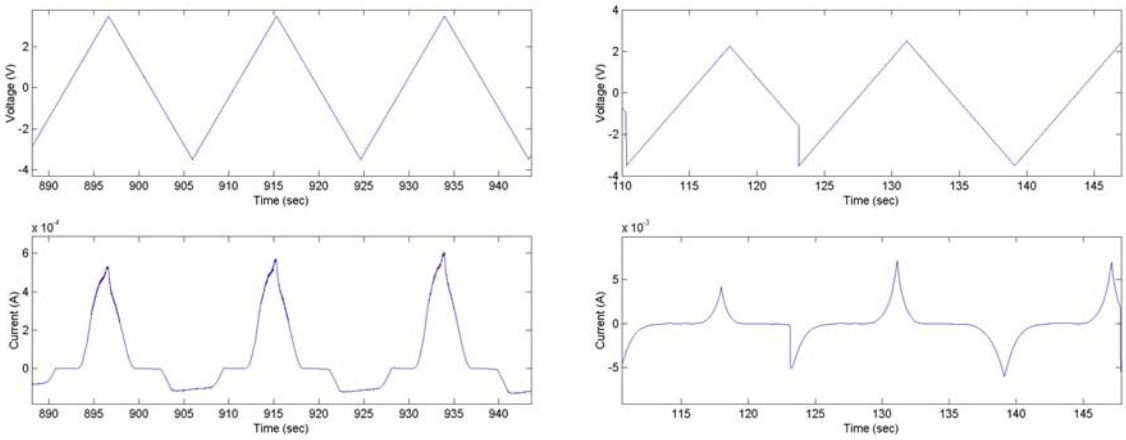

Figure 38: Left: Pre breakthrough voltage sweep, there is very low current in the negative voltage regime, and about 0.4mA at 2.5V in the positive voltage. Right: Post breakthrough voltage sweep, current is about 5mA at 2.5V, about ten orders of magnitude larger than pre breakthrough. Symmetry shows that both oxidation and reduction at occurring in the positive and negative voltage regimes respectively.

Figures 38 and 39 show the voltage and current sweeps, before and after breakthrough of the titanium oxide layer. In Figure 38 a triangular voltage waveform between 2.5V and -2,5V, starts off with 0.4mA peak in the positive regime, and towards the end the amplitude reaches a current of around 5mA peak value. In Figure 39, a comparison of the voltage sweep is given, of the multilayer template after breakthrough and a platinum only

on silicon control sample.

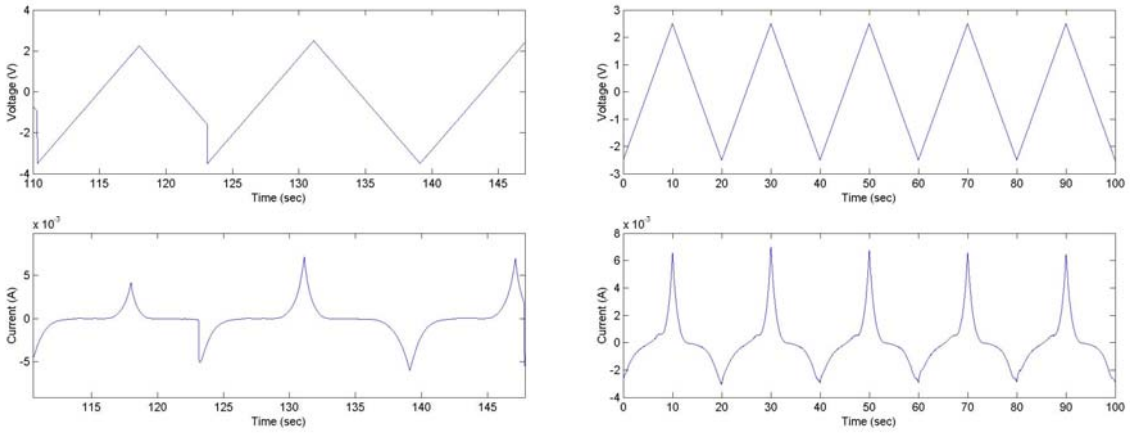

Figure 39: Left: Current profile for the multilayer template after breakthrough of the TiO_2 layer. Right: Platinum on Silicon Substrate. The current profiles increase and decrease symmetrically in both, but the shapes are very similar in case of the platinum and the multilayer that has platinum at the base.

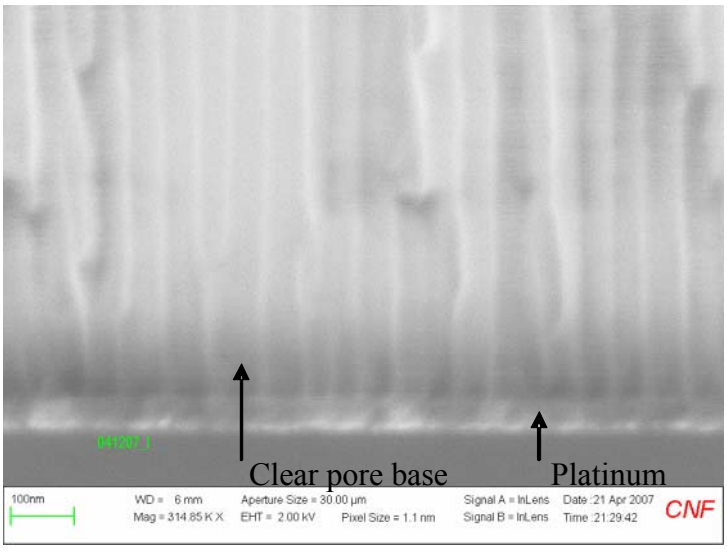

Figure 40: Anodized alumina nanotemplate showing no residual alumina at base of pores

An SEM of the pore cross section after this procedure indicates successful removal of the

alumina barrier layer at the pore base, and a straight pore reaching to the bottom of the template. This is seen in Figure 40. At this point, we have confirmed that the alumina barrier no longer exists at the pore bases. However, in order to ensure uniform breakthrough of the titanium oxide layer, we have to apply a number of voltage spikes, that will uniformly remove the oxide, and expose the platinum at the pore base. Figure 41 shows a voltage sinusoid applied to the template after the alumina barrier clean.

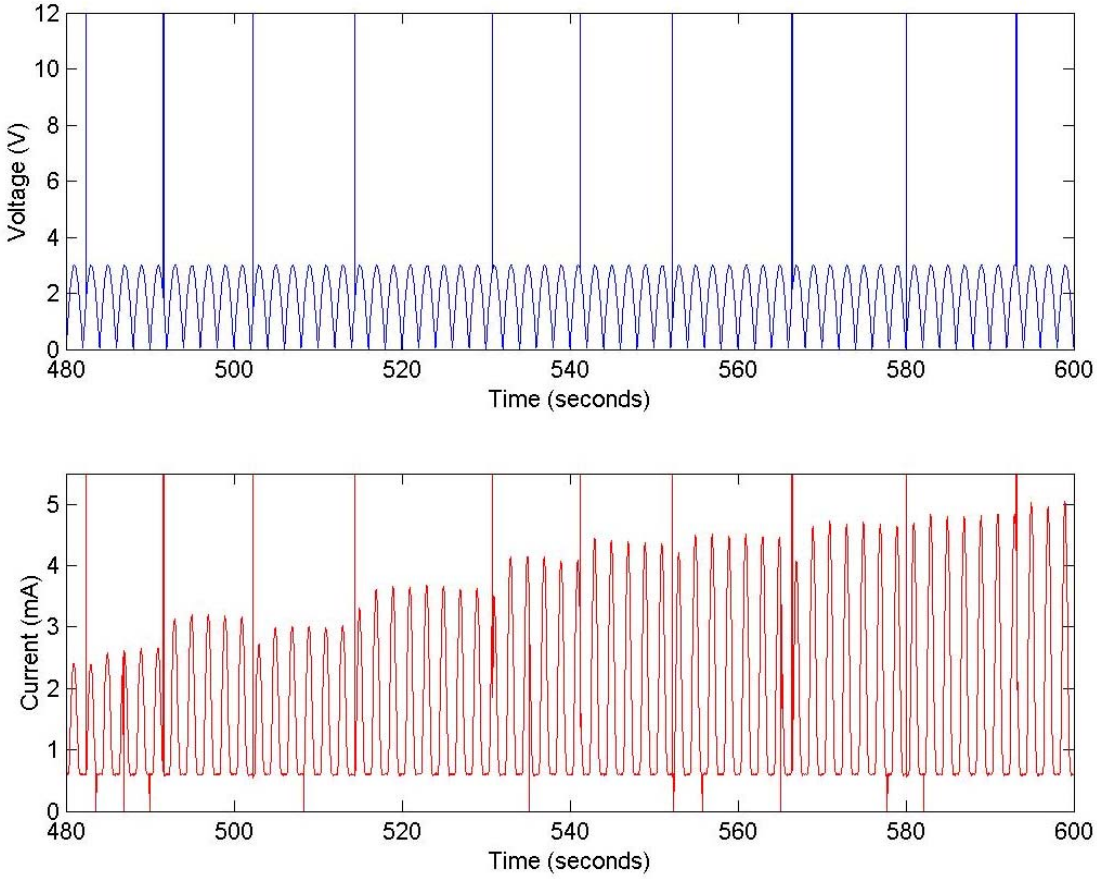

Figure 41: Post breakthrough pulse procedure to ensure uniform and complete breakthrough all over sample area. The pulses are 45V in amplitude and 0.15 sec in duration. After a number of pulses the current almost doubles from 2.5mA to 5mA.

As can be seen before application of the voltage spikes, a voltage sinusoid of amplitude 2.5V produces 2.5 mA. As the platinum is exposed with consistent application of voltage spikes of 45V amplitude, the current reaches a steady peak of around 4.5 mA. This completes the optimization of the alumina template, and quantum wires and quantum dots of different materials can be electrochemically deposited within this template.

Summary

We have optimized the complete multilayer template by employing a variety of techniques, as well as the anodization procedure, and the post anodization procedure, to get a very good breakthrough uniformly. We have addressed the critical issues of pore regularity, sample integrity and adhesion of individual layers within the template. In addition to the quality of the starting material, we have also achieved excellent breakthrough with very repeatable results. This is supported by the SEM images of the cross section of the template that show pore termination at the platinum base, with good uniformity, pore diameter, and pore regularity. This starting template will have good use for electrodeposition within the pores, as will be seen in the following chapter.

Chapter 5: Electrodeposition of CdTe Quantum Dots and Quantum Wires and Characterization results

5.1 Electrochemical Deposition Background

Electrochemistry involves chemical phenomena associated with charge separation, which often leads to charge transfer. It can occur homogeneously in solution, or heterogeneously on electrode surfaces. To assure, charge electro neutrality, two or more charge transfer half reactions take place, in opposing directions. Except in the case of homogeneous redox (reduction-oxidation reactions), these are separated in space, usually occurring at different electrodes immersed in solution in a cell. For charge transport to occur, these electrodes are linked by conducting paths both in solution (via ionic transport) and externally (via electric wires etc.). When the sum of the free energy changes at both electrodes is negative energy released can be collected by batteries. On the other hand, if it is positive, external energy can be supplied to electrodes to allow reactions to take place and convert chemical substances (electrolysis).

Electrode reactions are heterogeneous and take place in the interfacial region between

electrode and solution. This is the region where charge distribution differs from that of the bulk phases. At each electrode, charge separation can be represented by a capacitance and a resistance. The electrode can act as a source (for reduction) or a sink (for oxidation) of electrons transferred to or from speices in the solution [91]

$$O + ne^- \longrightarrow R \quad (1)$$

Here O and R are the oxidized and reduced species, respectively. The electrode can also participate in the reaction as in dissolution of a metal M [91]

$$M \longrightarrow M^{n+} + ne^- \quad (2)$$

In order for electron transfer to occur, there must be a correspondence between energies of the electron orbital where transfer takes place in the donor and acceptor. In the electrode this level is the highest filled orbital, which in a metal is the Fermi energy level E_f. In soluble species it is the orbital of the valence electron to be given or received.

Electrode reactions are half reactions and by convention expressed as reductions. Each has associated with its standard electrode potential, $E^{Ø}$, measured relatively to the normal hydrogen electrode (NHE) with all species at unity activity (a_i). For half reactions at equilibrium, the potential, E, can be related to the standard electrode potential through the *Nernst equation* [91].

$$E = E^{\phi} - \frac{RT}{nF} \sum v_i \ln a_i \quad (3)$$

Where v_i are the stochiometric numbers, positive for products (reduced species) and negative for reagents (oxidized species). This tendency of the reduction to occur is given by

$$\Delta G^{\phi} = -nFE^{\phi} \quad (4)$$

These equations will be reviewed again, in context of the deposition of CdS nanowires.

Two types of cells exist, i.e. galvanic and electrolytic cells. A galvanic cell is one in which a chemical reaction is transformed into electrical energy. In an electrolytic cell, electrical energy is converted into chemical energy, by an external voltage source. At the anode in a galvanic cell, since the oxidation is spontaneous, there is an excess of electrons at the electrode. In an electrolytic cell, where the oxidation is forced to occur, there is a shortage of electrons and a positive charge.

	Anode	Cathode
Galvanic Cell	-	+
Electrolytic Cell	+	_

Solvated ions move at different velocities, according to their size and charge. Diffusion is due to a concentration gradient and migration due to electric field effects. In other words, diffusion may occur for all species, while migration affects only charged species.

Diffusion is described by Fick's first law [91]:

$$J_i = -D_i \frac{\partial c_i}{\partial x} \tag{3}$$

Where J_i is the flux of species i of concentration c_i in direction x, and is the concentration gradient. D_i is the proportionality factor between flux and concentration gradient, known as the diffusion coefficient. In the presence of an applied electric field [1]:

$$E = \frac{\partial \phi}{\partial x} \tag{4}$$

$$J_i = -D_i \frac{\partial c_i}{\partial x} - z_i c_i \frac{F}{RT} E \tag{5}$$

Here the second term on the right hand side represents migration. The electric force on the right hand side is opposed by three retarding forces, namely, a frictional force that depends on the size of the solvated ion, an asymmetric effect, and a tendency for greater salvation in front of the ion compared to the direction behind it. In addition there is an electrophoretic effect that is defined as the ion movement stimulated motion of solvent molecules associated with ions of the opposite sign, resulting in a net flux of solvent molecules in the direction contrary of that of the ion considered. Let us describe the region where the electrode kinetics take place, called the interfacial region. The thermodynamic driving force and how the reactions take place depend on the structure of the interfacial region. This region is known as the *electrolyte double layer region* and the interfacial region in the solid is known as the *space-charge region*. The later region is very thin in metals. A schematic of the electrode solution interface is given in Figure 42.

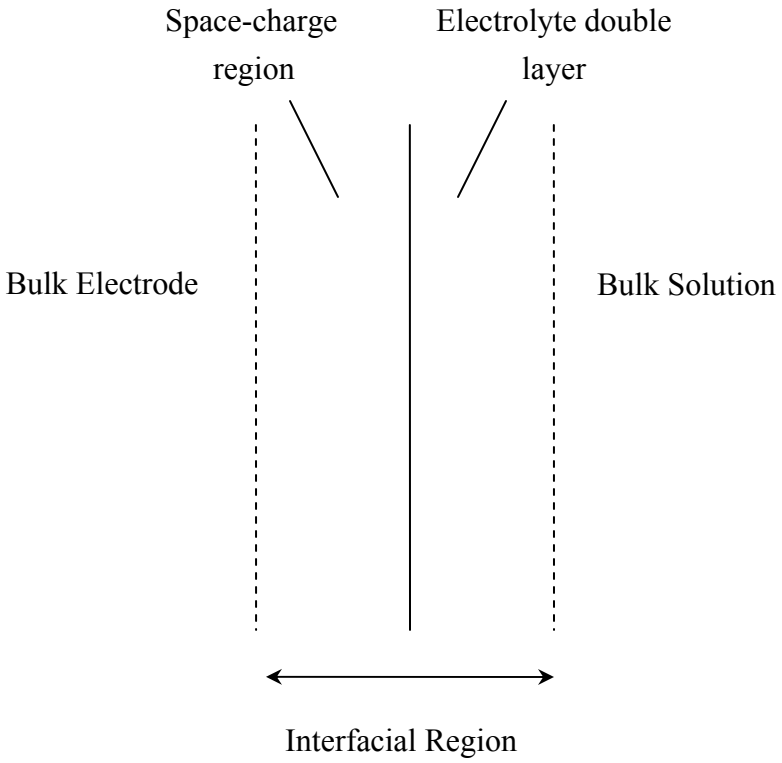

Figure 42: Schematic illustration of the electrode-solution interface [91]

The interfacial region in solution is the region where the bulk value of the electrostatic potential, ϕ, differs from that in the bulk solution. The basic concept is of an ordering of positive or negative charges at the electrode surface and ordering of the opposite charge and in equal quantity in solution to neutralize the electrode charge. The function of the electrode is only to supply or remove electrons from the interface. More sophisticated models exist, such as Helmholtz model, Gouy Chapman model, etc. [91].

In an aqueous solution, the electric double layer can be understood as follows. The inner layer, i.e. space charge region, is a monomolecular layer of adsorbed water molecules and ions, and an outer diffuse region that compensates for any local charge unbalance. This

gradually merges into the bulk solution. In case, of a metal immersed in pure water, the electron fluid within the metal causes the polar water molecules to adsorb to the surface and orient themselves so as to create two thin planes of positive and negative charge. If the water contains dissolved ions, some of the larger (and more polarizable) anions will loosely bond to the metal, creating a negative inner layer which is compensated by an excess of cations in the outer layer.

Electrochemistry is the study of reactions in which charged particles (ions or electrons) cross the interface between two phases of matter, typically a metallic phase (the electrode) and a conductive solution, or electrolyte. This process or chemical reaction takes place within the double layer and produces a slight unbalance in the electric charges of the electrode and the solution. The potential differences essentially dictate the thermodynamics and kinetics of the reactions that take place.

When semiconductors are formed on a surface of the electrode, they do not constitute the shape of a perfect single crystal, but a collection of crystals side by side with random orientations, known as grains. Two major modes of grain evolution exist in electrodeposition, namely nucleation and growth. Nucleation describes how often a random arrangement of incoming atoms will spontaneously order itself into a crystal. Growth is the term that describes how quickly these nucleated regions spread outwards. Ideally, we want one nucleation site for thin film growth, and many nucleation sites for nanowires. The following section describes the electrode kinetics, transport effects and crystal growth in more detail.

5.2 Reaction Dynamics

To grasp the electrodeposition process better, it is important to understand the following three mechanisms of the process: electrode kinetics, transport of species in the pore, and crystal growth. As the process is described further, it will become evident why DC electrodeposition is preferred and why it is carried out at galvanostatically (constant current) rather than potentiostatically.

Let us start with some basic terminology. Nernst equation states that the potential of an electrode through which current flows differs from the equililbrium potential by an amount [92]:

$$\varepsilon^0_{electrode} = E^0_{std} + RT\sum_j z_j \ln a^0_j \qquad (6)$$

where *zj* is the stoichiometric coefficient (ratio of species with respect to each other for a binary compound, a one to one ratio is ideally expected, hence a stoichiometry of one) of the participant species and a^0_j is the activity of species *j* when zero net current passes through the electrode. The difference in the potentials is defined as the overpotential η_0 and is given by [92].

$$\eta_0 = \varepsilon_{electrode} - \varepsilon^0_{elctrode} \qquad (7)$$

The overpotential is positive for anodic reactions and negative for cathodic reactions. Moreover the overpotential is a sum of the following three components [92].

$$\eta_0 = \eta_{ct} + \eta_{conc} + \eta_{xlt} \qquad (8)$$

Where charge transfer η_{ct} is the charge transfer overpotential , η_{conc} is the concentration overpotential , and η_{xlt} is the crystallographic growth. The overpotential for crystallographic growth is the component that we are interested in, however it is difficult

to measure it experimentally. The way around this is to measure the deviation voltage ΔV_{dev}, and this is the primary source of information regarding the electrocrystallization of CdS.

The charge transfer overpotential η_{ct} is the only reaction that is directly affected by the electrode potential, and is the amount of activational energy that must be supplied to produce the desired reaction current by increasing charge transport of carriers through the double layer. These heterogeneous kinetics can be described by the current potential characteristic equation below, for the rate determining step of multistep reactions by using the concentration of the rate limiting species at their electrode interface values $C_{O/R}^{(0,t)}$ [92]:

$$i = zFAk_O^0\left[C_O^{(0,t)}e^{-\alpha_{ct}f(\varepsilon_{electrode}-\varepsilon^0_{electrode}(rds))} - C_R^{(0,t)}e^{(1-\alpha_{ct})f(\varepsilon_{electrode}-\varepsilon^0_{electrode}(rds))}\right] \quad (9)$$

If the rate step is a one step, one electron process, equation can be written as below [92]:

$$i = i_0\left[\frac{C_O^*(0,t)}{C_O^{bulk}}e^{-\alpha_{ct}f\eta_{ct}} - \frac{C_R^*(0,t)}{C_R^{bulk}}e^{(1-\alpha_{ct})f\eta_{ct}}\right] \quad (10)$$

Where i_0 is the exchange current, and is a measure of how easily a reduction-oxidation (redox) couple establishes a net zero current at equilibrium. The transfer coefficient α_{ct} is a measure of the symmetry of the activation barrier for the redox couple. Reaction under an applied potential may become mass transfer limited or activation limited. The overpotential region for mass transfer control is termed the concentration overpotential, which has two components, diffusion controlled overpotential and non electron transfer related reaction overpotential. Diffusion overpotential is defined by the concentration gradient induced at the electrode interface versus the bulk concentration of the electrolyte, and is given by [92]:

$$\eta_{diff} = \varepsilon_{electrode} - \varepsilon^{0}_{electrode} = \frac{RT}{nF}\sum_{j} \ln \frac{a_j^{electrode}(i,t)}{a_j^{bulk}} \tag{11}$$

A reaction overvoltage η_{rxn} occurs for multistep electrode reactions where the rate of reaction is not governed by Butler Volmer kinetics [93]. For the case of specific adsorption in the absence of diffusion limitations, the value of the reaction overvoltage η_{rxn} is the Nernst equation with the ratio of the adsorbed reactant concentration participating in the electron transfer reaction to bulk reactant concentration [94]. The diffusion overpotential η_{diff} and the reaction overpotential η_{rxn} are often difficult to separate, and are considered as the concentration overpotential η_{conc} [92].The crystallization overvoltage η_{xlt} can be defined as the potential that must be added to the system at equilibrium to drive the inclusion of adsorbed atoms, after their participation in the charge transfer reaction, in to the ordered lattice of the growing solid electrode [92]. The crystallization potential overpotential typically includes the lower energy and rapid step-edge growth overpotential $\eta_{xlt}^{step-edge}$ and the higher energy new layer nucleation overpotential η_{xlt}^{nuc}. As it is hard to decouple the charge transfer and crystallization overpotentials, the activation overpotential is going to be estimated by measuring experimentally the deviation voltage ΔV_{dev} [92].

The nucleation overpotential η_{xlt}^{nuc} is the additional energy required to produce a new 2-D layer of growth on the solid electrode once the step edges have grown out of existence. The resulting microstructure of the electrodeposition is a result of the competition between the propagation of the existing 2-D growth step-edges to the limit of the nanowire dimensions and nucleation of new growth steps [92].

5.2.1 Electrode Kinetics:

Baranski has examined the electrode kinetics involved in the reduction of CdS for thin film semiconductor deposition on noble metal substrates [95], and the synthesis equations are given below:

$$S_{8sol} \xrightarrow[chemsorption]{} 8S^{*}_{electrode} \tag{12}$$

$$Cd^{2+}_{sol} + 2e^{-} \longrightarrow Cd_{electrode} \tag{13}$$

$$Cd_{electrode} + S^{*}_{electrode} \longrightarrow CdS \tag{14}$$

The driving force in the self organization of such a multi element compound reaction, is the free energy of formation ΔG^{0}_{f}. The more negative the free energy is, the more selective compound formation will be by minimizing secondary effects. For CdS electrodeposition, the potential for the overall reaction [92].

$$Cd^{2+} + S + 2e^{-} \xrightarrow[electrode]{} CdS \tag{15}$$

Is given by

$$E^{0}_{std}(CdS) = E^{0}_{std}(Cd) - \frac{\Delta G^{0}_{CdS}}{2F} \tag{16}$$

The above equation can be interpreted in the following way. The formation of the compound on the cathode is displaced by 0.73 volts for CdS [92], that corresponds to the second term in the equation, i.e. $-\frac{\Delta G^{0}_{CdS}}{2F}$. In this situation, Cd is preferentially deposited on sulfur in a 2-D mode, called underpotential deposition, which prevents Cd electrodeposition on a Cd electrode surface. The interactions between sulfur are slightly repulsive, which lead to sluggish specific absorption of sulfur on the freshly electrodeposited Cd plane, which in turn may be a prospective source of reaction

overpotential η_{rxn} that is a part of the concentration overpotential η_{conc} .This holds true, if large stoichiometric excess of sulfur is not used in the reaction, or reaction is not conducted at elevated temperatures. This mechanism holds true for a variety of chalcogenide semiconductors (Cd or Zn) based, i.e. CdTe, CdS, CdSe, thereby allowing bandgap engineering by solution composition and applied voltage [92].

5.2.2 Transport Effects during Electrocrystalizatoin

The primary mass transfer effects are diffusion and convection for both participating species, i.e. Cd^{+} and S. The presence of an electric field will also cause electromigration of Cd^{+} within the nanopores. This and other effects such as double layer interactions and electro osmosis are considered secondary effects [92].

The following set of equation describes the flux of ions in a solution in the presence of an applied field. As an approximation, only z component of the flux is considered. The axis is aligned such that the pore axis is parallel to the z axis [92].

$$\vec{J}_j = -D_j \vec{\nabla} C_j - \frac{v_j F}{RT} D_j C_j \vec{\nabla}\phi + C_j \vec{v} \qquad (17)$$

The first term is the diffusion, the second term is the electromigration due to the applied field $\vec{\nabla}\phi$, and the last term is the flux of ion *j* due to bulk fluid flow. The solution of the equation describes the concentration overpotential during the deposition of CdS. Recent works by Heerman,[96] and Mendoza [97] on diffusion controlled electrochemical crystallization, that is typical in the nanowire growth, have described the solutions to be locally smooth, low frequency, decay type functions, that allow for separation of timescales between crystal growth and nucleation phenomenon from mass transfer

effects. The rate of change of the overpotential with respect to the wire length axis, increases first, and then decreases as the electrode proceeds towards the pore mouth. The diffusion distance inside the pore is reduced the concentration gradient increases. As the growing CdS nanowire approaches the pore mouth, the concentration overpotential η_{conc} starts to decrease. This is typically seen in deposition curves for nanowires [92].

The lower frequency decay type behavior is typical of η_{conc}, and the higher frequency crystal behavior is η_{act}.The activation potential η_{act} can be obtained by locally fitting the data, removing the low frequency trend, and then creating a zero sum signal [92]. The residuals defined as deviation voltage, are shown to contain the necessary information that describes the crystal growth. Electro-osmosis effects and electro migration effects can be neglected [92], as most of the information lies in the deviation voltage.

5.2.3 Crystallization Effects of Electrodeposition

The electrodeposition dynamics are governed by two rate determining steps. On the one hand, the electron transfer reaction must produce an adatom on the electrode, with different rates for different crystal faces [92]. On the other hand, surface diffusion to kink/step sites and incorporation into the lattice takes place, which is also dependent of the crystal surface. If a perturbation is applied to the field with a characteristic time shorter than the time required for surface diffusion and lattice incorporation, additional nucleation sites will emerge [98]. These additional sites will possibly produce stacking faults, vacancies, and grain growth with boundaries, that contributes to the nonuniform propagation of the surface. This is the possible reason that AC produces high defects [99] while DC galvanostatic control electrodeposition produces nearly single crystalline

growth [100]. For the later, the goal is to allow the electrocrystallization system to choose its most energetically favorable level of overpotential and allow the system to govern its own microstructure [92].

Mononuclear layer by layer growth, takes place on quasi perfect faces [101], only at overpotentials in the vicinity of or slightly above the critical nucleation overpotential for the system [102]. At higher cathodic voltages, the nucleation rate increases steeply and additional nucleation sites emerge as the 2-D underpotential deposition (UPD) behavior transitions to the more typical 3-D multilayer, multi nuclear overpotential deposition (OPD).

Two important factors dominate electrochemical 2-D nucleation with layer by layer growth [92].

1. The average nucleation period $\bar{\tau}_{nuc} = (J_{nuc}\eta_{xstl}A_{cathode})^{-1}$ with the nucleation rate J_{nuc} as a strong function of η_{xstl} and the surface area of the cathode $A_{cathode}$.
2. The propagation time $\tau_p = A_{cathode}^{1/2} v\eta_{xstl}^{-1}$ required for a monoatomic layer to cover the whole surface area $A_{cathode}$ of the face.

The nucleation rate $J_{nuc}\eta_{xstl}$ is shown by Budevski et al. [102] to be an exponential function of the overpotential η_{xstl}. The step propogation velocity $v\eta_{xstl}$ is a linear function of the overpotential η_{xstl}, according to Staikov et al. [103], of the concentration of the adatoms on the surface and therefore can be approximated as a linear function of the overpotential η_{xstl}. This approximation holds for the low overpotential η_{ct} range when the Butler-Volmer term of equation (4) satisfies the following $\frac{zF|\eta_{ct}|}{RT} < 1$, which is typical of

electrocrystallization in the low Cd limit. If the average nucleation time $\bar{\tau}_{nuc}$ is much larger than the time required to propagate the step edges to the boundary of the system τ_p, each layer will form to completion before subsequent nucleation. This is the reason galvanostatic deposition is employed as the system will operate at the lowest possible $\Delta V_{applied}$ to achieve a set current, which minimizes τ_p amd maximizes $\bar{\tau}_{nuc}$ [92].

This gives the basic foundation for galvanostatic electrochemical growth of II-VI semiconductors, i.e. CdS, within a nanoporous template. The experimental apparatus is described next.

5.3 Apparatus for Electrochemical Growth

The experimental setup for growth comprises of three water tight, completely sealed chambers that are connected to each other via tubes that serve for vapor exit only. The cover has six openings of different sizes for a stirrer, a working electrode/sample, a platinum counter electrode, a platinum reference electrode wire, a condenser, and a thermocouple. The condensers in all three chambers feed into a manifold that is in turn connected to an oil bubbler, where the vapors get mixed into the oil, and thus vapor pressure is released with no possible back path for surrounding air to enter. The condensers have a water inlet and outlet that is connected to the chiller. The chambers are opened only when the sample needs to be immersed into the solution or at completion of the experiment to take the sample out. This ensures that the solution is isolated from any possible sources of contamination in the surrounding atmosphere, as well as keeping the chemicals confined in the chamber, for safety issues. The solvent used in all of the work is DMSO (Dimethyl sulfoxide) that is an excellent solvent for cadmium chloride ($CdCl_2$),

with sulfur (for CdS), tellurium (for CdTe) and selenium (for CdSe), and combinations thereof (for alloy deposition). In addition, DMSO does not react with the alumina template. Once the experiments are completed, and the solution has cooled down, argon gas is passed through the chambers, to draw any vapors that were in the chamber to the oil bubbler where they are mixed, and thus the chamber has an argon blanket on top of the solvent. The setup is shown in Figure 43. The vessels are heated by a built in metal within the glass wall, that is temperature controlled by a power supply that reads the temperature through the thermocouple, and controls it within an accuracy of 0.1° C. For electrodeposition a computer software written in LabView controls a Gamry card that serves as a power supply for potentiostatic or galvanostatic reactions, and also records the data with very high accuracy (in micro volts) and high data rate (in kHz). This level of accuracy is required for electrodeposition where we expect current and voltage variations to be in micro regime.

Figure 43: Experimental Setup for Electrochemical Deposition for II VI Semiconductors Electrochemical deposition is carried out in a solvent based environment

5.4 Quantum Wires, Quantum Dots Electrodeposition in Alumina Templates

Many methods are employed for depositing materials in PAA, including chemical vapor deposition [104], electrodeposition [105], electroless deposition [106], and sol gel deposition [107]. More recently VLS has been utilized for deposition of Si, and Ge nanowires within anodic alumina membranes [108]. Of all approaches for depositing semiconductor nanowires into PAA, electrochemical synthetic approach is the most favorable [8].

Semiconductor quantum dots have been fabricated by various techniques including MBE [109], MOVPE [110], CBE [111]. Devices have also been realized most important being quantum dot lasers and single electron sources. III-V semiconductors have been the focus of most of the quantum dot research, and more of the synthesis involved in II VI semiconductor quantum dot fabrication has been in chemical and thus difficult to integrate in silicon technology [112]. Quantum dots are used as single photon sources for their stability, narrow spectral linewidths, rapid radiative decay rates, and possibility to be integrated into larger structures [113]. For photodetector applications quantum dots are more attractive than nanowires as they inhibit phonons due to increased discretization of density of states, and are less prone to temperature variance [8]. PAA has been used as a host for growing nanowires, in case of quantum dots however its use has primarily been of a mask for quantum dot fabrication. This was demonstrated with techniques like thermal evaporation [114], and MBE [115]. Ni Quantum dots were also fabricated within porous alumina using electrodeposition as a technique, however there results indicate that nanostructures obtained after deposition and barrier removal do not lie at the base [116].

5.4.1 Template Fabrication

Starting with an n-type Si substrate, the following metal layers were sequentially deposited (without breaking vacuum when switching between metals) using electron beam evaporation at a vacuum level of 10^{-6} torr: 30 nm layer of Pt, 5 nm of Ti, and 500 nm of Al, as given in ref [8]. Once these metals are deposited on the desired substrate, the wafer is placed in an electrochemical cell with the wafer and template serving as the anode and a Pt cathode counter electrode. The anodization is carried out in an agitated

0.5M H_2SO_4 solution at 10°C at a constant 25V. As the anodization terminates and the Ti at the base is exposed, the voltage is ramped at a rate of 1.5V/min to ~55V and in the process removing the alumina barrier at the base of the pores. Subsequently, the voltage is ramped several times from the anodization potential to 55V at a rate of 1.5V/min, to clean up the pores. The sample is removed from the anodization chamber after this procedure, and rinsed with distilled water, and dried. A pore widening etch is then performed using a 5% by weight H_3PO_4 solution at room temperature for 30min., and then the sample is rinsed and dried.

5.4.2 Quantum Wire Fabrication Results

Results for the electrodeposition are presented. CdTe was cathodically deposited in anodic aluminum oxide (AAO) template at the constant current density of 0.25-2.5 mA cm^{-2} for 10~20 minutes at 160°C. The electrolyte solution consisted of 1.00 mol L^{-1} $CdCl_2$, 0.01 mol L^{-1} $TeCl_4$ and 0.3 mol L^{-1} KI in glycol [105].

The photoluminescence (PL) results of CdTe films at room temperature indicate transmission peak at 730 nm, which matches closely the peak found in litterature. The slight bulge in the PL peak at around 783 nm is attributed to excitons bound to neutral acceptors.

The shoulder seen at around 795 nm is attributed to the acceptor centers which are isolated cadmium vacancies that are responsible for Te^{4+} surface trap states [117]. A series of thin films were prepared for different deposition currents of 0.25mA, 0.5mA, 1.5mA, and 2.5mA, as shown in Figure 44 below. The deposition time was maintained constant at 5 minutes in each case. We can see that the shoulder at around 650 nm

decreases with decreasing the deposition current.

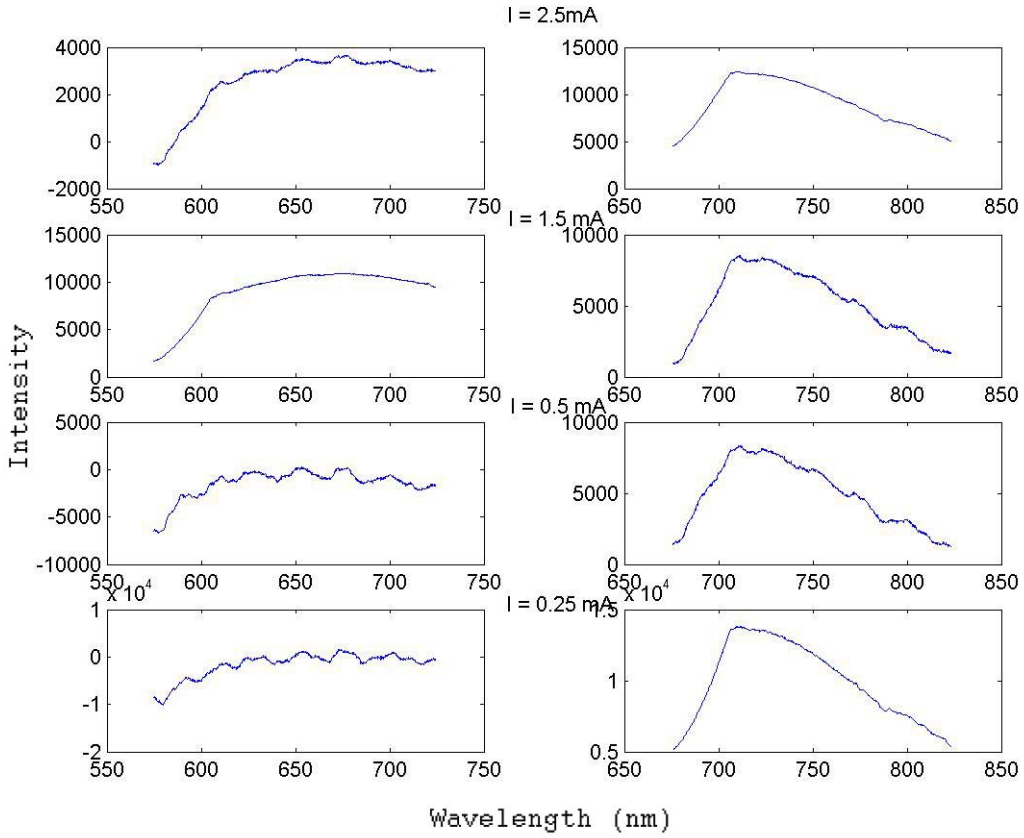

Figure 44: PL results of CdTe for different deposition currents at Room Temperature. A decrease in current usually has the effect of increasing grain size, and reducing defects in the structure being deposited [92].

CdTe nanowires have been deposited in the anodized multiplayer template with Pt exposed at the bases, and then pore widened etched with phosphoric acid. Again the bath used was the same as above. We were able to get nanowires deposited; however there was a concern about the presence of the template matrix around the nanowires. The template seemed to have dissolved, at inspection of SEM. An image of the SEM of the nanowires is given in Figure 45. As seen in Fig. 45, the nanowires are loosely distributed

and short in length, and the template is missing.

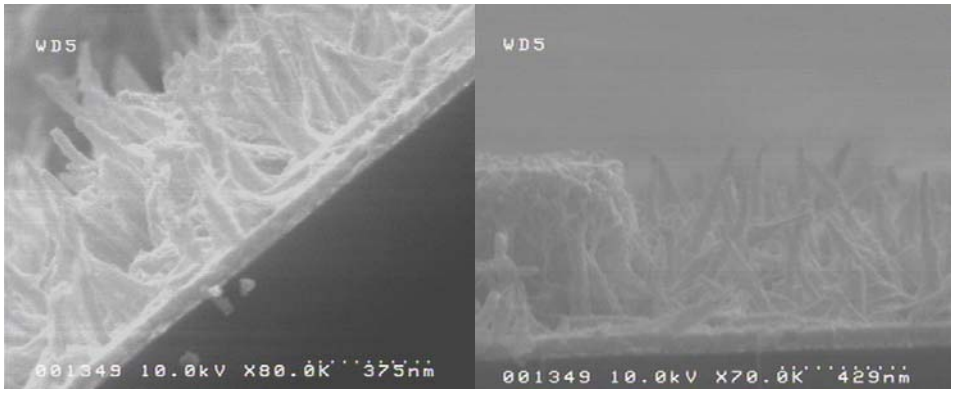

Figure 45: SEM of CdTe Nanowires electrochemically deposited in Ethylene Glycol Solution. The template has bee etched away within a couple of minutes of electrodeposition. The bar is 375 nm in length on the left image, and 429nm in the right image.

There are two possible sources of the dissolution. The first one is that the template is getting dissolved prior to the electrodeposition, which is unlikely for a 30 minute etch, as pore widening etch study on the alumina template only negates that. The second possibility is that the solvent is reacting with the alumina template. It is known that alumina is stable at a pH of 5-8 [118].

An analysis of the solution's pH confirmed the solution to be 3, hence acidic. Therefore the dissolution was occurring in the electrodeposition bath. As the depositions were carried out in Ethylene Glycol solution, and the fact that alcohol groups can participate in Acid/Base chemistry, it was understood that we need to change the solvent. DMSO was attractive because it can solvate a wide range of ionic and non-ionic compounds and is aprotic. Thus, a non-aqueous aprotic solvent is a better match for our AAO system. So the synthesis technique for CdTe nanowire growth was modified.

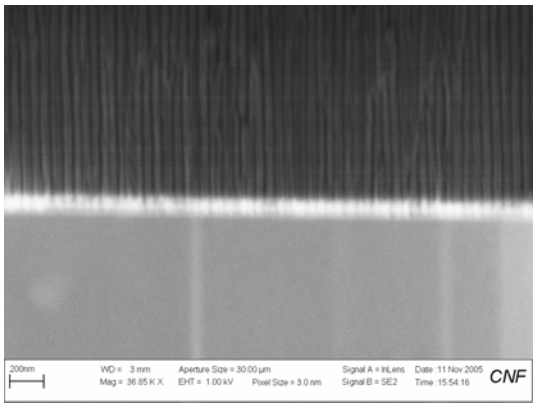

Fig. 46: Cross-sectional SEM view of CdTe nanowires grown using the alumina based nanotemplate. The alumina has pores that are long and straight allowing for the fabrication of high quality nanowires.

The DMSO solution consisted of $CdCl_2$ and Te powder [119]. SEM Images of the nanowires in the template as a cross section are given in Figure 46. A better image to confirm successful CdTe nanowire deposition was achieved by dissolving the template, and an SEM of the nanowires is given in Figure 47.

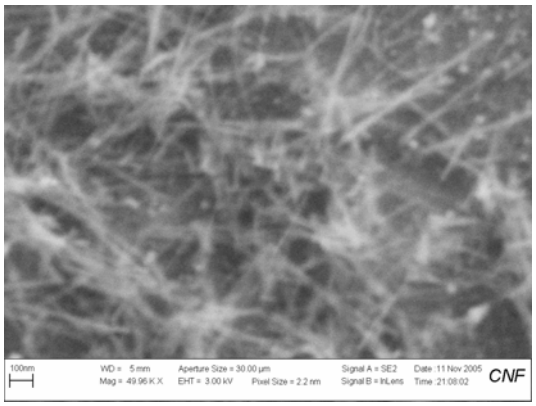

Fig. 47: SEM Top view of CdTe Nanowires, using DMSO as a solvent after template removal. The nanowires have diameters of approximately 10nm.

5.4.3 Quantum Dot Fabrication Results

There is not much difference in the fabrication technique for quantum wires versus quantum dots. The deposition time can be short for the fabrication of QDs, it can be long for the fabrication of QRs, and the growth solution can be changed during the deposition to allow for quantum wire heterostructures or superlattices composed of different II-VI semiconductors to be fabricated. Therefore, after successfully depositing CdTe nanowires within the template, we optimized the alumina template as mentioned in the previous chapter, to get good quality nanostructures, and more consistent electrodeposition results. During this process, it was possible to deposit high density CdTe quantum dots. Electrodeposition of CdTe quantum dots was carried out in a dimethyl sulfoxide bath, with 0.005M $CdCl_2$ and 0.004M Te powder at 140°C, at a current density of approximately 0.3mA/cm2, for 5min following a similar recipe to the one given in [119]. For structural characterization the alumina template was removed completely by immersing it in a 5% by weight H_3PO_4 for an hour at room temperature. An SEM of the quantum dots is shown in Figure 48. Luminescence data, taken at room temperature using a computer controlled Ocean Optics USB 2000 spectrometer. The sample was excited by a LED centered at 365 nm, with a band pass filter of 25 nm. The luminescence spectrum was collected by a collomating lens of quartz, connected to a fiber that was in turn connected to the spectrometer.

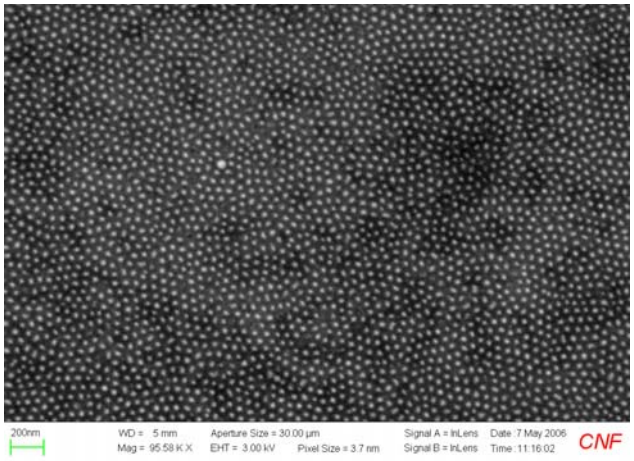

(a)

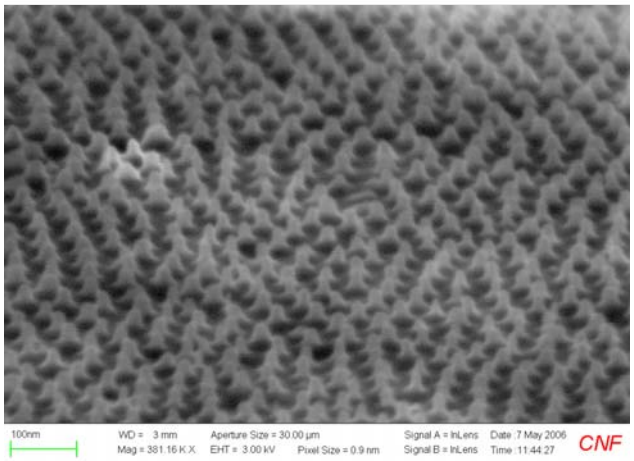

(b)

Figure 48: An SEM image of the top view of the QDs is given in Fig. 7(a). The QDs exhibit a hexagonal close packed distribution, identical to the arrangement of the pores in the alumina. An SEM image of the CdTe dots taken at a 15° angle is shown in Fig. 7(b). A uniform distribution of uniformly sized QDs with regular spacing, and a diameter of 15.5nm and pore spacing of approximately 30nm are observed. Also this array of QDs has a very high packing density, approximately 1.5×10^{10}/cm2.

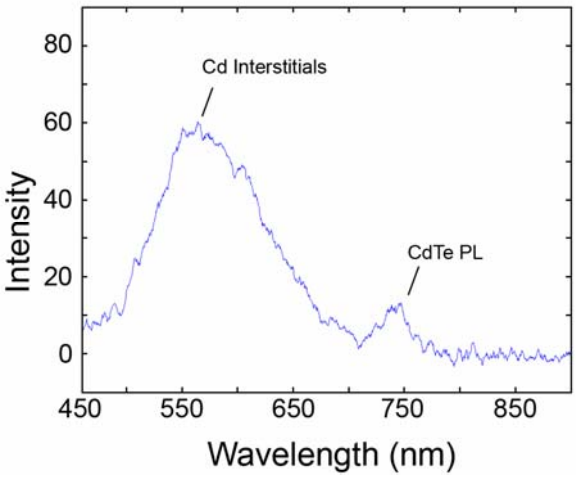

Figure 49: Luminescence Result for CdTe quantum dots at room temperature

Luminescence results of the sample are given in Fig. 49. As seen in Figure.49 there is a broad peak at around 564nm, and a lower intensity peak at around 740 nm. The second peak corresponds to the bandgap of CdTe shifted by confinement effects that is expected in quantum dots or wires. The analytical expression for the shift, for cylindrical quantum dots [120] is given by Eq. (1).

$$E_{\Delta} = E_e + E_h = \left(\frac{\hbar^2}{2m_e^*} + \frac{\hbar^2}{2m_h^*} \right) \left[\left(\frac{\theta_0}{R} \right)^2 + \left(\frac{\pi}{H} \right)^2 \right] \tag{18}$$

Given $m_e^* = 0.096 m_0$ and $m_h^* = 0.4 m_0$, and $\theta_0 = 2.404$ as the first zero of the 0th order Bessel function. For a quantum dot radius of 7.75 nm, and height of 20nm, the ground state energy level calculated using Eq. (18) is 0.0596 eV. However, the excitonic Rydberg energy also contributes to a blue shift and the new energy term is given Equation (19) [121].

$$E_{new} = E_g + E_{\Delta} + 0.752\Re \tag{19}$$

The value of $\Re = 10meV$. Here, we haven't taken into account the Coulombic interaction, which is much smaller compared to E_Δ and $\Re$. The above values added move shift the bandgap from 1.606eV [121] (772 nm) to 1.6731eV (741 nm), as seen in Figure 49 as the smaller peak. Therefore it is seen that the optical bandgap, or direct electron-hole recombination contributes to a lesser extent to the emission spectrum, compared to the emission by the defects, centered at 564 nm. This peak also called the yellow band emission [122] has been attributed to Cd vacancies [123], and has also been seen in CdS thin films.

We believe these results, including the uniformity of the size and distribution of the QDs and the high packing density, using a practical self-ordering mechanism for fabrication (i.e., PAA and the multilayer template), are the best yet reported in the literature on the subject.

Summary

This chapter has described electrochemical deposition in brief, with reaction dynamics. Results within the optimized template have been also mentioned, with characterization results. It can be seen that the optimized template is an excellent starting material for fabrication of quantum wires, quantum dots, and hybrid structures. The next chapter gives future directions in connection with the newly optimized template.

Chapter 6: Conclusion and Future Direction

We have optimized a multilayer template that has great utility for nanowire, nanodots, and other combined nanostructure fabrication, by using electrodeposition, in general. Other techniques can also be employed, such as VLS, MBE, etc. Our results indicate extremely uniform barrier layer removal and titanium oxide layer breakthrough, and good structural integrity of the template after the procedure. A good starting template is indispensable for a good device operation based on this material. Future work within this area would be on two fronts, the theoretical front and the experimental front. These are mentioned in the following two sections:

6.1 Theoretical Front:

On the theoretical front our calculations for the energy levels and absorption are based on the parabolic approximation in context of the envelope function approximation. A brief overview of the parabolic approximation is presented next.

In crystalline materials the main source of current are the electrons and holes. The major

carrier dynamics emerges from the diffraction of electrons and holes off the periodic potential. This diffraction produces the band structure that is a combination of relations between energy and momentum. We assume that the crystal potential is a constant. Then it is possible to apply the Schrödinger's equation in vacuum. As the crystal structure is not vacuum, all effects of the crystal potential on the electron are included in its mass known as the effective mass m^*. The time independent Schrödinger's equation becomes.

$$-\frac{\hbar^2}{2m^*}\nabla^2\psi = E\psi \tag{1}$$

The energy solutions for the above equation are of the form

$$E = \frac{\hbar^2 k^2}{2m^*} \tag{2}$$

This assumption is also known as the effective mass approximation. At low energy near the band edges, there is a quadratic relationship between energy and the wave vector k, and the energy vs. k has a parabolic form, as can be seen in Fig. 50.

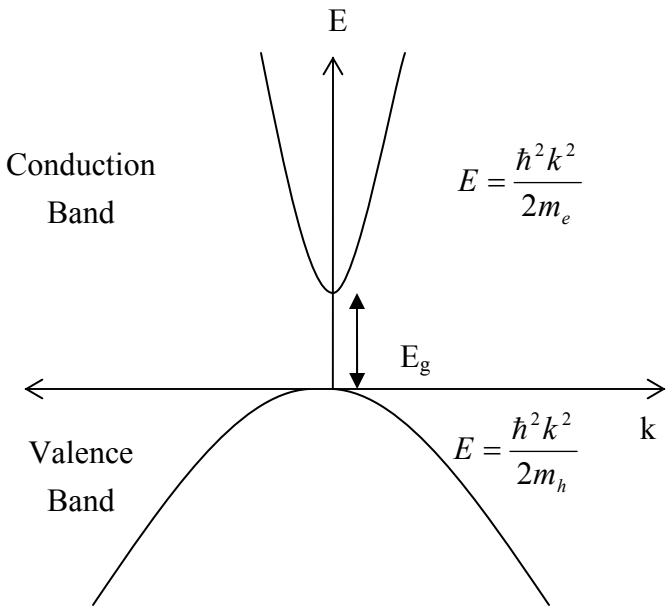

Figure 50: A schematic of the parabolic approximation near the band edges

Electron and hole energy states as a function of wave vector k in the parabolic approximation. The electron and hole effective masses for the conduction and valence bands are given by m_e and m_h. As the effective mass of the electron is much smaller than that of the hole, corrections including second order perturbation theory and beyond make more sense for conduction band than for the valence bands. The conduction band dispersion can be written more accurately as [124].

$$E_c(k) = E_c + \frac{\hbar^2 k^2}{2m_e} + \alpha k^4 + \beta\left(k_x{}^2 k_y{}^2 + k_z{}^2 k_x{}^2 + k_y{}^2 k_z{}^2\right) \qquad (3)$$

Within close proximity to the band edge, it is customary to use the parabolic approximation, especially for wide band gap materials, e.g. InSb.

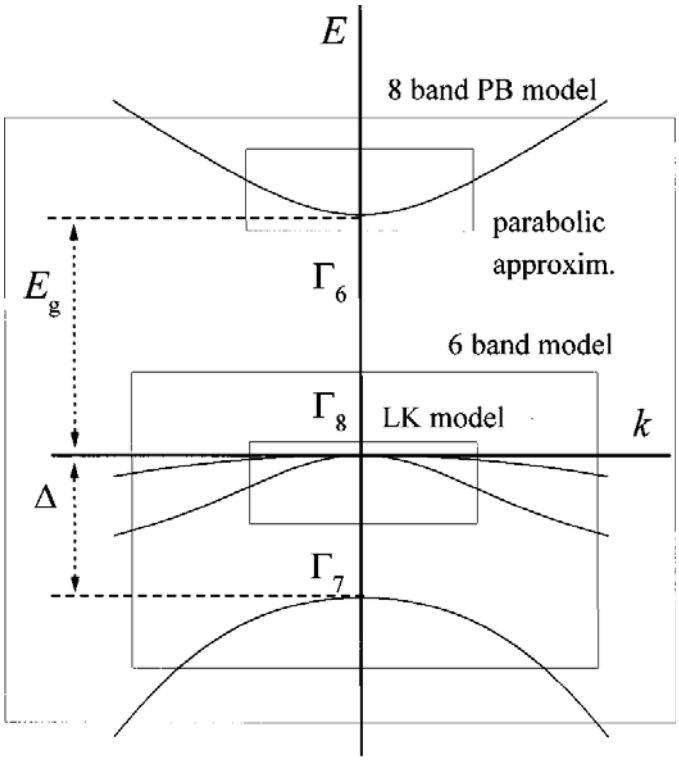

Figure 51: Image showing different techniques for theoretical analysis of band structure that have been studied, and scope of each approach [125]

The bulk band structure of a typical direct gap semiconductor with cubic or zinc blende lattice structure and band edge at the Γ point of the Brillouin zone is given Figure.51 [125]. Figure 51 shows the parabolic approximation as well as other approaches and depicts what other bands are included for the relevant techniques. The band structure shown in figure is typical for semiconductors such as GaAs, InAs, CdSe, CdTe, CdS or InSb. As seen only the band edges of the conduction band and valence bands are parabolic. The valence band shows fourfold degeneracy at Γ_8. These account for the light holes and heavy holes. The point Γ_7 is the spin orbit split off band. For device design we required better understanding of the material properties, in order to be able to predict

optical behavior we need to include the effects of nonparabolicity. The optical properties of materials in the quantum confinement regime arise from transitions between the energy sublevels of electrons and holes. Therefore a more accurate derivation follows from energy calculations based on the real band structure of the semiconductors.

Effective mass approximation has been extensively used to describe electronic motion near band edges. This approach gives very good results with the condition of weak perturbations, i.e. applied magnetic and electric fields, in particular to the shallow impurity problem [126]. The validity of slowly varying perturbation is violated in the structure of a quantum well [127], because the difference between the potentials in the well and the barrier layer is not small nor slowly varying [127].

For lower bandgap semiconductors as well as lower dimensions, such as quantum wires and quantum dots there needs to be a better approximation that is based on all parameters affecting the particle, such as band coupling, spin orbit coupling, etc. for more accurate results required for good device design. An eight band calculation will thus be required for accurate modeling of materials and devices. Such a study was carried out by PB [128]. PB studied the magnetic energy levels in the valence and conduction bands at the zone center, by a modified version of the L.K. effective mass method [126]. They have included coupling between conduction and valence bands exactly, and effects of higher order bands to order k^2. This includes the effects of non parabolic conduction and light hole bands, as well as warping of the conduction and valence bands, and the quantum effects of the light and heavy hole valence bands.

Therefore later simulations need to address the calculation based on the $\vec{k} \bullet \vec{p}$ theory, in context of envelope function approximation with second order effects included. As a

starting point in case spin orbit interaction and external fields are ignored, that will be included later as perturbations, the lattice periodic functions obey the following relation.

$$\left[-\frac{\hbar^2}{2m_0}\Delta+\frac{\hbar}{2m_0}k\cdot\frac{\hbar}{i}\nabla+\frac{\hbar^2k^2}{2m_0}+W(r)\right]u_{jk}(r)=E_j(k)u_{jk}(r) \tag{4}$$

The term in the bracket is the Hamiltonian. Applying perturbation theory, the following decomposition can be used.

$$\hat{H}(k)=\hat{H}^{(0)}+\hat{H}^{(i)}(k)+\frac{\hbar^2k^2}{2m_0} \tag{5}$$

$$\hat{H}^{(0)}=-\frac{\hbar^2}{2m_0}\Delta+W(r);\hat{H}^{(i)}(k)=\frac{\hbar}{2m_0}k\cdot\frac{\hbar}{i}\nabla \tag{6}$$

The term $\frac{\hbar^2k^2}{2m_0}$ is a scalar and does not affect the eigenfunctions. The eigenvalues and eigenfunctions in the vicinity of k=0 can be calculated by the unperturbed eigenvalues and eigenfunction, $E_j=E_j(k=0)$ and $u_j=u_{j,k=0}$.The matrix elements of the perturbation are evaluated from the following expression.

$$\left(j\left|\hat{H}^{(i)}(k)\right|j'\right)=\frac{\hbar}{m_0}k\cdot p_{jj'};p_{jj'}=\frac{1}{\Omega_0}\int_{\Omega_0}d^3ru_j(r)\frac{\hbar}{i}\nabla u_{j'}(r) \tag{7}$$

Which is why it is called the "$k\cdot p$" theory. [129]

Hence, on the theoretical front, better more accurate calculations involving a full eight band approach needs to be taken. In addition, phonons need to be studied in greater detail, to study operation with respect to temperature variance.

The present theoretical is based on the effective mass approximation in context of the envelope function approximation, which is described without going into atomic details. This approach has turned out to be quiet successful, as it is a good compromise between

simplicity and reliable results. For more accurate analysis, other techniques may need to be explored. This is because as materials are scaled further down, EFA approximation may not be accurate anymore. In such a scenario, the theory has to be replaced by an ab initio approach, that would be much more complex itself as well as the computational cost it would require. The ideal situation would be to have a complete quantum description based on a full band approach, while avoiding the computational load of ab initio techniques, and limitations of EFA.

Localized basis approaches such as the tight binding (TB) approach have been extensively used to predict electronic properties of nanostructure [130]. TB methods can also be coupled with Transfer Techniques or Green Function Techniques to study transport properties in nanostructure systems. The TB approach being a full band approach overcomes the shortcomings of the envelope function approximation and includes atomic details, for a realistic formulation of the band structure in the complete Brillouin zone. Future work on the experimental and fabrication front is briefly stated next.

6.2 Experimental and Fabrication Front:

At this point, we have optimized the multilayer template. We have shown electrodeposition of CdTe nanowires, nanodots, and CdS nanowires. Future work will include structural and optical characterization of the fabricated materials, including II-VI semiconductor quantum wires, quantum dots, superlattices, and other combined structures of one material or ternary alloys of the II-VI semiconductors, such as CdSSe, CdZnSe. The possibility of electrodepositioin of III-V materials can also be explored with in the template [131].

Photodetection applications are a small subset of the types of application that template based nanostructures can have, e.g. lasers, diodes, chemical biological sensors, etc. and these can be explored. With the added advantage of having the substrate of choice, i.e. silicon, this process can allow for many types of device structures to be fabricated and easily integrated with other circuitry. One possible application in case of photodetectors would be focal plane arrays, with readout circuitry on the same substrate. A schematic of the readout circuitry is shown in Figure 3.

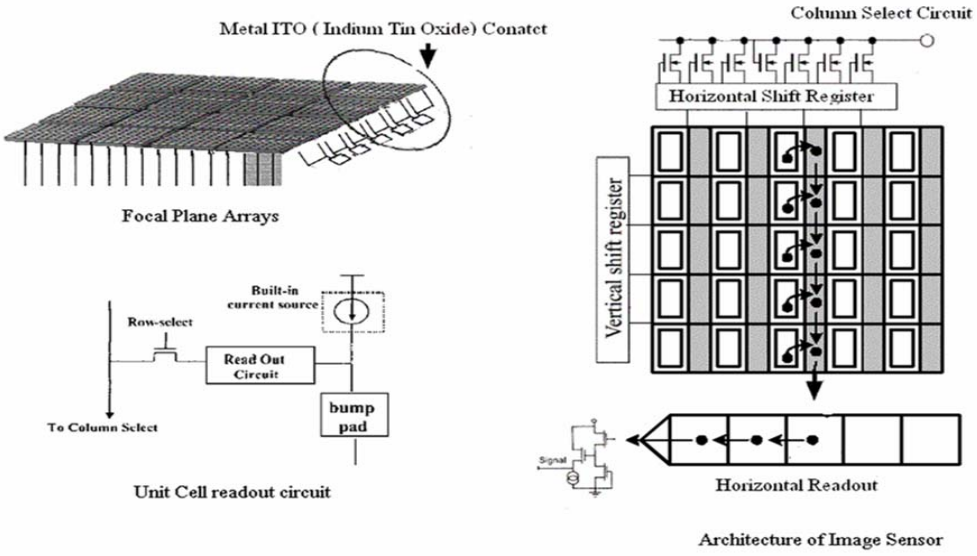

Figure 52: Readout Circuitry for Focal Plane Array that can be fabricated on the same substrate, due to ease with si integration.

For this to be realized a study of issues related to incorporation of this material into a device structure, for which packaging steps such as interconnects, and device layout need to be understood and implemented. A very promising device application for these

structures would be a focal plane array.

The template has been fabricated on silicon to be able to integrate it with existing technologies. Another device application may be a multiwavelength detector, as shown in Figure 4. The structure has multiple stacks of nanowires, on a float glass substrate. The absorption of each layer has a window width that decreases from top to bottom. For this different semiconductor materials can be used, each tuned to absorb a certain range of the spectrum, as shown in Figure 53.

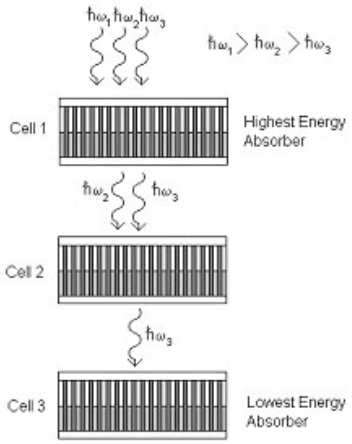

Figure 53: Schematic device structure of cascaded II-VI heterostructure quantum wire multiwavelength detector.

This is just a few directions in which research can be conducted based on the multilayer template and nanostructures based on the same. At this point we are exploring the fabrication of alloys, and nanowire heterostructures of II-VI semiconductors within this material structure.

References:

[1] A. C. Sharma, J. Appl. Phys. 100 (2006) 084301.

[2] E. Towe, D. Pan, 6, IEEE Journal of Selected Topics in Quant. Electr. 6 (2000) 408.

[3] Y.-C. Chang, R. B. James, Phys. Rev. B vol.39, number 17, 1989.

[4] M. A. Reed, J. N. Randall, J. H. Luscombe, Nanotechnology 1 (1990) 63-66.

[5] R. Q. Yang, J. M. Xu, M. Sweeny, Phys. Rev. B 50 (1994) 7474.

[6] J. Phillips, J. Appl. Phys. 91 (2002) 4590.

[7] S. J. Chua, S. J. Xu, X. H. Zhang, x. C. Wang, T. Mei, W. J. Fan, C. H. Wang, J. Jiang, X. G. Xie, Appl. Phys. Lett. 73 (1998) 1997.

[8] D. Crouse, M. Crouse, Infrared Phys. & Tech. 48, 227 (2006).

[9] X. Zhang, Y. hao, G. Meng, L. Zhang, J. Electrochem. Soc. 152 (2005) C 664-C668.

[10] J. Luo, L. Zhang, Y. Zhang, J. Zhu, Adv. Mater. 14 (2002) 1413.

[11] C. Yoon, J. S. Suh, Bull. Korean Chem. Soc. 23 (2002) 1519.

[12] D. J. Peňa, J. K. N. Mbindyo, A. J. Carado, T. E. Mallouk, C. D. Keating, B. Razavi, T. S. Mayer, J. Phys. Chem. B 106 (2002) 7458.

[13] J. S. Tresback, A. L. Vasiliev, J. Mater. Res. 20 (2005) 2613

[14] B. R. Martin, D. I. Dermody, B. D. Reiss, M. Fang, L. A. Lyon, M. J. Natan, T. E. Mallouk, Adv. Mater. 11 (1999) 1021.

[15] Z. H. Yuan, H. Huang, S. S. Fan, Adv. Mater. 14 (2002) 303.

[16] Z L Xiao, Y H Catherine, U Welp, H H Wang, K W Kwork, G A Willing, J M Hiller, R E Cook, D J Miller, CrabtreeW G Crabtree, Nano. Lett. 20 (2002) 1293.

[17] Y T Tian, G W Meng, T Gao, S H Sun, T Xie, X S Peng, C H Ye and L D Zhang, Nanotechnology 15 (2004) 189.

[18] X. Peng, A. Chen, Nanotech. 15 (2004) 743.

[19] O. Takeshi , H. Xavier, F. Andrea, G. Laurent, A. Philippe, J. Mater. Chem. 13 (2003) 2530.

[20] H. Andrzej, L. Hubert, S. Maciej, Y. Q. Zhu, K. H. Wen, W. K. Harold, R. M. W. David, J. Phys. Chem. 106 (2002) 1534.

[21] Y. C. Wang, I. C. Leu , M. H. Hon, J. Mater. Chem. 12 (2002) 2439.

[22] D. Crouse, A.A.Ikram, A. Miller, M. Crouse, Proc. of SPIE 5592 (2005) 296.

[23] M. M. Crouse, A. E. Miller, D. T. Crouse, and A. A. Ikram, J. Electrochem. Soc. 152 (2005) D167.

[24] S. K. Das, G. C. Morris, J. Appl. Phys. 73 (1993) 782.

[25] C.S. Ferekides, D. Marinskiy, V. Viswanathan, B. Tetali, V. Palekis, P. Selvaraj, D.L. Morel, Thin Solid Films 361 (2000) 520.

[26] V. Mitin, V. Kochelap, M. A. Stroscio, *Quantum Heterostructures,* Cambridge Universtiy Press, 1999

[27] B. Äoer, K.W., *Survey of Semiconductor Physics, Vol. 1: Electrons and Other Particles in Bulk Semiconductors,* Van Nostrand, New York, 1990.

[28] Cheng et al., Journal of Materials Chemistry 15 (2005), 3409-3414

[29] R. Henriquez, J. Gomez, G. Riveros, J. F. Guillemoles, M. Froment, D. Lincot, J. Phys. Chem. B 108 (2004) 13191-13199.

[30] K. Premaratne, S. N. Akuranthilaka, I. M. Dharamadasa, A. P. Samantilleka, Renew. Energy 29 (2003) 549-557.

[31] M. Wolfe, N. Holonyak, G. E. Stillman, Physical Properties of Semiconductors, Prentice Hall, New York, 1989.

[32] W. Palmer, Properties of the II-VI semiconductors, 2002, Available from <=http://www.semiconductors.co.uk>.

[33] M. F. Fels, A. U. Hazi, Phys. Rev A 4 (2) (1971) 662-674.

[34] M. F. Fels, A. U. Hazi, Phys. Rev. A 5 (3) (1972) 1236-1249.

[35] David M. –T Kuo, Angbo Fang, Y. C. Chang, Infrared Phys. Technol. 42 (2001) 433-442.

[36] V. A. Mandelshtam, T. R. Ravuri, H. S. Taylor, Phys. Rev. Lett. 70 (13) (1993) 1932-1935.

[37] J. Austin, M. Jaros, Phys. Rev. B 31 (8) (1985) 5569-5572.

[38] S. L. Chuang, Physics of Optoelectronics Devices, John Wiley and Sons, New York, 1995.

[39] Y. Liang, L. Zhai, X. Zhao, D. Xu, J. Phys. Chem. B 109 (2005) 7120.

[40] T. Yamada et al. vol. 40, #9, Phys. Rev. B, 6265 (1989).

[41] B. S. Williams, S. Kumar, Q. Qin, and Q. Hu, J. L. Reno, Appl. Phys. Lett., 88, 261101 (2006).

[42] C. Wirner, Y. Awano, N. Yokoyama, M. Ohno, N. Miura, T. Nakagawa, and H. Bando, Semiconductor Sci. Technol. 24 (1997) 998-1002.

[43] I. E. Kozin, I. V. Ignatiev, S. V. Nair, H.-W. Ren, S. Sugoua and Y. Masumoto, J. Lumin., 87-89, (2000) 441-443.

[44] J. S. Yu, R. Darvish, A. Evans, J. Nguyen, S. Slivken, and M. Razeghi, Appl. Phys. Lett. 88, 041111 (2006)

[45] U. Bockelman, G. Bastard, Phys. Rev. B 42 (1990) 8947.

[46] R. Loudon, *The Quantum Theory of Light*, Oxford University Press, Oxford, Second Edition, 1983.

[47] P. Harrison, *Quantum Wells, Wires and Dots,* John Wiley & Sons, Second Edition, 2005 p. 271

[48] M. J. Kelly, *Low Dimensional Semiconductors: Materials, Physics, Technology, Devices,*Clarendon Press, Oxford, 1995.

[49] A C Sharma et al 1983 J. Phys. C: Solid State Phys. 16 L1233-L1242.

[50] S. H. Rhim, Miyoung Kim, A. J. Freeman, R. Asahi, Phys. Rev. B 71, 045202 (2005).

[51] F. Kootstra, P.L. de Boeij, J.G. Snijders , Phys. Rev. B 62, # 11, (2000).

[52] C. Delerue et al, Phys. Rev. B 68, 115411, (2003).

[53] X. Cartoixa, L. W. Wang, Phys. Rev. Lett. 94, 236804 (2005).

[54] R. Fuchs and K. L. Kliewer, Phys. Rev. 140, A2076 (1965)

[55] N. W. Ashcroft and N. David Mermin, *Solid State Physics* (Saunders College Publishing, Fort Worth, 1976), p. 541.

[56] F. W. de Wette and G. E. Schacher, Phys. Rev. 137, A78 (1965).

[57] L. Wendler, Phys Status Solidi B 129, 513 (1985).

[58] C. Trallero-Giner, F. Comas, and F. Garcia-Moliner, Phys. Rev. B 50, 1755 (1994)

[59] K. W. Kim, M. A. Stroscio, A. Bhatt, R. Mickevicius, and V. V. Mitin, J. Appl. Phys. 70, 319 (1991)

[60] M. A. Stroscio, Phys. Rev. B 40, 6428 (1989)

[61] N. C. Constantinou and B. K. Ridley, Phys. Rev. B 41, 10622 (1990).

[62] F. Keller, M. S. Hunter, D. L. Robinson, J. Electrochem. Soc. 9 (1953) 411.

[63] H. Masuda, K. Fukuda, Sicence 268 (1995) 1466.

[64] A. J. Yim, J. Li, W. Jian, A. J. Bennett, J. M. Xu, Appl. Phys. Lett. 79 (2001) 1039.

[65] G. J. Strijkers, J. H. J. Dalderop, M. A. A. Broeksteeg, H. J. M. Swagten, W. J. M. de Jonge, 86 (1999) 5141.

[66] H. Masuda, H. Yamada, M. satoh, H. Asoh, M. Nakao, T. Tamamura, Appl. Phys. Lett. 71 (1997) 2770.

[67] H. Masuda, K. Yada, A. Osaka, Jpn. J. Appl. Phys. 37, L1340 (1998).

[68] O' Sullivan, J. P., G. C. Wood, Proc. Of the Royal Soc. Of London A., 317 (1970) p. 511-543.

[69] G. Bailey, G. C. Wood, Trans. Inst. Metal. Finish. 52 (1974) 187.

[70] G. E. Thomspson, G. C. Wood, Nature 290, (1981) 230.

[71] V.P. Parkhutik, V. I. Shershulsky, J. Phys. D: Appl. Phys. 25 (1992) 1258.

[72] O. Jessensky, F. Muller, U. Gosele, Appl. Phys. Lett. 72 (1998) 1173.

[73] A.P. Li, F. Muller, A. Birner, K. Nielsh, U. Gosele, J. Vac. Technol. A 17 (1999) 1428.

[74] B.Das, J. Electrochem. Soc., Volume 151, Issue 6, pp. D46-D50 (2004).

[75] A. P. Li, F. Muller, A.Birner, K. Nielsch, U. Gosele, J. Appl. Phys. 84 (1998) 6023.

[76] K. Nielsch, J. Choi, K. Shwirn, R. B. Wehrspohn, U. Gosele. Nano Lett. 2 (2002) 677.

[77] D. Xu, D. Chen, Y. Xu, X. Shi, G. Guo, L. Gui, Y. Tang, Pure Appl. Chem. 72 (2000) 127-135.

[78] S.Shingubara, Y. Murakami, K. Morimoto, T. Takahagi, Surface Science 532–535 (2003) 317–323.

[79] A. B. Greytak, L. J. Lauhon, M. S. Gudiksen, C. M. Lieber, Appl. Phys. Lett. 84 (2004) 4176.

[80] S. Banerjee, A. Dan, D. Chakravorty, J. Mater. Sci 37 (2002) 4261.

[81] N. K. Kontos, R. Moshohoritou, V. Ninni, I. T. Kaplanoglu, Thin Solid Films, 326 (1998) 166.

[82] Y. Yang, H. Chen, Y. Mei, J. Chen, X. Wu, X. Bao, Solid State Comm. 123 (2002) 279.

[83] O. Rabin, P. R. Herz, Y. M. Lin, A. I. Akinwande, S. B. Cronin, M. S. Dresselhaus, Adv. Funct. Mater. 13 (2003) 631.

[84] P. P. Mardilovich, A. N. Govyadinov, N. I. Mazurenko, R. Paterson, J.Membr. Sci. 98 (1995) 143.

[85] N. Yasui, A. Imada, T. Den, Appl. Phys. Lett. 83 (2003) 3347

[86] J. M. Albella, I. Montero, J. M. Martinez-Duart, V. Parkhutik, Journal of Materials Science, 26 (1991) 3422-3432.

[87] Y.S. Hwang, J.W. Lee, S. Y. Lee, B. J. Koo, D. Jin Jung, Y. S. Chun, M. H. Lee, D. W. Shin, S. H. Shin, S. E. Lee, Jpn. J. Appl . Phys. 37 (1998) 1332-1335.

[88] K. Sreenivas, I. Reaney, T. Maeder, N. Setter, C. Jagdish, R. G. Elliman J. Appl. Phys. 75 (1994) 232.

[89] Murray, J.L., *The Pt-Ti binary phase diagram-ASM Handbook.* Binary Alloy Phase Diagrams, 1982. **2**: p. 1915-1916.

[90] S. Y. Kweon, S. Kyung, Choi, S. J. Yeom, J. S. Roh, Jpn. J. Appl. Phys. 40 (2001) 5850-5855.

[91] Christopher M. A. Brett, Ana Maria Olieveira Brett, *Electrochemistry, Principles, Methods, and Applications,* Oxford University Press, New York, 1993.

[92] Michael Crouse, "Enabling One-Dimensional Nanostructured Materials through Electrochmistry with novel template development: An application towards monocrystalline nanowires of cadmium sulfide" University of Notre Dame, (2003)

[93] Bard, A. J. and L. R. Faulkner, *Electrochemical Methods: Fundamentals and Applications.* Second ed. 2001, New York: John Wiley & Sons, 833.

[94] Yoon, H.A. *Coverage Dependent Structures of the sulfur on Pt(111) studied by low energy electron diffraction (LEED) and scanning tunneling microscopy (STM).* Surface Science, 1997, 376 (1997), p.254-266.

[95] Baranski, A.S., W.R. Fawcett, and A.C. McDonald, *The mechanism of electrodeposition of cadmium sulfide on intert metals from DMSO solution.* Journal of Electroanalytical Chemistry, 160 (1984) p. 271-287.

[96] Heerman, L. and A. Tarallo, *Theory of the chronoamperometric transient for electrochemical nucleation with diffusion-controlled growth.* Journal of Electroanalytical Chemistry, 470 (1999) p.70-76.

[97] Mendoza-Huizar, L. H., J. Robles, and M. Polmarr-Pardave, *Nucleation and growth of cobalt onto different substrates Part II: The UPD-OPD transition onto a gold electrode.* Journal of Electroanalytical Chemistry, 545 (2003) p.39-45.

[98] Budevski, E.G. Staikov, and W.J. Lorenz, *Electrocrystallization: Nucleation and Growth Phenomenon,* Electrochemica Acta, 2000 45 (2000) p.2559-2574.

[99] Hutchison, J. L. et al, *TEM and HRTEM structural studies of non-lithographically produced CdS nanowires.* Microscopy of Semiconducting Materials Conference Proceedings 157 (1997) p.389-392

[100] Liu, B. et al. *Photoluminescence and structural characteristics of CdS nanoclusters synthesized by hydrothermal microemulsion.* Journal of Applied Physics, 89(2) (2001, p. 1059-1063

[101] Budevski, E. G. Staikov, and W. J. Lorenz, *Electrocrystallization: Nucleation and Growth Phenomenon.* Electrochimica Acta, 45 (2000) p.2559-2574.

[102] Budevski, E. G. Staikov, and W. J. Lorenz, *Electrochemical Phase Formation and Growth.* First ed. Advances in Electrochemical Science and Engineering, ed. R.C. Alkire, 1996, Weinheim, Germany: VCH.

[103] Staikov, G. and W. J. Lorenz, *The role of crystal imperfections in electrochemical phase formations and growth.* Canadian Journal of Chemistry, 75 (1997) p. 1624-1634.

[104] T. Kyotani, L. Tasi, A. Tomita, Chem. Mater. 8 (1996) 2109.

[105] D. Xu, D. Chen, Y. Xu, X. Shi, G. Guo, L. Gui, Y. Tang, Pure Appl. Chem. 72 (2000) p. 127-135.

[106] V. P. Menon, C. R. Martin, Anal. Chem. 67 (1995) 1920.

[107] B. B. Lakshmi, P. K. Dorhout, C. R. Martin, Chem. Mater. 9 (1997) 857.

[108] J. M. Redwing, S. M. Dilts, K. K. Lew, A. Cranmer, S. E. Mohney, Proc. Of SPIE, 6003 (2005) 60030S.

[109] B. C. Lee, S. D. Lin, C. P. Lee, H. M. Lee, J. C. Wu, K. W. Sun, Appl. Phys. Lett. 80 (2002) 326.

[110] Bhavtosh Bansal, M. R. Gokhale, A. Bhattacharya, B. M. Arora, Appl. Phys. Lett. 87 (2005) 203104.

[111] N. Panev, A. I. Persson, N. Skold, L. Samuelson, 83 (2003) 2238.

[112] V. N. Antonov, P. Swaminathan, J. A. N. T. Soares, J. S. Palmer, J. H. Weaver, Appl. Phys. Lett. 88 (2006) 121906.

[113] C. Santori, D. Fattal, J. Vuckovic, G. S. Solomon, Y. Yamamoto, Lett. To Nature 419 (2002) 594.

[114] J. H. Sung, H. Moon, J. H. Bahng, J. Y. Koo, B. Kim, Mat. Res. Soc. Symp. Proc. 818 (2004) M11.34.1.

[115] D. A.Tenne, O. R. Bajutova, A. K. Bakarov, A. K. Kalagin, A. G. Milekhin, A. I. Toropov, D. R. T. Zahn, Tehchnic. Phys. Lett. 28 (2002) 44.

[116] M. T. Wu, I. C. Leu, J. H. Yen, M. H. Hon, Electrochem. Solid-State Lett. 7 (2004) C61-C63.

[117] J. Hu, Y. Bando, Z. Liu, T. Sekiguchi, D. Golberg, J. Zhan, J. Am. Chem. Soc. 125 (2003) 11306.

[118] C. Li, W. Fan, B. Lei, D. Zhang, J. Han, M. Meyyapan, C. Zhou, Mater. Rese. Soc. Symp. Proc., 818 (2004) 371.

[119] A.C. Rastogi, and K. S. Balakrishnan, J. Electrochem. Soc. **136**, (1989)1502-1505.

[120] S. Le. Goff, Stebem Phys. Rev. B 47 (1993) 1383.

[121] Y. Masumoto, K. Sonobe, Phys. Rev. B 56 (1997) 9734.

[122] R. L. Morales, O. Z. Angel, G. T. Delgado, Appl. Phys. Lett. 73 (2001) 61.

[123] E. S. Brigham, C. S. Weisbecker, W. E. Rudzinski, T. E. Mallouk, Chem. Mater. 8 (1996) 2121.

[124] E. O. Kane, J. Phys. Chem. Solids, 1, 249 (1957)

[125] A.L. Efros, M. Rosen, Phys. Rev. B, 58 (1998) 7120.

[126] J. M. Luttinger, W. Kohn, Phys. Rev. 97 (1955) 869.

[127] M. G. Burt, J. Phys.: Condens. Matter 4 (1992) 6651-6690.

[128] C. R. Pidgeon, R. N. Brown, Phys. Rev. 146 (1966) 575.

[129] S. Glutsch, *Excitons in Low Dimensional Semiconductors: Theory, numerical Methods, Applications,* Springer Verlag Berlin Heidelberg New York, (2004).

[130] A. Di Carlo, Semiconductor Science and Technology 18, (2003) R1-R31.

[131] X. Zhang, Y. Huo, G. Meng, L. Zhang, *J. Electrochem. Soc.* 152 (2005) C664-C668.